

Phase-space resolved decay rates of driven systems near the transition state

Von der Fakultät Mathematik und Physik der Universität Stuttgart
zur Erlangung der Würde eines Doktors der Naturwissenschaften
(Dr. rer. nat.) genehmigte Abhandlung

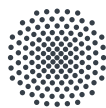
Vorgelegt von

Matthias Feldmaier

aus Nürtingen

Hauptberichter: Prof. Dr. Jörg Main
Mitberichter: Prof. Dr. Udo Seifert

Tag der mündlichen Prüfung: 07. September 2020



Universität Stuttgart

1. Institut für Theoretische Physik

2020



Inhaltsangabe

Die Bewegung einzelner Atome oder Moleküle bei chemischen Reaktionen lässt sich in vielen Fällen durch klassische Mechanik auf einer Born-Oppenheimer Potentialfläche beschreiben. Hierbei sind die Reaktanten oft durch eine Rang-1 Barriere von den Produkten getrennt. Eine solche Barriere ist durch einen instabilen Freiheitsgrad, die Reaktionskoordinate und eine gegebene Anzahl an stabilen Freiheitsgraden, die orthogonalen Moden, charakterisiert. Eine reagierende Trajektorie wird die Barriere meist in der Sattelregion, d. h. in einer direkten Umgebung des Sattels, überqueren. Diese Region fungiert als Flaschenhals für die Reaktion. Im Rahmen der Theorie der Übergangszustände (engl. transition state theory, TST) können Reaktionsraten über den Fluss reaktiver Trajektorien durch eine nur einmal durchstoßene Trennfläche (engl. dividing surface, DS) berechnet werden. Eine solche Trennfläche ist an der normal hyperbolischen invarianten Mannigfaltigkeit (NHIM) des Sattels verankert und trennt das System in Reaktanten und Produkte. Die NHIM ist dabei ein spezieller Unterraum des vollen Phasenraums und enthält Trajektorien, welche für alle Zeiten an die Sattelregion gebunden sind. Da diese Trajektorien somit weder zur Reaktanten- noch zur Produktseite gehören, bildet die NHIM einen Übergangszustand (engl. transition state, TS) der Reaktion. Für getriebene Systeme ist dieser zeitabhängig.

In dieser Arbeit werden anhand eines zweidimensionalen, getriebenen Modellsystems mehrere Methoden zur Berechnung von NHIM und DS im Phasenraum vorgestellt. Basierend auf der Dynamik in einer direkten Umgebung der NHIM werden außerdem verschiedene Ansätze zur Berechnung des zugehörigen Zerfalls der Reaktantenpopulation nahe des TS diskutiert.

Anschließend werden die vorgestellten Methoden auf ein realistischeres chemisches Modell angewandt, der getriebenen $\text{LiCN} \rightleftharpoons \text{LiNC}$ Isomerisationsreaktion, für welche sowohl die Potentialfläche als auch die Dipolfläche aus der Literatur bekannt sind [1, 2]. Ein wichtiges Resultat hierbei ist, dass das externe Treiben dieses Systems einen großen Einfluss hat, sowohl auf die Dynamik von Trajektorien in der NHIM, als auch auf den zugehörigen Zerfall der Reaktantenpopulation nahe des TS.



Abstract

In many cases the motion of individual atoms or molecules in chemical reactions can be fully described by classical mechanics on a Born-Oppenheimer potential energy surface. On this surface reactants are often separated from products via a rank-1 barrier. Such a barrier has one unstable degree of freedom, the reaction coordinate, and a given number of stable degrees of freedom, the orthogonal modes. A reactive trajectory on its pathway from the reactant to the product side will overcome the barrier usually in a close neighborhood of the saddle, the barrier region, which serves as a bottleneck for the reaction. Here, the framework of transition state (TS) provides both a qualitative and quantitative description of reaction rates using the flux of reactive trajectories through a recrossing-free dividing surface (DS) which separates reactants from products. In the barrier region, such a recrossing-free DS can be attached to the normally hyperbolic invariant manifold (NHIM). The NHIM is a special area of the full phase space of the system containing all trajectories which are mathematically bound to the saddle and will never leave to either the reactant or to the product side. Consequently, the NHIM serves as an intermediate state in between reactants and products and is often referred to as the TS. In time-dependently driven systems both the NHIM and the DS are time-dependent and the associated reaction rates will be influenced by this driving.

By means of a two-dimensional and time-dependently driven model system this thesis presents several methods to resolve both the time-dependent NHIM in the phase space close to the driven barrier and the DS attached to it. Based on the dynamics in a close neighborhood of these objects various methods to obtain the associated decay rates of reactant population close to the TS are introduced and compared.

In the second large part of this thesis these methods are applied to a more realistic model of a chemical reaction – the driven $\text{LiCN} \rightleftharpoons \text{LiNC}$ isomerization reaction. For this reaction analytical functions for both the potential energy surface and for the dipole surface are known from the literature [1, 2]. As a main result, the external driving has a significant influence on the dynamics of trajectories inside the NHIM and on the associated decay rates of reactant population close to the TS.



Contents

Inhaltsangabe	3
Abstract	5
1. Introduction and motivation	11
2. Reactions over a static energy barrier	17
2.1. Characteristics of a reaction in the context of transition state theory . . .	18
2.1.1. Open 1D systems	18
2.1.2. Closed 1D systems	21
2.1.3. Multidimensional rank-1 barriers	23
2.2. Reaction rates vs. decay rates	28
2.2.1. Kramers' rate	29
2.2.2. Decay rates of reactant population close to the transition state . .	31
3. Driven systems	35
3.1. Model system for a two-dimensional reaction over a driven rank-1 barrier	35
3.2. Time-periodically driven barriers	37
3.3. Revealing phase space structures	40
3.3.1. Lagrangian descriptor	40
3.3.2. Modifications of the Lagrangian descriptor	41
3.3.3. Generalization to multidimensional rank-1 barriers	45
3.4. Finding the NHIM	46
3.4.1. Binary contraction method	46
3.4.2. Interpolating the NHIM using machine learning techniques	48
3.5. Dynamics on the NHIM	52

4. Phase-space resolved decay rates for driven systems	57
4.1. Decay rates close to transition states in driven systems	57
4.2. Ensemble method	59
4.3. Local manifold analysis	61
4.3.1. The ensemble part	64
4.3.2. The DS part	67
4.4. Floquet method	69
4.5. Applications	71
5. Isomerization of LiCN	73
5.1. Mathematical description	73
5.1.1. A suitable coordinate system	73
5.1.2. Potential energy surface in the absence of external fields	77
5.1.3. Coupling to a time-periodically driven external field	81
5.2. Non-driven LiCN isomerization reaction	85
5.2.1. Analysis of reactive trajectories	85
5.2.2. Static NHIM and attached DS	91
5.2.3. Phase-space resolved decay rates close to the static transition state	93
5.3. Periodically driven LiCN isomerization reaction	97
5.3.1. Dynamics of periodically driven transition states	97
5.3.2. Instantaneous decay rates for trajectories on the driven NHIM . .	100
5.3.3. Phase-space resolved decay rates associated with the periodically driven transition states	104
6. Conclusion and outlook	109
A. Constants and equations for the LiCN potential	113
Bibliography	117
Zusammenfassung in deutscher Sprache	127
Curriculum Vitae	135
Danksagung	139



List of abbreviations

a_0	Bohr's radius
BCM	binary contraction method
DS	dividing surface
EOM	equations of motion
LD	Lagrangian descriptor
LMA	local manifold analysis
NHIM	normally hyperbolic invariant manifold
NN	neural network
PSOS	Poincaré surface of section
SCF	self consistent field
TD	time descriptor
TS	transition state
TST	transition state theory

1 Introduction and motivation

The term *reaction* is usually associated to chemistry where it describes chemical transformation of one set of chemical substances to another [3]. Indeed, such transformations are not limited to chemistry. When described in appropriate coordinates various reactions from one *state* to another can be found in a very broad range of problems, e. g., in atomic physics [4], solid state physics [5], cluster formation [6, 7], diffusion dynamics [8, 9], cosmology [10], celestial mechanics [11, 12], Bose-Einstein condensates [13–17], and chemical reaction dynamics [18–21] to name a few.

In many cases, the dynamics of a system can be described by classical equations of motion for selected coordinates driven by, e. g., a Born-Oppenheimer potential. Here, the framework of transition state theory (TST) [22–27] provides a powerful tool for the qualitative and quantitative description of these reactions from an initial state, called the *reactant* \mathcal{R} to a final state, denoted as *product* \mathcal{P} . Usually, these states appear as (local) minima in the corresponding potential energy surface and they are separated by an energy barrier or *saddle*. Typically, such a saddle is characterized by a rank-1 saddle point, which has one unstable direction, the *reaction coordinate* and an arbitrary number of stable degrees of freedom, called *orthogonal modes*.

In classically described autonomous Hamiltonian systems reactive trajectories must have at least enough energy to overcome a barrier close to its saddle point on their way from a reactant state to a product state. In other words, the local neighborhood of a saddle point in the phase space serves as a bottleneck for most of the reactive trajectories. Since their energy is minimal here, the corresponding reactive flux is slowest and, hence, to measure it is crucial for obtaining reaction rates. In consequence, a basic assumption of TST is that reaction rates are determined by what happens inside this bottleneck of such an energy barrier. Therefore, precise knowledge on the dynamics of reactive and non-reactive trajectories inside this bottleneck is of utmost importance and can usually be acquired by studying another very localized area of the phase space referred to as the NHIM [28, 29]. On the NHIM, trajectories are unstably bound to the vicinity of the barrier for infinite time at the boundary between reactants and products. Hence, this

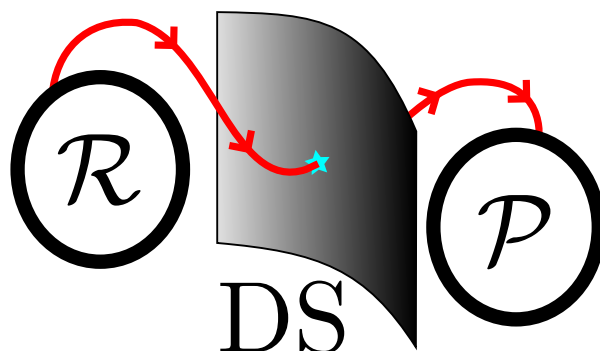


Figure 1.1.: Idealized sketch of a chemical reaction. Here, the reactant \mathcal{R} is separated from the product \mathcal{P} via the in general multidimensional and non-trivially curved DS . In the context of TST, a reaction happens exactly when and where (blue star) a reactive trajectory (red solid line) pierces the DS (gray surface).

intermediate state is often referred to as the TS.

To obtain the reactive flux and the associated rate one has to know exactly when and where a reactive trajectory *reacts*, or more precisely, pierces the boundary between reactants and products in the phase space, called DS , as sketched in Fig. 1.1. In case of a rank-1 saddle a simple but intuitive DS to separate reactants from products in the phase space would be a planar surface which is attached to the saddle point of an energy barrier and spanned perpendicular to its unstable degree of freedom in direction of the orthogonal modes. However, this is in general a rather strong approximation since such a planar DS is usually recrossed by many reactive trajectories on their way from reactants to products [22–25]. These recrossings lead to an overestimation of both the flux of reactive trajectories through such a planar DS as well as of the associated reaction rate and, consequently, these rates are in that case always an upper bound to the true reaction rate. To obtain accurate rates a DS has to be recrossing-free meaning that it should be crossed once and only once by each reactive trajectory. Thus, these recrossing-free DS s are usually multidimensional, non-trivially curved and their construction is a challenging task. Approximations can be found, e. g., in a variational TST approach by minimizing recrossings [30, 31] or by perturbation theory using normal form expansions [11, 32–40].

Advances in these methods allow one to examine non-driven chemical reactions with few degrees of freedom, e. g., the $H + H_2$ [35, 41] reaction or the LiCN [42] and ketene [43] isomerization reactions. In general, however, chemical reactions require representations with higher dimensionality which yields problems with regards to the convergence and the necessary numerical effort of these approximative approaches. Thus, an initial point of this thesis is to develop a fast and numerically exact method to obtain recrossing-free DS s – and not only for static, but also for time-dependently driven and multidimensional systems. This extension, however, is non-trivial. Whereas for a static system the sep-

aration between reactants and products can be done in configuration space, a DS for a time-dependently driven system needs to be constructed in the corresponding full phase space and will be time-dependent itself.

The generalization towards time-dependently driven systems is motivated by the desire to not only understand chemical reaction dynamics but to control these reactions by manipulating reaction rates. Thus, a main topic of this thesis is to understand the influences of an external driving on the reaction dynamics and the associated decay rates close to the TS, on the one hand by the means of a two-dimensional model chemical reaction and on the other hand by the driven isomerization reaction of LiCN.

First steps towards time-dependently driven systems have been done in a thermal environment [44–46]. Thereby, introducing friction to a system can be used to considerably simplify its description since the friction leads to a collapse of the dynamics on the NHIM towards a single trajectory in the long-term limit. This unique trajectory is then referred to as *the* TS trajectory and used as an attachment point of a planar DS which moves according to the noise in the system. Without this simplification, however, infinitely many trajectories are located on the NHIM of a time-dependently driven barrier and reactive trajectories may pierce the DS close to any of them. Hence, simply attaching a planar DS to a single trajectory is not sufficient anymore and the full dynamics of bound trajectories on the NHIM needs to be taken into account. A result of this thesis is that the specific position at which a reactive trajectory pierces the DS has a strong impact on the corresponding *phase space resolved* rate. In order to purely study this effect only driven systems without noise and friction are therefore considered.

This thesis starts introducing the characteristics of a reaction in the context of TST very basically by means of a static energy barrier in Chapter 2. Therein, not only most of the technical terms are introduced but also a classification of the obtained decay rates with respect to the well known Kramers’ rate is given. In Chapter 3 these concepts are generalized by introducing a model system with a time-periodically driven barrier. Here, various methods to reveal the phase space structures in the barrier region of a time-dependently driven rank-1 saddle are discussed and an efficient algorithm to obtain the associated time-dependent NHIM is introduced. To this NHIM a recrossing-free DS can be attached which can be used for rate calculation. In Chapter 4, three methods to calculate decay rates close to the TS of a time-dependently driven system are presented and applied to the driven model system. While, ultimately, they all yield the same rate, two of them are based on propagating reactive ensembles initialized close to the TS and a third method relies on an examination of the stability of trajectories on the NHIM. In Chapter 5 all methods are applied to the driven isomerization reaction of LiCN. Therefore, a mathematical model to describe this isomerization reaction in appropriate coordinates when coupled to a time-periodically driven external field is introduced. A special focus is here on the effects of the external driving on the obtained phase space resolved decay rates. In Chapter 6 follows the conclusion and outlook part of this thesis.

Essential parts of the Chapters 3 - 5 and related work have been published or will be published soon:

- *Chemical dynamics between wells across a time-dependent barrier: Self-similarity in the Lagrangian descriptor and reactive basins*,
A. Junginger, L. Duvenbeck, M. Feldmaier, J. Main, G. Wunner, R. Hernandez,
J. Chem. Phys. **147**, 064101 (2017)
- *Obtaining time-dependent multi-dimensional dividing surfaces using Lagrangian descriptors*,
M. Feldmaier, A. Junginger, J. Main, G. Wunner, R. Hernandez,
Chem. Phys. Lett. **687**, 194-199 (2017)
- *Binary contraction method for the construction of time-dependent dividing surfaces in driven chemical reactions*,
R. Bardakcioglu, A. Junginger, M. Feldmaier, J. Main, R. Hernandez,
Phys. Rev. E **98**, 032204 (2018)
- *Neural network approach to time-dependent dividing surfaces in classical reaction dynamics*,
P. Schraft, A. Junginger, M. Feldmaier, R. Bardakcioglu, J. Main, G. Wunner,
R. Hernandez,
Phys. Rev. E **97**, 042309 (2018)
- *Invariant Manifolds and Rate Constants in Driven Chemical Reactions*,
M. Feldmaier, P. Schraft, R. Bardakcioglu, J. Reiff, M. Lober, M. Tschöpe, A. Junginger, J. Main, T. Bartsch, R. Hernandez,
J. Phys. Chem. B **123**, 2070–2086 (2019)
- *Phase-space resolved rates in driven multidimensional chemical reactions*,
M. Feldmaier, R. Bardakcioglu, J. Reiff, J. Main, R. Hernandez,
J. Chem. Phys. **151**, 244108 (2019)
- *Neural network approach for the dynamics on the normally hyperbolic invariant manifold of periodically driven systems*,
M. Tschöpe, M. Feldmaier, J. Main, R. Hernandez,
Phys. Rev. E **101**, 022219 (2020)
- *Influence of external driving on decays in the geometry of the LiCN isomerization*,
M. Feldmaier, J. Reiff, R. M. Benito, F. Borondo, J. Main, R. Hernandez,
J. Chem. Phys. **153**, 084115 (2020)
- *Dynamics and decay rates of a time-dependent two-saddle system*,
J. Reiff, M. Feldmaier, J. Main, R. Hernandez,
Submitted to Phys. Rev. E (2020)

-
- *Thermal decay rates of an activated complex in a driven model chemical reaction*, R. Bardakcioglu, J. Reiff, M. Feldmaier, J. Main, R. Hernandez, Submitted to Phys. Rev. E (2020)
 - *Controlling decay rates in model chemical reactions through external driving*, J. Reiff, R. Bardakcioglu, M. Feldmaier, J. Main, R. Hernandez, In preparation (2020)

2

Reactions over a static energy barrier

A barrier is usually a certain area in an energy surface that divides a system into subsystems called the *reactant* \mathcal{R} and the *product* \mathcal{P} . In the context of TST, the term “reaction” describes the process in which such a trajectory pierces the DS, an in general high-dimensional boundary in the barrier region separating the reactant from the product. Sometimes, this separation is just done in the configuration space of a system. However, for a full dynamical description of driven systems as, e. g., the systems used in this thesis, the DS has to be created in their full phase space. When using a DS to calculate rates for an ensemble of many reactive trajectories, these rates are exact only if the DS is free of recrossings. Hence, any reactive trajectory should cross the DS once, and only once.

For autonomous Hamilton systems, a recrossing-free DS can be attached to the NHIM of a barrier. The NHIM is an unstable subspace of the full phase space where trajectories are trapped in the barrier region both forward and backward in time. This fact has been known in literature and the construction of the corresponding NHIM was done, e. g., using normal form expansions [11, 32–40].

In this chapter, the fundamental terms and definitions necessary to characterize such reactions in autonomous systems are introduced. Therefore, the underlying geometry of reactive and non-reactive trajectories in the barrier-region is elaborated in Sec. 2.1. Based on this geometry, the NHIM of such a system can be constructed to which a recrossing-free DS can be attached. Having obtained a recrossing-free DS in principle allows to calculate reaction rates by propagating ensembles of reactive trajectories over the barrier. However, the term “rate” needs to be specified here, as its meaning is not unique. On the one hand, an ensemble of thermal particles could be trapped in a deep potential basin and some of these particles may escape the basin (very rarely) over an energy barrier. The rate associated with this escape of particles is called *Kramers’ rate* [47, 48]. On the other hand, the term “rate” in the context of TST is associated with the decay rate of reactant population close to the TS of a barrier. The differences between these two different types of rates are elaborated in Sec. 2.2.

2.1 Characteristics of a reaction in the context of transition state theory

To characterize a reaction in the context of TST, the phase space geometry in the barrier region is important. Based on the dynamics of trajectories close to a saddle this region can be divided into different reactive and non-reactive areas. The boundaries of these areas, called the *stable* and the *unstable manifold* intersect on the NHIM. To this intersection, a recrossing-free DS can be attached. This section starts with a very basic description of the phase space geometry in the barrier region of an open one-dimensional system in Sec. 2.1.1. Here, the concept of the NHIM and the attached stable and unstable manifold is introduced in a simple way. Thereby, a focus is on the difference between an open and a closed system in Sec. 2.1.2, as for the latter the meaning of having a “recrossing-free” DS changes significantly. In Sec. 2.1.3 follows the generalization to higher rank barriers, having a single unstable direction and an arbitrary number of stable degrees of freedom.

2.1.1 Open 1D systems

A one-dimensional potential energy surface with a single barrier and open reactant \mathcal{R} and product \mathcal{P} basins is the most simple example to model reactions in an autonomous Hamiltonian system, as sketched in Fig. 2.1 (a). Here, a single position coordinate x , called the *reaction coordinate*, is used to describe the system and the origin of coordinates is set to the maximum of the barrier without loss of generality. The use of the word “open” is to indicate, that every trajectory leaving the barrier to either the reactant side $x \rightarrow -\infty$ or to the product side $x \rightarrow \infty$ never returns, when propagated according to the corresponding Hamiltonian equations of motion. Further, the reactant and the product basins are allowed to be unequally deep.

The separation into reactants \mathcal{R} and products \mathcal{P} is given by the reaction coordinate $x = 0$ of the maximum of the barrier, called the *saddle point*. A trajectory launched on the reactant side \mathcal{R} with an initial momentum towards the barrier is considered *reactive*, if its energy is high enough to pass the saddle point to the product side \mathcal{P} . Conversely, a trajectory launched at the product side that is inversely reacting back to the reactant side is also considered reactive. Consequently, the saddle point not only separates the system into reactants \mathcal{R} and products \mathcal{P} , but also characterizes reactive trajectories as those which have enough energy to pass this maximum of the barrier. However, if the energy barrier is too high or the initial kinetic energy too small, the trajectories are rejected to their originating side and, since the potential is open, never return to the barrier. Such trajectories, which are not able to pass the maximum of the barrier are denoted *non-reactive*.

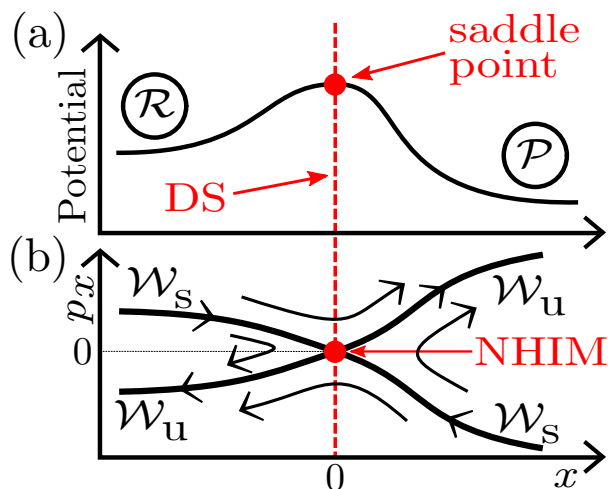


Figure 2.1.: (a) Sketch of an energy barrier of an open one-dimensional system described via the *reaction coordinate* x , with the origin of coordinates set to $x = 0$ at the maximum of the barrier. Here, at the *saddle point*, a recrossing-free DS separates the system into *reactant* \mathcal{R} and *product* \mathcal{P} . (b) Using the conjugated momentum p_x yields the same situation in the phase space (x, p_x) . It is separated by the stable \mathcal{W}_s and the unstable \mathcal{W}_u manifold into four different areas, which are indicated by the black arrows symbolizing the predominant flux of trajectories. The intersection of these manifolds, located exactly at the same position $x = 0$ as the saddle point, is a hyperbolic fixed point. This fixed point is also known as the NHIM of this system.

The classification into reactive and non-reactive trajectories is valid for all possible trajectories of the system except for the single trajectory resting at the saddle point at $x = 0$ in Fig. 2.1. Although being unstable, this trajectory never falls down to neither the reactant nor to the product side and, therefore, it is in some kind of intermediate state between reactant \mathcal{R} and product \mathcal{P} . This state is called the *transition state* (TS). The TS is *unstable*, meaning that any deviation from it, even if infinitesimally small, grows exponentially fast in its local vicinity [49]. Consequently, such a departing trajectory “falls down” to either the reactant or to the product side.

An important requirement for the trajectory in the TS is that it is resting exactly on top of the static barrier. Having any initial momentum here makes a trajectory reactive as it falls down to one side of the barrier forward in time and it has climbed up the barrier from the other side in the past. This simple argumentation is to illustrate, that the description of the TS in position space, namely at the top of the barrier, is not sufficient and additional information on its momentum is needed.

In Fig. 2.1 (b), an extended representation of the simple one-dimensional barrier in the phase space (x, p_x) is given, including not only the position coordinate x , but also the conjugated momentum p_x . A description in the phase space naturally provides

a division into reactive and non-reactive regions. This can be explained by a simple example: Let us assume a trajectory is launched on the reactant side $x < 0$. If its initial momentum is large and oriented towards the barrier, $p_x \gg 0$, its energy is high enough to pass the barrier. This trajectory is considered reactive. When successively lowering the initial momentum, at some point the trajectory has no longer enough energy to cross the barrier. Even though it approaches the barrier for initial $p_x > 0$ to some extent, it “falls down” to the same side again and never returns since the potential is open. If the momentum is negative, $p_x < 0$ for $x < 0$, trajectories immediately leave the barrier region when propagated forward in time. However, two cases for the propagation backward in time have to be distinguished. Trajectories with large negative momentum have crossed the barrier in the past (reactive trajectories), whereas trajectories with small negative momentum have been reflected at the barrier, and hence, are considered non-reactive.

Since these considerations are conversely also valid for any trajectory at $x > 0$, the full phase space in Fig. 2.1 (b) can be subdivided into four disjunct areas, indicated by the thin black arrows. These arrows illustrate the predominant flux of trajectories forward in time in the respective area. The top and the bottom area are reactive either from reactant to product or vice versa, the left and the right area are non-reactive and trajectories in this region of the phase space are being reflected at the barrier.

The four areas of different reactivity are separated from each other via curved boundaries, called the stable \mathcal{W}_s and the unstable manifolds \mathcal{W}_u . In case of a one-dimensional problem, these manifolds are just curves intersecting at the position $x = 0$ of the saddle point, as indicated with thick black lines in Fig. 2.1 (b). In general, and thus especially for higher-dimensional problems as described in Sec. 2.1.3, these manifolds themselves become multidimensional objects. They have locally the structure of Euclidean space and can be imagined as a multidimensional surface embedded in the full phase space [49].

A trajectory initialized somewhere on the stable manifold \mathcal{W}_s approaches the intersection of \mathcal{W}_s and \mathcal{W}_u asymptotically fast as $t \rightarrow \infty$, when propagated forward in time [49]. Conversely, a trajectory initialized somewhere on the unstable manifold \mathcal{W}_u departs from this intersection asymptotically fast and asymptotically approaches this intersection as $t \rightarrow -\infty$.

The intersection of the stable and the unstable manifold¹ is again a manifold, called the *normally hyperbolic invariant manifold* (NHIM) [11, 32–40, 49]. Here, the term *normally hyperbolic* is a specification of the dynamics close to the NHIM in terms of Lyapunov exponents which are a measure on how fast initially nearby trajectories separate from each other. To classify the NHIM as normally hyperbolic implies that any stretching and contraction rates of the dynamics on the NHIM are smaller than the stretching and contraction rates away from the NHIM [41]. Consequently, the NHIM is *unstable*, meaning that any (possibly infinitesimally small) deviation from it grows exponentially fast in time in its local vicinity [49]. On the other hand, any trajectory precisely initialized on the NHIM will stay in this unstable subspace of the full phase space when propagated

¹Actually, it is the intersection of the closures of both manifolds.

both forward and backward in time. Hence, the NHIM is *invariant* under the dynamics of a system. In the chemistry community the NHIM is often called the TS. In this thesis, I will use both terms interchangeably and depending on the context of a statement.

In case of a one-dimensional static barrier according to Fig. 2.1 (b), the NHIM is a phase space point located at the position $x = 0$ of the maximum of the barrier with momentum $p_x = 0$. Here, the benefit of such a complicated description of the intersection of the stable and the unstable manifold is not obvious since the only existing coordinate is the unstable reaction coordinate x . In multidimensional systems, however, this reaction coordinate may be coupled to various *orthogonal modes* according to Sec. 2.1.3. Here, these definitions will become more comprehensible.

To the NHIM in the phase space of Fig. 2.1 (b), a vertical line can be attached, a *dividing surface*² (DS), which separates the phase space into reactants \mathcal{R} and products \mathcal{P} . Usually, such a DS is *recrossing-free* for a static and one-dimensional barrier. Hence, any reactive trajectory is going to cross it only once on its pathway from reactant to product or vice versa. Non-reactive trajectories, however, never cross this DS and therefore stay in their respective state of a system.

Choosing a vertical DS implies the assumption that it is recrossing-free, independent of the reactive momentum p_x . This assumption does not hold in general and exceptions are known [38, 50–52]. In very nonlinear systems, where the stable and the unstable manifolds are strongly deformed such a vertical DS might lead to unwanted recrossings, especially for trajectories with high energy, which cross the DS far away from the NHIM. However, the choice of a vertical DS can always be justified if unwanted recrossings are absent in dynamical simulations as has been done, e. g., in Refs. [29, 53, 54]. For many systems of practical relevance the use of a vertical DS is adequate. Usually, many other DSs that are located sufficiently close to the vertical line are also recrossing-free and choosing a vertical DS is not critical.

For a static one-dimensional system as in Fig. 2.1 (a) the NHIM shares the same position $x = 0$ as the saddle point. In more general cases, e. g., in multidimensional systems according to Sec. 2.1.3 or if a barrier is time-dependently driven, as explained in Chap. 3, the NHIM detaches from the location of the saddle point. The importance of constructing a DS in the phase space of a system will then be evident. Here, it is only mentioned for the sake of completeness.

2.1.2 Closed 1D systems

An open system, like the one introduced in Fig. 2.1 is called “open”, since trajectories leaving the barrier to either the reactant \mathcal{R} or the product \mathcal{P} side never return towards the barrier. The DS attached to the saddle point in such static and open systems usually

²Naming a line a surface seems odd here. However, when doing the generalization to multidimensional systems, the separation between reactants and products becomes a multidimensional hypersurface, i. e., the DS. Since a line is a special case of a surface, the multidimensional nomenclature is kept here to avoid confusion.

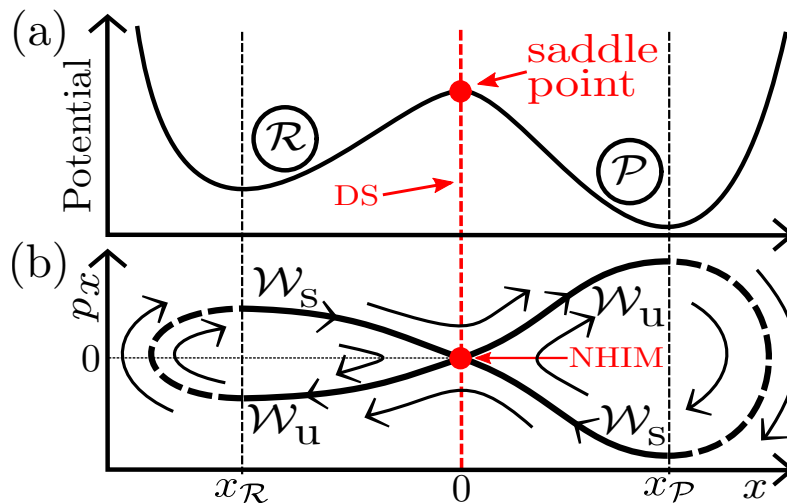


Figure 2.2.: (a): Sketch of an energy barrier of a closed one-dimensional system described via the reaction coordinate x , with the origin of coordinates set to $x = 0$ at the maximum of the barrier. Here, at the saddle point, a *locally recrossing-free* DS separates the system into reactant \mathcal{R} and product \mathcal{P} . (b): phase space view (x, p_x) . Within the barrier region $x \in [x_{\mathcal{R}}, x_{\mathcal{P}}]$, the situation looks similar to an open system, as explained in Fig. 2.1 (b). Outside this region, however, the stable and the unstable manifold are connected to the full separatrix in between reactive and non-reactive trajectories. From these outer boundaries of the reactant and product basins *global recrossings* arise and the associated trajectories, again emphasized as thin black arrows, pierce the DS attached to the NHIM infinitely many times.

is recrossing-free. Consequently, reactive trajectories, having enough energy to overcome the barrier are going to cross it only once, whereas non-reactive trajectories never cross it. In systems with closed reactant \mathcal{R} and product \mathcal{P} basins, however, this fact changes fundamentally when regarding reactive trajectories.

A very simple example for a closed 1D system is given by a double-well potential as, e. g., sketched in Fig. 2.2 (a). Here, the reactant \mathcal{R} and product basins \mathcal{P} are closed, meaning that the potential energy in both basins is not monotonously decreasing in the direction away from the barrier but starts to increase again after passing the minimum of a basin. If the increase of the potential at its outer boundaries goes to infinity, as sketched in the example of Fig. 2.2, any trajectory once initialized somewhere inside these boundaries is trapped forever. In a real system, however, the increase of the potential energy surface would cease somewhere and even further away from the barrier, it would decrease again. However, since the maximum in between this in- and decrease would then be an additional (and possibly much higher) barrier other than the one at $x = 0$, this barrier could again be treated using the methods explained here, just with a different origin of coordinates.

Since the barrier and the associated potential regarded here are static, the total energy of trajectories is conserved. If the energy of a trajectory is smaller than the potential energy of the maximum of the barrier, it is not able to cross the associated DS and, hence, it is considered non-reactive. Here, nothing has changed when compared to an open one-dimensional and static system according to Sec. 2.1.1. However, if a trajectory has enough energy to overcome the barrier once in a closed and static system, it can in principle overcome the barrier infinitely many times since it is reflected again and again at the outer boundaries of the potential. This can be easily seen in the phase space (x, p_x) , where according to Fig. 2.2 (b) the stable and the unstable manifold outside a certain *barrier region* $x \in [x_{\mathcal{R}}, x_{\mathcal{P}}]$ are connected and form the *separatrix*, which separates reactive from non-reactive trajectories [49]. As indicated with the thin black arrows, the flux field of trajectories outside of the barrier region approximately follows the separatrix. Here, the former reactive trajectories are globally reflected back towards the barrier. This leads to multiple crossings, the *global recrossings*, of the DS attached to the NHIM – which was said to be recrossing-free in an open system. Consequently, solely the question of finding a globally recrossing-free DS is pointless for closed systems. For a comprehensive further discussion of global recrossings see, e. g., Ref. [55].

Inside the barrier region $x \in [x_{\mathcal{R}}, x_{\mathcal{P}}]$, however, the phase space (x, p_x) of the closed one-dimensional and static system in Fig. 2.2 (b) looks very similar to the phase space of an open system according to Fig. 2.1 (b). A reactive trajectory entering the barrier region continues its pathway over the barrier as described by the associated equations of motion (EOM). It pierces the DS attached to the NHIM only once, as long as the size of the barrier region is properly chosen. In that case, the DS of a bound system is said to be *locally recrossing-free*. An intuitive choice is to set the boundaries of the barrier region to the minima of the reactant and product basins, as has been done in Fig. 2.2 (a). Other choices having a smaller saddle region are also possible and may be numerically easier to handle, especially for multidimensional and time-dependent systems. For a more detailed discussion on the influence of choosing a barrier region, see Sec. 3.3.

2.1.3 Multidimensional rank-1 barriers

Everything said so far was limited to a one-dimensional system, which is an idealization taking into account only the unstable degree of freedom of a barrier. More realistic systems, however, are usually not restricted to a single degree of freedom, since e. g., the three dimensions of space or internal degrees of freedom in a molecule require a multidimensional description of reactions. Still, TST provides a set of tools to examine and understand these multidimensional reactions, at least for a special type of barrier, the *rank-1 saddle*. In an n -dimensional energy surface, a rank-1 saddle is a barrier which has one unstable degree of freedom, again called the *reaction coordinate* just like in the one-dimensional case, and $(n - 1)$ stable degrees of freedom, referred to as *orthogonal modes*. Here, the multidimensional generalization of the saddle point is located at the maximum of the barrier with respect to its unstable direction and at the minimum of

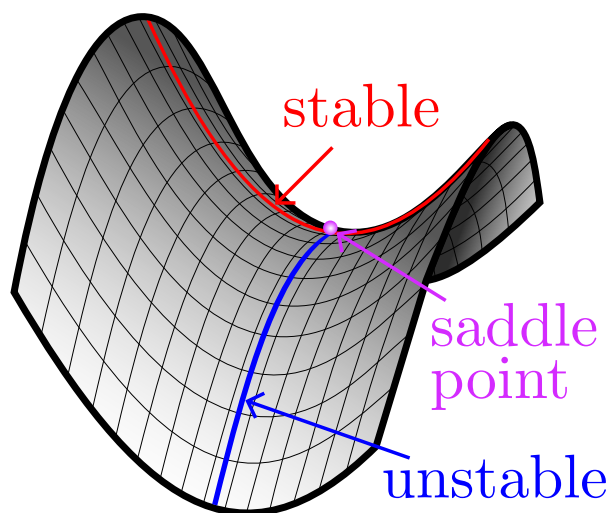


Figure 2.3.: Sketch of a two-dimensional rank-1 barrier. Here, the movement of trajectories is bound in the stable direction of the orthogonal mode (red), while they are balancing on the barrier in the unstable direction (blue). The saddle point (purple) is located at the maximum of the barrier with respect to the unstable direction and at its minimum in the orthogonal mode.

the barrier in any orthogonal mode. Exemplary, a sketch of the energy surface of a two-dimensional rank-1 saddle is shown in Fig. 2.3, having an unstable direction (blue) and a stable orthogonal mode (red).

Changing to multidimensional systems comes with the huge disadvantage that the associated phase space is hard to imagine, and thinking of the location of surfaces or manifolds prescribed by the dynamics in this high-dimensional phase space is even harder. Often, the problems of imagining things are tackled by resorting to their strict mathematical description. However, this usually makes life not easier at first hand. That is why the following subsection is written as simple and descriptive as possible, without going too much into mathematical details. The herein interested reader is referred to, e. g., the books of Wiggins [49, 56] or the papers of Fenichel [57–59], who introduced the concept of the NHIM in 1971 and the following years.

The basic idea when dealing with a rank-1 barrier in a multidimensional system is the same as in the one-dimensional case: an in general non-trivially curved recrossing-free DS is sought to divide the full phase space of a reactive system into reactants \mathcal{R} and products \mathcal{P} . Since the phase space of a system with n degrees of freedom is $2n$ -dimensional, this DS has to be $(2n-1)$ -dimensional. Once found, it allows one to classify the dynamics of the system since reactive trajectories are able to cross this DS and non-reactive trajectories are not. For open systems this DS is globally recrossing-free and for closed systems just locally recrossing-free as discussed in Sec. 2.1.2 for a one-dimensional system but still valid in higher dimensions.

The classification of trajectories into being reactive or non-reactive is not complete as there exists an intermediate state, called the TS, in between reactants and products. In a static one-dimensional system according to Sec. 2.1.1, this TS contains just a single unstable trajectory, which is resting at the saddle point on top of the barrier. For a multidimensional rank-1 saddle, however, trajectories in the TS are able to move in direction of the stable orthogonal modes, while “balancing” in the unstable direction on the barrier, see Fig. 2.3. Since the movement in the orthogonal modes is in principle not limited, the TS of a higher-dimensional system contains not a single, but infinitely many trajectories which are stable with respect to the orthogonal modes and unstable in the reaction degree of freedom.

In a mathematician’s view on the phase space, all trajectories of the TS are bound to the NHIM of the rank-1 barrier. The dynamics close to this NHIM is again prescribed by its stable \mathcal{W}_s and its unstable \mathcal{W}_u manifold, containing all trajectories that asymptotically approach the NHIM at $t \rightarrow \infty$ forward in time or at $t \rightarrow -\infty$ backward in time. Again, these two manifolds \mathcal{W}_s and \mathcal{W}_u subdivide the $2n$ -dimensional phase space in the barrier region of a multidimensional rank-1 saddle into reactive and non-reactive areas. Therefore, the stable and the unstable manifolds are $(2n - 1)$ -dimensional, and their intersection, the NHIM, is $(2n - 2)$ -dimensional.

To parametrize the NHIM, we express the reaction coordinate x and its conjugated momentum p_x as a function of the $(n - 1)$ -dimensional orthogonal modes \mathbf{y} and their respective conjugated momenta \mathbf{p}_y . Consequently, the NHIM of an n -dimensional rank-1 barrier is a mapping of the $(2n - 2)$ -dimensional subspace of the full phase space described by the orthogonal modes $(\mathbf{y}, \mathbf{p}_y)$ on the reaction coordinates (x, p_x)

$$\text{NHIM} : \begin{aligned} & \mathbb{R}^{2n-2} \rightarrow \mathbb{R}^2, \\ & (\mathbf{y}, \mathbf{p}_y) \mapsto (x(\mathbf{y}, \mathbf{p}_y), p_x(\mathbf{y}, \mathbf{p}_y)), \quad n \geq 2. \end{aligned} \quad (2.1)$$

For fixed orthogonal modes $(\mathbf{y}, \mathbf{p}_y)$, the projections of the $(2n - 1)$ -dimensional manifolds \mathcal{W}_s and \mathcal{W}_u appear as linear fibers in an (x, p_x) cross section of the full phase space, see Fig. 2.4.

Similar to the equivalent phase space of a one-dimensional barrier in Fig. 2.1 (b), these fibers cross each other in a point-like intersection. Whereas the full NHIM was given by this particular intersection in the one-dimensional case, here, the intersection of the linear fibers is just a single point $(x, p_x)^{\text{NHIM}}(\mathbf{y}, \mathbf{p}_y)$ of the $(2n - 2)$ -dimensional NHIM, parametrized by the orthogonal modes $(\mathbf{y}, \mathbf{p}_y)$. In other words, for a specific position $(\mathbf{y}_i, \mathbf{p}_{y,i})$ in the orthogonal modes, the associated position x_i^{NHIM} and $p_{x,i}^{\text{NHIM}}$ of the NHIM is given by the intersection of the linear fibers of \mathcal{W}_u and \mathcal{W}_s in the corresponding (x, p_x) -cross section of the full phase space. Since the NHIM is, depending on the details of the dynamics, a non-trivially curved manifold, this position x_i and $p_{x,i}$ is usually different for various positions i in the orthogonal modes.

Exemplary, this fact is visualized in the sketch in Fig. 2.5 for the two-dimensional NHIM of a rank-1 saddle in a system with two degrees of freedom (x, y) and a four-dimensional phase space (x, y, p_x, p_y) , where x approximates an unstable reactive degree

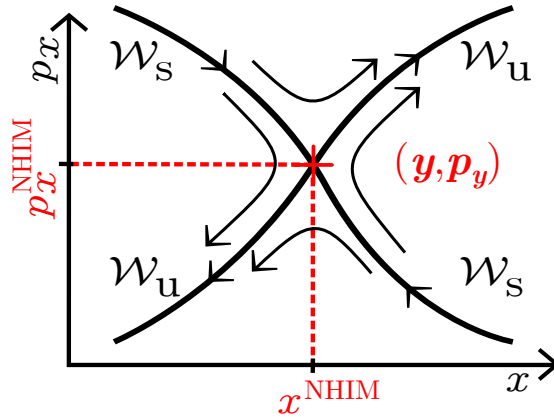


Figure 2.4.: Cross section (x, p_x) of the full phase space close to an n -dimensional rank-1 barrier with reaction coordinate x and $(n - 1)$ orthogonal coordinates \mathbf{y} . Here, the actually $(2n - 1)$ -dimensional stable \mathcal{W}_s and unstable \mathcal{W}_u manifolds appear as linear fibers, intersecting in a point $(x^{\text{NHIM}}, p_x^{\text{NHIM}})(\mathbf{y}, \mathbf{p}_y)$ of the $(2n - 2)$ -dimensional NHIM which depends on the chosen position $(\mathbf{y}, \mathbf{p}_y)$ of the orthogonal modes.

of freedom and y a stable orthogonal mode. The fibers of the stable \mathcal{W}_s and the unstable \mathcal{W}_u manifolds of the NHIM are displayed for three cross sections (x, p_x) , chosen at different, but for each cross section constant, positions $(\mathbf{y}, \mathbf{p}_y)$ in the orthogonal mode. For each cross section, the fibers intersection yields a position x (and p_x) on the NHIM. Since it is not possible to draw the full four-dimensional phase space, only a representation of the NHIM, $x^{\text{NHIM}}(\mathbf{y}, \mathbf{p}_y)$ in the three-dimensional space (x, \mathbf{y}, p_y) is shown, omitting the reactive momentum p_x . The purpose of Fig. 2.5 is to visualize, that the full NHIM is given by the continuous connection of all intersections of the fibers of \mathcal{W}_u and \mathcal{W}_s , obtained in the respective cross section (x, p_x) at any position $(\mathbf{y}, \mathbf{p}_y)$ of the orthogonal modes.

In a multidimensional autonomous system, the NHIM of a rank-1 saddle can be approximately constructed using normal form expansions [11, 32–40, 60]. Therefore, the EOM are expanded in the vicinity of a fixed point, e. g. the saddle point of a barrier, and transformed to *normal form coordinates*, where they appear in a very simple form. This perturbative procedure is only valid in a local area close to the barrier. However, by looking for individual points of the NHIM as schematically described in Fig. 2.5, the full NHIM of a multidimensional rank-1 saddle can be revealed numerically exact in its barrier region. Therefore, two methods are discussed in the present work. The first one is based on identifying the stable and unstable manifold using Lagrangian descriptors, as explained in Sec. 3.3. The second, much faster method, the *binary contraction method* according to Sec. 3.4.1, relies on the dynamics of reactive and non-reactive trajectories in the barrier region. Both methods share the common advantage, that they can also be applied to time-dependently driven barriers, which are discussed in Chap. 3.

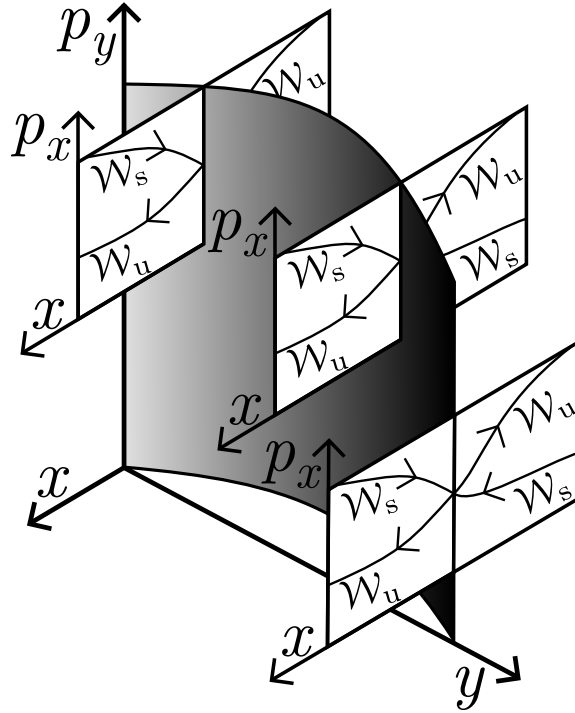


Figure 2.5.: Exemplary visualization of the two-dimensional NHIM of a rank-1 barrier in a system with two degrees of freedom (x, y) and, hence, a four-dimensional phase space (x, y, p_x, p_y) . Here, x approximates an unstable and y a stable degree of freedom. For three cross sections (x, p_x) , chosen at different, but in each case constant, positions (y, p_y) in the orthogonal mode, the linear fibers of the stable \mathcal{W}_s and unstable \mathcal{W}_u manifolds of the NHIM are shown. Their intersection yield the corresponding point $x^{\text{NHIM}}(y, p_y)$ on the NHIM. By continuously connecting all intersections of the fibers of \mathcal{W}_u and \mathcal{W}_s given at any position (y, p_y) , a full representation of the two-dimensional NHIM can be obtained, which is shown as a black shaded surface $x^{\text{NHIM}}(y, p_y)$ in the three-dimensional space (x, y, p_y) .

Having found the NHIM of a multidimensional rank-1 saddle with either method allows for the construction of a locally recrossing-free DS in the barrier region

$$x^{\text{DS}}(\mathbf{y}, \mathbf{p}_y) = x^{\text{NHIM}}(\mathbf{y}, \mathbf{p}_y), \quad (2.2)$$

which is vertically attached to the NHIM and independent of the reactive momentum p_x . As already discussed in the one-dimensional case in Sec. 2.1.1, this is certainly a simplification since there is no general proof that such a vertical recrossing-free DS should exist and exceptions are known [38, 50–52]. However, many systems of practical relevance are not too nonlinear and hence, the stable and unstable manifolds are not strongly deformed in the barrier region. Consequently, using a vertical DS is adequate

in many case, plus, can always be verified in a dynamical simulation, as has been done, e. g., in Refs. [29, 53, 54].

2.2 | Reaction rates vs. decay rates

The term *rate* in the context of a reaction between two (meta)-stable states of a system can have various meaning. Historically, it is associated to the escape rate of Brownian particles over a barrier in a thermal system. Therefore, a large ensemble of these particles is initialized close to thermal equilibrium and far away from the barrier in a (deep) potential well. Since the Brownian motion allows individual particles to gain and loose energy, some of them may, very rarely, have enough energy to escape the well over a barrier. The associated rate in this diffusion model of a simple chemical reaction is referred to as *Kramers' rate* [47, 48].

However, when calculating rates in the context of TST the term “rate” is to be understood differently. Here, it describes the decay of the activated complex between reactant and product, or in other words, the decay of reactant population close to the TS. Since the TS is unstable with respect to the unstable degree of freedom of a barrier, a trajectory having just the smallest deviation from it departs to either the reactant or the product side. This exponentially fast departure of trajectories from the unstable TS is associated with a rate, i. e., the *decay rate of reactant population* close to the TS.

When compared to reactions according to Kramers' rate, the decay rates of reactant population in TST are obtained for a rather localized area in the phase space close to the NHIM of a rank-1 saddle. Here, these decay rates are obtained as a sole property of the local dynamics and depend only on the EOM and the specific shape of the barrier. A description of a thermal state in the potential wells is, in contrast to Kramers' rate, not included and therefore, a decay rate of reactant population in a close neighborhood of the NHIM is by construction independent of a specific reactive ensemble. In TST, these decay rates can be obtained with various methods which rely on propagating ensembles of reactive trajectories, either according to the full dynamics prescribed by the EOM, see the ensemble method in Sec. 4.2, or by skipping this ensemble propagation taking advantage of the linearized properties of the dynamics in a close neighborhood of the NHIM. The corresponding method, referred to as *local manifold analysis* is introduced in Sec. 4.3. An alternative method giving access to these decay rates is based on an analysis of the stability of trajectories bound to the NHIM. This *Floquet method* is explained in Sec. 4.4.

To be able to understand the differences of a reaction rate according to Kramers and a decay rate of reactant population in a local neighborhood of the TS, in Sec. 2.2.1 a brief overview on the assumptions made for obtaining Kramers' rate is given. Afterwards, the concept of these decay rates is introduced in Sec. 2.2.2 for one- and for multidimensional rank-1 barriers.

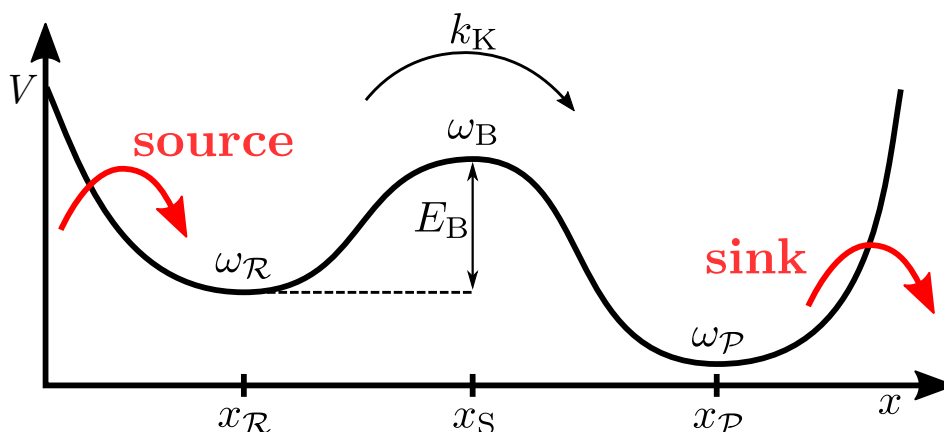


Figure 2.6.: One-dimensional asymmetric double well potential energy surface $V(x)$. In the reactant well at $x_{\mathcal{R}}$ and in the product well at $x_{\mathcal{P}}$, as well as at the position of the saddle point $x_{\mathcal{S}}$ the potential is assumed to be approximately harmonic in a small neighborhood with angular frequencies $\omega_{\mathcal{R}}$, $\omega_{\mathcal{P}}$ and $\omega_{\mathcal{B}}$, respectively. The height of the barrier is $E_{\mathcal{B}}$, measured from the bottom of the reactant well. On the reactant side, there is a source, inserting classical Brownian particles with an energy much smaller than the barrier energy. Hence, these particles thermalize fast. Very rarely, some of these particles gain enough energy from the fluctuations such that they are able to pass the barrier to the product side. Here, they are instantaneously taken away by a sink. After a transient time, the system reaches a steady state where the flux of particles to the product side is approximately constant. Now, the associated steady state escape rate of these classical Brownian particles is referred to as Kramers' rate $k_{\mathcal{K}}$.

2.2.1 Kramers' rate

In 1940 Kramers published an article about Brownian motion in a force field and a diffusion model of chemical reactions [47]. Therein, he derived his famous rate formula for the steady state escape rate of classical Brownian particles which move in a one-dimensional asymmetric double-well potential. Since such an escape rate is fundamentally different to a decay rate of the TS, the purpose of this subsection is to give a brief overview on what is the famous Kramers' rate and why it is so different when compared to the decay rates calculated in the present work. A reader interested in a more detailed and mathematical description of Kramers' rate, however, is referred to Ref. [48], which gives an in-depth overview on reaction rate theory and serves as the theoretical background of this subsection.

As sketched in Fig. 2.6, Kramers used a one-dimensional double-well energy surface $E(x)$, to describe a simple chemical reaction over a barrier with saddle point at position $x_{\mathcal{S}}$. Close to $x_{\mathcal{R}}$, there is the reactant well, containing classical particles of mass m .

2. Reactions over a static energy barrier

Their coupling to any remaining degrees of freedom as well as to other molecules of a solvent with temperature T is simply described by a linear damping force $-m\gamma\dot{x}$ and a fluctuating force $\xi(t)$. Here, γ is a constant damping rate. Hence, these particles can be described by a Langevin equation

$$m\ddot{x} = -\frac{\partial E(x)}{\partial x} - \gamma m\dot{x} + \xi(t) . \quad (2.3)$$

The fluctuating force $\xi(t)$ is assumed to be white noise with zero mean $\langle \xi(t) \rangle = 0$ according to the fluctuation-dissipation theorem

$$\langle \xi(t)\xi(t') \rangle = 2m\gamma k_B T \delta(t-t') , \quad (2.4)$$

where $k_B = 1.380649 \times 10^{-23}$ J/K is the Boltzmann constant [61]. On the reactant side, there is a source, which continuously supplies the reactant well with particles having an energy considerably lower than the barrier energy. Inside the well, these particles thermalize very fast. Due to the fluctuations, some of them may eventually gain enough energy to overcome the barrier to the product side. Here, the separation of timescales is important, meaning that the timescale associated with the escape of reactive particles over the barrier is much larger than any other timescale relevant for the system's dynamics. Such other timescales may be, e. g., how fast the particles thermalize or how fast their relaxation time after crossing the barrier is. Therefore, the friction γ should be strong in the system.

On the product side of the barrier, there should be a sink, meaning that any particle which was able to cross the barrier to the product side close to x_P is taken out of the system. Consequently, after a transient time, a stationary situation emerges, where the flux j of escaping particles over the barrier is given by the product of the escape rate k_K from reactant to product and the population N_R in the reactant well or, equivalently,

$$k_K = \frac{j}{N_R} . \quad (2.5)$$

This spatial-diffusion-controlled *Kramers' rate* k_K could be derived by Kramers in 1940 to [47, 48]

$$k_K = \frac{\lambda}{\omega_B} \left[\frac{\omega_R}{2\pi} \exp\left(-\frac{E_B}{k_B T}\right) \right] \quad \text{with } \lambda = -\frac{\gamma}{2} + \sqrt{\omega_B^2 + \frac{\gamma^2}{4}} , \quad (2.6)$$

where E_B is the height of the barrier relative to the bottom of the product well. Here, the energy surface is approximately assumed to be harmonic with angular frequency $\omega_B^2 = -E''(x_B)/m$ around a small neighborhood of the saddle point and angular frequency $\omega_R^2 = E''(x_R)/m$ near the bottom of the reactant well. Hence, the thermal state in the reactant well is directly included in Kramers' rate formula, a fact that is completely different for decay rates of the TS, which are independent of a specific reactive ensemble.

2.2.2 Decay rates of reactant population close to the transition state

In the concept of TST a system has at least two stable states, referred to as reactants and products. Usually, these states are separated by an energy barrier, or more specifically, a rank-1 saddle, which has to be passed by reactive trajectories on their way from one stable state to the other. In the barrier region, in between these two stable states, there exists a third state, the TS, which is unstable. As introduced in Sec. 2.1, this TS contains just a single trajectory for a one-dimensional system or an infinite amount of trajectories in the case of a multidimensional rank-1 barrier. Any trajectory in the TS is trapped forever, meaning that it can never be classified to be reactant or product, neither forward, nor backward in time. Trajectories initialized in a local neighborhood of the unstable TS depart exponentially fast from it to either the reactant or the product side of the barrier. This departure is associated with a specific rate, the decay rate of reactant population close to the TS.

If a system is only one-dimensional with a static energy barrier, the TS contains just the zero-dimensional trajectory resting exactly at saddle point on top of the barrier. In the phase space, this unstable state corresponds to the NHIM of the rank-1 saddle which is located at the intersection of its stable and unstable manifold, see Sec. 2.1. Since this NHIM is unstable, any trajectory having just a small deviation from it, even if infinitesimally small, departs exponentially fast to either the reactant or the product side of the barrier – at least in a certain neighborhood of the NHIM [49]. Consequently, a number $N_{\text{react}}(t_0)$ of reactants, initially located closely to the TS at a time t_0 on the reactant side, decreases exponentially fast in time t to the product side according to

$$N_{\text{react}}(t) = N_{\text{react}}(t_0) \exp(-k(t - t_0)) . \quad (2.7)$$

The rate associated with this exponential decrease is the *decay rate* k of reactant population close to the TS

$$k = -\frac{1}{N_{\text{react}}} \frac{d}{dt} N_{\text{react}}(t) = -\frac{d}{dt} \ln(N_{\text{react}}(t)) . \quad (2.8)$$

This decay rate is a sole property of the dynamics close to the NHIM of a barrier and, hence, is determined by the EOM and the specific shape of the saddle. As the decrease of the number of reactants in the close neighborhood of a static barrier is purely exponential, the change $\frac{d}{dt} N_{\text{react}}$ is proportional to the number of reactants via

$$\frac{d}{dt} N_{\text{react}}(t) = -k N_{\text{react}}(t) . \quad (2.9)$$

This result is also known in the framework of chemical kinetics [48, 62, 63], where the change of a reactant's population is also exponential for first order, unimolecular reactions.

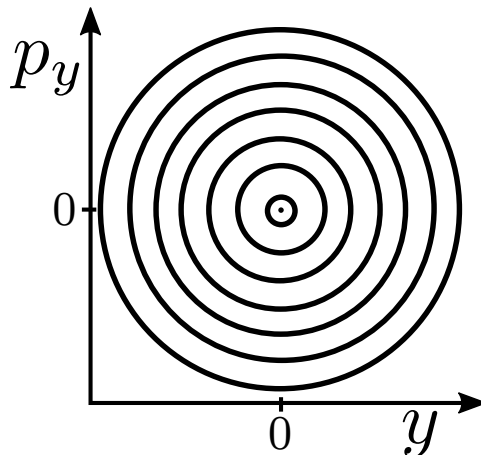


Figure 2.7.: Sketch showing the regular motion of periodic trajectories around an elliptic fixed point at $(y = 0, p_y = 0)$ on the NHIM of a static two-dimensional rank-1 barrier. This fixed point corresponds to the trajectory resting exactly at the saddle point, which is the maximum of the barrier in the unstable direction x and the minimum of the barrier in the stable direction y .

When switching to a static multidimensional rank-1 barrier with one unstable and $(n - 1)$ stable degrees of freedom, an infinite number of trajectories is bound to the saddle region for infinite time. These bound trajectories are located within the $(2n - 2)$ -dimensional NHIM of the rank-1 saddle, as explained in Sec. 2.1.3.

In the stable directions, i. e., the span of the NHIM in the orthogonal modes $(\mathbf{y}, \mathbf{p}_y)$, the dynamics is stable and initially closely located trajectories on the NHIM are usually not going to depart exponentially fast from each other as long as the associated dynamics is not chaotic. In the remaining two degrees of freedom of the full phase space, i. e. the reaction coordinate x and the conjugated reactive momentum p_x , the NHIM is unstable. Hence, the distance of any trajectory initialized with a (possibly arbitrary small) deviation in the unstable degree of freedom to one of the trapped trajectories on the NHIM increases approximately exponentially fast while both trajectories share the same dynamics in the orthogonal modes $(\mathbf{y}, \mathbf{p}_y)$, at least in a local vicinity of the NHIM. The restriction to “approximately exponentially fast” is necessary for systems in which the reaction coordinate x is coupled to the orthogonal modes \mathbf{y} . In that case, the decay rate $k(\mathbf{y}(t), \mathbf{p}_y(t))$ of a trajectory parametrized by the time t at a phase space position $(x, \mathbf{y}, p_x, \mathbf{p}_y)(t)$ in a close neighborhood of the TS depends on the corresponding position $(x^{\text{NHIM}}, p_x^{\text{NHIM}})(\mathbf{y}(t), \mathbf{p}_y(t))$ on the NHIM and is therefore referred to as *instantaneous rate*.

For static rank-1 barriers, the dynamics on the NHIM is regular and energy is strictly conserved. Hence, any trajectory initialized at position $(\mathbf{y}(t), \mathbf{p}_{\mathbf{y}}(t))$ on the NHIM is periodic and oscillates in direction of the orthogonal modes as, e. g., sketched in Fig. 2.7 for a two-dimensional rank-1 barrier. By averaging the instantaneous decay rates of reactant population in a close neighborhood of such a trajectory for a full period an associated *mean decay rate* of reactant population \bar{k} can be obtained.

In the special case where the reaction coordinate of a multidimensional system is uncoupled to the orthogonal modes, the decay rates of reactant population in a close neighborhood of the NHIM is purely exponential, just like in case of static one-dimensional barrier. Here, the instantaneous decay rates and the mean decay rates are the same. For general (and time-dependent) multidimensional systems, however, instantaneous decay rates need to be obtained and averaged over to obtain mean decay rates. The basic concepts therefore will be introduced in Chap. 4.

3

Driven systems

This section generalizes the theory from Chap. 2 to time-periodically driven barriers. After introducing a simple model for such a time-periodically driven barrier in Sec. 3.1 the basic changes arising from the external driving are stated in Sec. 3.2. Therefore, several methods to reveal the structure of the phase space close to the TS are discussed in Sec. 3.3 and an efficient method to find the NHIM in these systems is presented in Sec. 3.4. In Sec. 3.5 the dynamics of trajectories on the NHIM is briefly introduced. Essential parts of this Chapter have been published in Refs. [29, 53].

3.1 Model system for a two-dimensional reaction over a driven rank-1 barrier

To study the influence of a time-dependently driven barrier on the geometry of the phase space and the associated decay rates of reactant population close to the TS, a simple but general model is sought-for. It should describe classical particles of unit-mass, which move according to the Hamiltonian EOM in a potential with a rank-1 barrier. This barrier should feature an unstable degree of freedom, the reaction coordinate x , and it should be multidimensional and time-dependent. An example of being “multidimensional” is given by a two-dimensional barrier

$$V(x, y, t) = E_b \exp(-[x - \hat{x} \sin(\omega_x t)]^2) + \frac{\omega_y^2}{2} \left[y - \frac{2}{\pi} \arctan(2x) \right]^2, \quad (3.1)$$

where a single orthogonal mode y is coupled to the unstable direction x . In this *two-dimensional model system*, a Gaussian barrier with height E_b is time-periodically oscillating in direction of x with an amplitude \hat{x} and a frequency ω_x . In the stable direction of the barrier we assume the potential to be harmonic with angular frequency ω_y . To

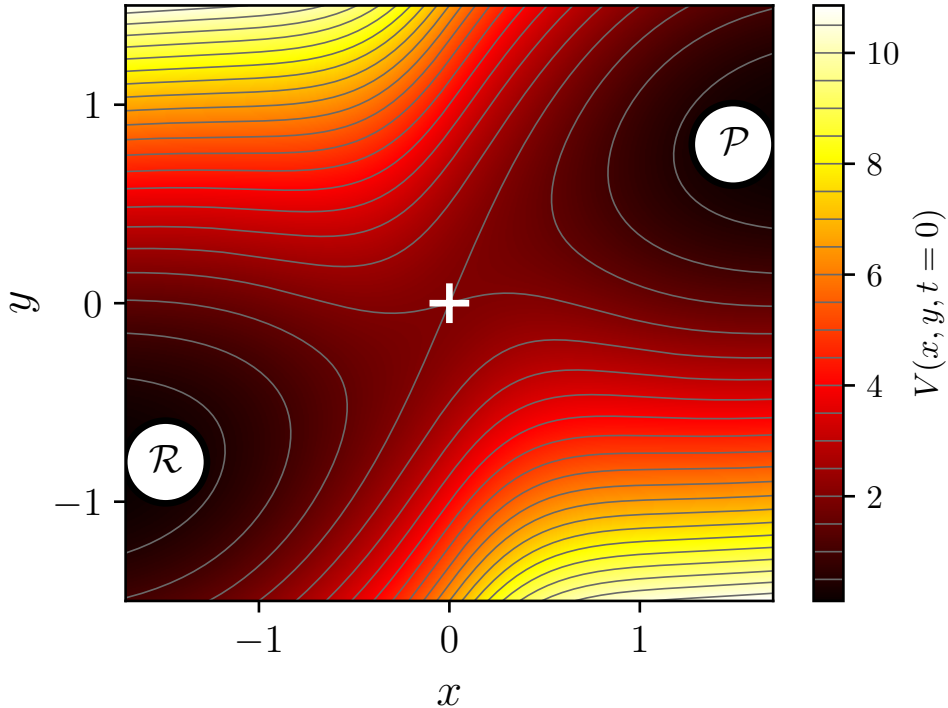


Figure 3.1.: The two-dimensional model system $V(x, y)$ according to Eq. (3.1) for the standard parameter set $E_b = 2$, $\hat{x} = 0.4$, $\omega_x = \pi$ and $\omega_y = 2$, visualized at time $t = 0$. The minimum on the left-hand side is called reactant \mathcal{R} and the minimum on the right-hand side is referred to as product \mathcal{P} . The saddle point is marked by a white cross.

prevent the system from separating into two one-dimensional systems the bath mode y is nonlinearly coupled to the reaction coordinate x via the arctan-function. Unless explicitly stated otherwise, we use a set of standard parameters in dimensionless units, where we set $E_b = 2$, $\hat{x} = 0.4$, $\omega_x = \pi$ and $\omega_y = 2$. Exemplary, a plot of the two-dimensional model system at time $t = 0$ is displayed in Fig. 3.1. Its minimum at $x < 0$ is called the reactant \mathcal{R} and the minimum at $x > 0$ is referred to as product \mathcal{P} . In between, there is the barrier having its saddle point marked by a white cross.

By setting $\omega_y = 0$, the potential becomes effectively one-dimensional and independent of y , which is repeatedly used in this work and referred to as the *one-dimensional model system*. Since the potential (3.1) has open reactant and product basins, we do not have to worry about global reflections at its outer boundaries, which would lead to global recrossings of the barrier. This is a simplification but not a constraint, since according to Sec. 2.1.2 the rise of global reflections can always be countered by introducing a proper saddle region in which the dynamics close to the barrier is locally recrossing-free. This fact has been comprehensively discussed in Ref. [55].

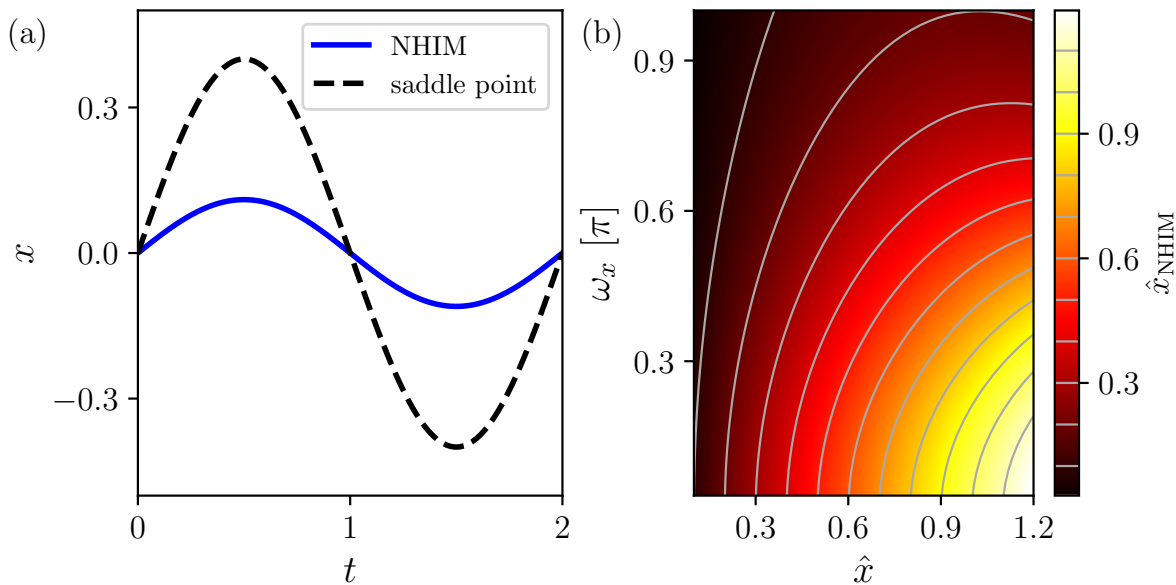


Figure 3.2.: (a): Black dashed line: instantaneous position of the saddle point of a time-periodically moving one-dimensional barrier according to Eq. (3.1) with $\hat{x} = 0.4$, $\omega_x = \pi$ and $\omega_y = 0$. Here, the instantaneous position of the NHIM, given as a blue solid line, moves in-phase with the barrier but with a considerably smaller amplitude. (b): Dependency of the amplitude \hat{x}_{NHIM} of the driven one-dimensional model system according to Eq. (3.1) with standard parameters on the amplitude \hat{x} and the frequency ω_x of the external driving.

3.2 Time-periodically driven barriers

When switching to a time-dependently driven system, a first, but very important change is that the associated Hamiltonian describing such a driven potential energy surface is explicitly dependent on time. Consequently, energy in such systems is not conserved. For a one-dimensional barrier, the associated NHIM still contains just a single trajectory, called the TS trajectory [44, 45], which “balances” on the moving barrier and never falls down to neither the reactant nor the product side. If time-periodically driven, the TS trajectory of such a barrier is a period-1 trajectory with respect to the period of the external driving. For the one-dimensional model system according to Eq. (3.1) with $\omega_y = 0$, the TS trajectory is displayed as a blue solid line in Fig. 3.2 (a) for standard parameters.

For multidimensional driven rank-1 saddles, there is an infinite number of trajectories balancing in the saddle-region on a moving barrier. Since all of them are bound to the

saddle region both forward and backward in time while moving on the NHIM in direction of the orthogonal modes, these trajectories are referred to as *bound trajectories*. The dimensionality of the NHIM of such a driven n -dimensional rank-1 barrier is still $(2n - 2)$ at a given time t , just like in the static case. When propagated in time, however, the NHIM changes its position and shape according to the EOM.

Whereas for non-driven systems the NHIM is attached to the saddle point of a rank-1 barrier, in driven systems the location of the NHIM in phase space completely detaches from the saddle point, as exemplary illustrated in Fig. 3.2 (a) for the one-dimensional driven model system. Here, the oscillation of the saddle point, given as a black dashed line, is considerably larger than the oscillation of the NHIM (blue solid line).

In general, the amplitude \hat{x}_{NHIM} of the NHIM's oscillation depends on the specific parameters of the external periodic driving. Exemplary for the one-dimensional model system, the dependency of \hat{x}_{NHIM} on the amplitude \hat{x} and the frequency ω_x of the one-dimensional model system according to Eq. (3.1) is displayed in Fig. 3.2 (b). Obviously, if the frequency ω_x of the external driving is very low, the amplitude \hat{x}_{NHIM} of the NHIM is approximately the same as the amplitude \hat{x} of the saddle point and, hence, the NHIM follows the maximum of the barrier quasi-statically. With increasing frequency, however, the amplitude of the NHIM's oscillation decreases non-trivially depending on the specific amplitude \hat{x} of the external driving. However, the amplitude \hat{x}_{NHIM} of the NHIM's oscillation can never be larger than the amplitude \hat{x} of the moving barrier. Otherwise, there would exist no repelling force of the potential on the bound trajectory back into the barrier region and such a trajectory would "fall off" to either the reactant or to the product side.

For multidimensional systems, a comparison between the amplitude of a moving barrier and the amplitude of the moving NHIM similar to Fig. 3.2 (b) is hard to do because the NHIM is an extended object in phase space. To still give the reader an idea of how such a multidimensional NHIM is moving in the barrier region of time-periodically driven systems, in Fig. 3.3 a three-dimensional representation $x_{\text{NHIM}}(y, v_y, t)$ of the NHIM in the two-dimensional model system according to Eq. (3.1) with an amplitude of $\hat{x} = 0.6$ and a frequency of $\omega_x = 0.5\pi$ is displayed at three different times $t = [0, T/4, T/2]$ from two different viewing angles (side view and top-down view).

The NHIM is displayed as a v_y color encoded, curved surface. As a comparison, the potential $V(x, y, t)$ is shown as gray-shaded contour surface having the instantaneous position of the saddle point marked as red dot. To illustrate the NHIM's movement, a coordinate-fixed dashed line is shown in the top-down view as a guide to the eye.

In Fig. 3.3 various effects of time-periodically driven systems can be seen. First of all, the movement of the NHIM is absolutely non-trivial and can be compared best to a flag moving in the wind. In its center, close to the saddle point, it is deformed much stronger than far away from that center. Further on, Fig. 3.3 nicely illustrates that the NHIM, being dependent on v_y , has to be constructed in phase space. If it would only depend on the position space coordinates x and y , it would be planar and not be visible in the top-down view. Last but not least, the movement of the NHIM relative to the

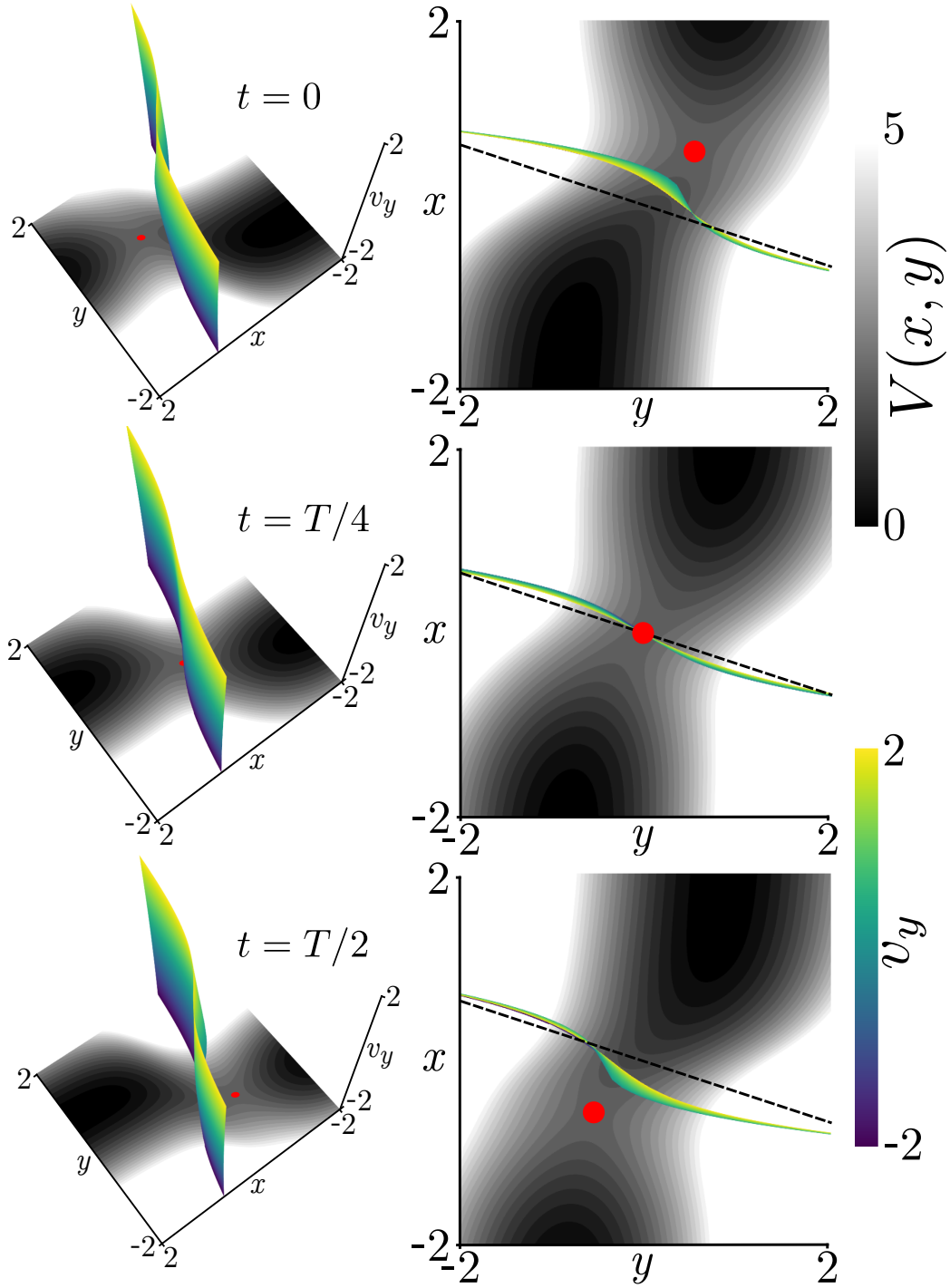


Figure 3.3.: Time-dependent representation $x_{\text{NHIM}}(y, v_y, t)$ of the moving NHIM of the two-dimensional model system according to Eq. (3.1) with $\hat{x} = 0.6$ and $\omega_x = 0.5\pi$. The NHIM is displayed as a v_y color encoded surface. The potential $V(x, y, t)$ is displayed as a gray-shaded contour surface with the saddle point marked as red dot. For further information, see text.

black dashed line in the top-down view is not of equal strength everywhere. Close to the saddle point, where the NHIM is deformed strongest, the amplitude of its movement is large. Far away from the saddle point, the movement of the NHIM is considerably smaller. In any case, however, the NHIM always moves less than the time-periodically driven barrier.

As explained in Sec. 2.1.1, a recrossing-free DS can be attached to the NHIM. For time-dependent systems the position of the NHIM in the phase space is time-dependent and, consequently, the attached DS moves with the same frequency as the NHIM. Other than that, statements given in Sec. 2.1 regarding to the DS are also valid if a barrier is time-dependently driven. In closed systems, however, the movement of a saddle has to be taken into account when choosing a proper barrier region.

3.3 | Revealing phase space structures

In the context of TST, a reaction happens exactly when a reactive trajectory pierces the DS attached to the NHIM of a barrier. The existence, dimensionality and meaning of these potentially multidimensional objects located in phase space are discussed in Chap. 2 for static rank-1 barriers. In Sec. 3.2, changes introduced by a time-periodically driven barrier are elaborated. In this section, several methods are introduced to numerically resolve not only the NHIM and the attached stable and unstable manifolds, but also the different reactive and non-reactive areas of the phase space.

3.3.1 Lagrangian descriptor

A tool to examine the phase space structures of time-dependent dynamical systems is the Lagrangian descriptor (LD) [64]. It was introduced in 2013 by Mancho et al. and applied successfully to reactions in the context of TST in many different cases [29, 55, 64–67]. For a given position \mathbf{x}_0 , velocity \mathbf{v}_0 and time t_0 the LD is defined as

$$\mathcal{L}(\mathbf{x}_0, \mathbf{v}_0, t_0) = \int_{t_0-\tau}^{t_0+\tau} \|\mathbf{v}(t)\| dt. \quad (3.2)$$

It measures the arc length of a trajectory $\mathbf{x}(t)$ which is initialized at a position $(\mathbf{x}_0, \mathbf{v}_0)$ at time t_0 in the phase space and propagated according to the EOM of a system both forward and backward in time over the interval $[t_0 - \tau; t_0 + \tau]$. Here, the parameter τ has to be chosen such that the relevant timescale of the system is covered.

The LD of a trajectory initialized in the barrier region of a rank-1 saddle is large if this trajectory “falls down” the barrier to either the reactant or the product basin and therefore gains a lot of kinetic energy. However, if initialized on or very close to the stable or unstable manifolds, it will approach the NHIM asymptotically fast in either the forward or in the backward direction of time. Since such a trajectory is not going

to fall down the barrier, its kinetic energy will remain relatively small and, therefore, its arc-length is short. Consequently, the stable and the unstable manifolds are revealed by having a local minimum in \mathcal{L} . To distinguish between the stable and the unstable manifolds the integral in Eq. (3.2) can be split into a part solely forward in time and one solely backward in time. The stable manifold is then defined by the minimum of the forward LD and the unstable manifold by the minimum of the backward LD.

Exemplary, the LD of the one-dimensional model system according to Eq. (3.1) with $\omega_y = 0$ at time $t = 0$ is displayed in Fig. 3.4 (a). The stable \mathcal{W}_s and the unstable \mathcal{W}_u manifolds appear as minimal, ditch-like structures and are located as expected according to Fig. 2.1 (b). At their intersection, the NHIM is marked by a black cross. Additionally, the full TS trajectory is displayed as a blue dashed line. When looking at the LD in Fig. 3.4 (a), a disadvantage of its definition according to Eq. (3.2) is evident. Other than the cross-like ditches of the stable and unstable manifolds, additional minima of the LD are visible in the phase space. As a result, numerically looking for a minimum of the LD to find one of the two manifolds will be very difficult as a minimization routine could get stuck in one of these additional minima. In closed systems, the LD as defined in Eq. (3.2) still contains the ditches of the stable and the unstable manifolds. However, these ditches become obfuscated by a fractal-like structure in the LD originating from the global recrossings due to the reflections at the outer boundaries of the potential. A detailed discussion on these fractal-like structures and their causes can be found in Ref. [55].

3.3.2 Modifications of the Lagrangian descriptor

As already discussed in Sec. 2.1.2, the problem of global recrossings can be solved by introducing a suitable barrier region $x \in [x_{\mathcal{R}}, x_{\mathcal{P}}]$ for the reaction coordinate x . If properly chosen, such a barrier region does not only solve the problem of arising fractal-like structures in the LD for closed systems, it also removes the occurring additional minima in the LD other than the main ditches of the stable and the unstable manifolds. Therefore, the LD is computed not for a fixed time τ but rather until the underlying trajectory leaves the barrier region. Hence, this modified LD is defined as

$$\tilde{\mathcal{L}}(\mathbf{x}_0, \mathbf{v}_0, t_0) = \int_{t_b(\mathbf{x}_0, \mathbf{v}_0, t_0)}^{t_f(\mathbf{x}_0, \mathbf{v}_0, t_0)} \|\mathbf{v}(t)\| dt \quad (3.3)$$

with $x(t_{b,f}(\mathbf{x}_0, \mathbf{v}_0, t_0)) = x_{\mathcal{R}}$ or $x_{\mathcal{P}}$ for $t_b < t_0 < t_f$.

Here, t_b and t_f are the times at which the corresponding trajectory, initialized at $(\mathbf{x}_0, \mathbf{v}_0, t_0)$, leaves the barrier region backward or forward in time, respectively. In Fig. 3.4 (b), the modified LD is displayed for the same case as in Fig. 3.4 (a). When comparing both figures, the filtering mechanism of the modified LD is evident. Additional substructures visible in the standard LD according to Fig. (3.4) (a) vanish in the modified LD according to Fig. 3.4 (b). As a major change, however, the stable and the

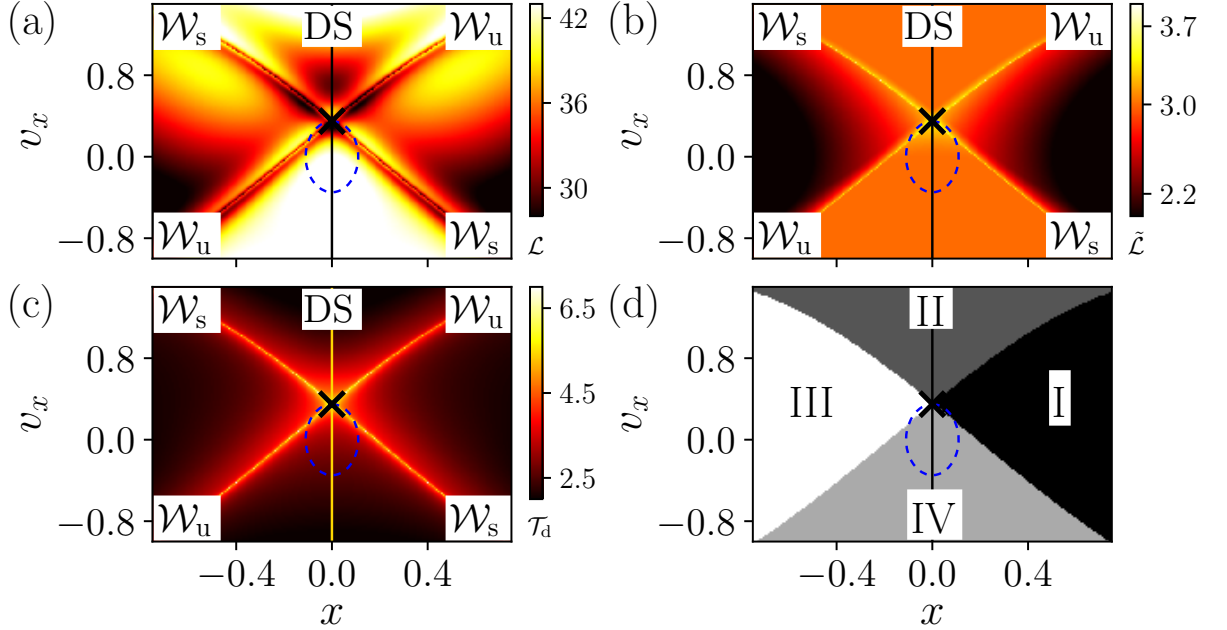


Figure 3.4.: Phase-space of the one-dimensional model system according to Eq. (3.1) with $\omega_y = 0$ at time $t = 0$. Several methods are visualized to reveal the stable (\mathcal{W}_s) and unstable (\mathcal{W}_u) manifolds of the NHIM, which is given by their intersection and marked by a black cross. The vertical solid line shows the attached instantaneous DS. The blue dashed line shows the TS trajectory. The contours in the panels correspond to (a) \mathcal{L} as defined in Eq. (3.2) with $\tau = 10$, (b) $\tilde{\mathcal{L}}$ according to Eq. (3.3), (c) the time-descriptor \mathcal{T}_d (see Eq. (3.4)), and (d) reactive and non-reactive regions according to Table 3.1. Therefore, the barrier region was set to $x \in [-1.5, 1.5]$. Already published in Ref. [29].

unstable manifolds appear as maximum structures of the modified LD. The reason is that trajectories initialized closer to the manifolds stay in the saddle region for a longer time. Since the propagation of a trajectory is only stopped when it leaves the barrier region, the modified LD increases for such trajectories. Mathematically, if initialized directly at the manifolds or the NHIM, this propagation time will be infinite and, hence, the modified LD will diverge. However, due to the unstable properties of the NHIM, such an infinite trapping will usually not occur in a numerical simulation.

Based on these observations, the modified LD can be simplified again by just tracking the time a reactive trajectory, initialized at $(\mathbf{x}_0, \mathbf{v}_0, t_0)$, stays in the barrier region.

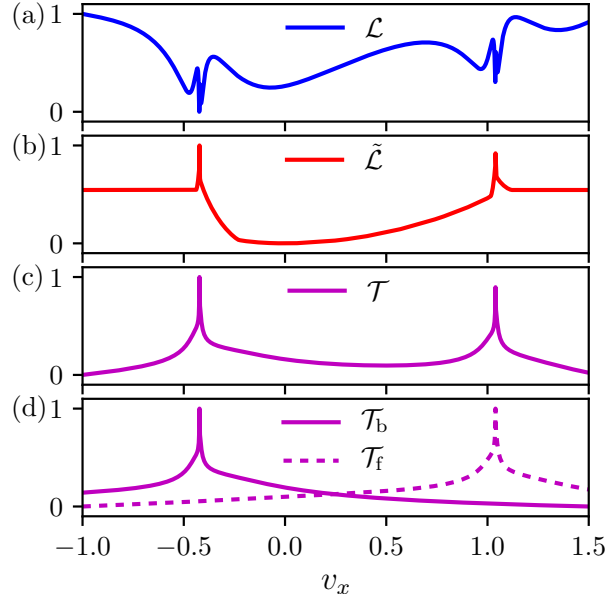


Figure 3.5.: One-dimensional cut through Fig. 3.4 at $x = -0.4$. The LD defined in Eq. (3.2) is displayed in part (a), the modified LD according to Eq. (3.3) by including an appropriate barrier region in part (b) and the TD according to Eq. (3.4) in part (c). Part (d) shows the individual parts of the TD for propagation solely in backward respectively forward time. All curves have been normalized. Already published in Ref. [29].

Following the nomenclature of the LD this time is referred to as TD

$$\begin{aligned}
 \mathcal{T}(\mathbf{x}_0, \mathbf{v}_0, t_0) &\equiv t_f(\mathbf{x}_0, \mathbf{v}_0, t_0) - t_b(\mathbf{x}_0, \mathbf{v}_0, t_0) , \\
 \mathcal{T}_f(\mathbf{x}_0, \mathbf{v}_0, t_0) &\equiv t_f(\mathbf{x}_0, \mathbf{v}_0, t_0) - t_0 , \\
 \mathcal{T}_b(\mathbf{x}_0, \mathbf{v}_0, t_0) &\equiv t_0 - t_b(\mathbf{x}_0, \mathbf{v}_0, t_0) .
 \end{aligned} \tag{3.4}$$

Since the time a trajectory stays in the barrier region increases the closer it is initialized to either \mathcal{W}_s or \mathcal{W}_u , these two manifolds are revealed by a maximum of the TD as exemplarily displayed in Fig. 3.4 (c) for the same trajectory as in Fig. 3.4 (a). Again, a theoretical divergence of the TD for trajectories initialized exactly on the manifolds is numerically very unlikely. When compared to the LD in Fig. 3.4 (a) and the modified LD in Fig. 3.4 (b), the TD according to Fig. 3.4 (c) shows the cross-like structure of the two manifolds with a very high contrast and no additionally obfuscating structures. On top of that, the TD again offers the possibility to resolve just the stable or just the unstable manifold by propagating trajectories solely forward (\mathcal{T}_f) or backward in time (\mathcal{T}_b). To set up a numerical routine to find the stable and the unstable manifolds in the phase space, an optimization based on the TD is the method of choice. Since the propagation of trajectories in forward and backward time can be done separately,

Table 3.1.: Nomenclature of the different reactive (II, IV) and non-reactive (I, III) areas in phase space separated by the two manifolds. Trajectories are leaving the neighborhood of the barrier at the reaction coordinate $x_{\text{exit}}^{\text{b,f}}$ when propagated in backward (b) and forward (f) time, respectively.

Area	$x_{\text{exit}}^{\text{b}}$	$x_{\text{exit}}^{\text{f}}$
I	$x_{\mathcal{P}}$	$x_{\mathcal{P}}$
II	$x_{\mathcal{R}}$	$x_{\mathcal{P}}$
III	$x_{\mathcal{R}}$	$x_{\mathcal{R}}$
IV	$x_{\mathcal{P}}$	$x_{\mathcal{R}}$

numerical ambiguities between the stable and unstable manifolds near their intersection can be avoided.

To further clarify the process when modifying the LD or even switching to the TD, a one-dimensional cut through the several parts of Fig. 3.4 at $x = 0.4$ is displayed in Fig. 3.5. Here, the two manifolds are located at the deepest minima of the LD, but several other minima are also visible. However, the modified LD in Fig. 3.5 (b) shows clearly visible maxima at the positions of the manifolds and other maxima are not present. Hence, removing any obfuscating structures is basically done by introducing an appropriate barrier region. Switching to the TD in Fig. 3.5 (c) just increases the contrast when compared to the modified LD. In Fig. 3.5 (d), the forward and the backward parts of the TD are displayed individually to show how they form the total TD when combined.

These approaches to resolve the stable and the unstable manifolds in the phase space can be simplified even more. Therefore, the phase space is separated into four different areas based on from which side of the barrier trajectories come from in their past and to which side they go to in the future. A trajectory, initialized at the phase space position $(\mathbf{x}_0, \mathbf{v}_0, t_0)$ is propagated forward (f) and backward in time (b) until it leaves the barrier region $x \in [x_{\mathcal{R}}, x_{\mathcal{P}}]$ with respect to its reaction coordinate x . The initial point is then assigned to one of the four areas explained in Table 3.1. Based on the so-assigned reactive and non-reactive areas, a fourth method to resolve phase space structures is given in Fig. 3.4 (d) with different shades of gray. Using this separation into reactive and non-reactive areas the manifolds are clearly revealed at their boundaries and there are no obfuscating structures present.

In any case, the specific choice of a suitable barrier region $x \in [x_{\mathcal{R}}, x_{\mathcal{P}}]$ always depends on the system and the dynamics introduced by the external driving of a barrier. Usually, if the barrier region is chosen too large, arising fractal-like structures will obfuscate the predominant cross of the manifolds or will lead to a mixing of the separate reactive and non-reactive areas. On the other hand, if the barrier region is chosen too small, trajectories are not propagated long enough to capture the relevant dynamics of a system and the structure of the manifolds in the phase space is not clearly resolved.

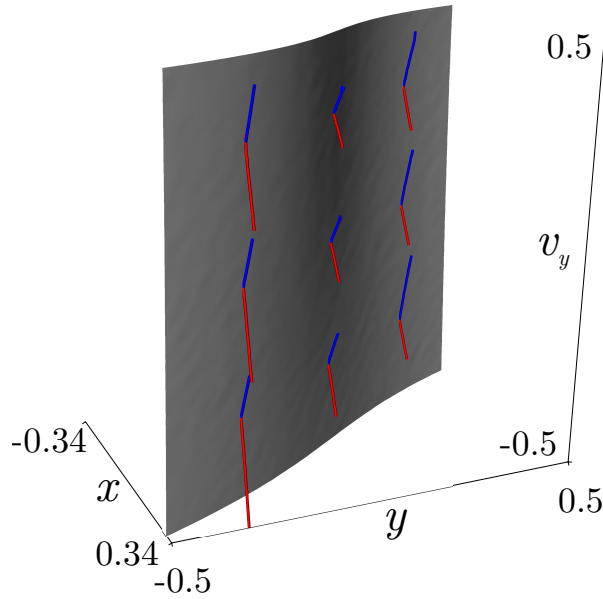


Figure 3.6.: Gray surface: $x^{\text{NHIM}}(y, v_y)$ for the potential (3.1) at $t = 0.5$. For (x, v_y) -slices at 3×3 different values (y, v_x) the one-dimensional fibers of the stable manifold in each slice are given in red lines, the fibers of the unstable manifold in blue lines. Their intersections are located on the two-dimensional NHIM. Already published in Ref. [29].

3.3.3 Generalization to multidimensional rank-1 barriers

Although the examples displayed in Figs. 3.4 and 3.5 are given for a one-dimensional model system, the generalization to systems with multidimensional rank-1 saddles is straightforward. Having found a suitable coordinate system with an appropriate reaction coordinate x and orthogonal modes \mathbf{y} , any of the methods introduced here is able to resolve the fibers of the stable and unstable manifolds in an (x, v_x) cross section of the full phase space for fixed orthogonal modes $(\mathbf{y}, \mathbf{v}_y)$ at a given time t . The result will look similar to Fig. 3.4, but will depend on the specific choice of the orthogonal modes (and of course on time). The full multidimensional stable and unstable manifold can be revealed pointwise by successively repeating these calculations for different sets of orthogonal modes. The in general also multidimensional intersection of the stable and unstable manifolds is the NHIM, as explained in the sketch in Fig. 2.4 or in Sec. 2.1.3. Exemplary, a similar figure is obtained for the two-dimensional model system according to Eq. (3.1) and displayed in Fig. 3.6 at time $t = 0.5$. Therefore, the one-dimensional fibers of the stable and unstable manifolds are obtained by numerically looking for the two maxima of the TD in an (x, v_x) -slice of the full phase space. For 3×3 different values (y, v_x) , these fibers are displayed together with the two-dimensional NHIM which is shown as a gray surface $x^{\text{NHIM}}(y, v_y)$.

3.4 Finding the NHIM

Finding the NHIM can be done numerically using the methods explained in Sec. 3.3.1. For a given initial reaction coordinate x_0 , the corresponding velocities v_x of the stable and the unstable manifolds can be obtained using a standard iterative routine to find the maxima of, e. g., the modified LD or the TD according to Fig. 3.5. The NHIM is located at the intersection of the stable and the unstable manifold. At the corresponding position x^{NHIM} , the v_x distance between these manifolds is zero. Consequently, x^{NHIM} can be found iteratively using a root search for the distance of the stable and the unstable manifold at various positions x_i . This procedure, however, is numerically very expensive since it nests the iterative routine to find the maxima of, e. g., the modified LD or the TD into the root search of the v_x -difference between the two manifolds. The fact that obtaining any of the many LD or TD values requires the propagation of a full trajectory makes the situation even worse. Still, the method of finding the NHIM using nested iterations has been successfully applied in Ref. [68] to a three-dimensional extension of the model system similar to Eq. (3.1) and further information can be found in this reference. In this thesis, however, I will present a different approach to numerically obtain the position of the NHIM in the phase space, the *binary contraction method* (BCM) which is, according to Sec. 3.4.1, much faster and more elegant than just using nested iterations.

3.4.1 Binary contraction method

By introducing a barrier region $x \in [x_{\mathcal{R}}, x_{\mathcal{P}}]$ for an appropriately chosen reaction coordinate x , various trajectories can be classified according to Table 3.1 to different reactive areas. Thereby, the basic idea is to determine at which side a trajectory entered the barrier region in the past and to which side it leaves the barrier region when propagated forward in time. The classification of reactive and non-reactive trajectories offers an alternative way to find the NHIM, the *binary contraction method* (BCM), which avoids the nested iterations needed to find the stable and the unstable manifolds. The binary contraction method (BCM) is explained best by means of Fig. 3.7. It starts with a quadrangle in an (x, v_x) section of the phase space. Each vertex of the quadrangle has to be located in a different reactive or non-reactive area which are separated by the stable and the unstable manifold. This initialization is non-trivial since the specific location of the manifolds is a priori unknown. In Fig. 3.7, these manifolds are just sketched for a better understanding. An initial quadrangle fulfilling this requirement can be either obtained by choosing it large enough or making an educated guess¹.

¹To gain a priori knowledge on the structure of the phase space in the barrier region obtaining a figure like Fig. 3.4 based on the LD or the TD might help. Alternatively, Ref. [68] gives numeric approaches on how to correctly initialize the BCM.

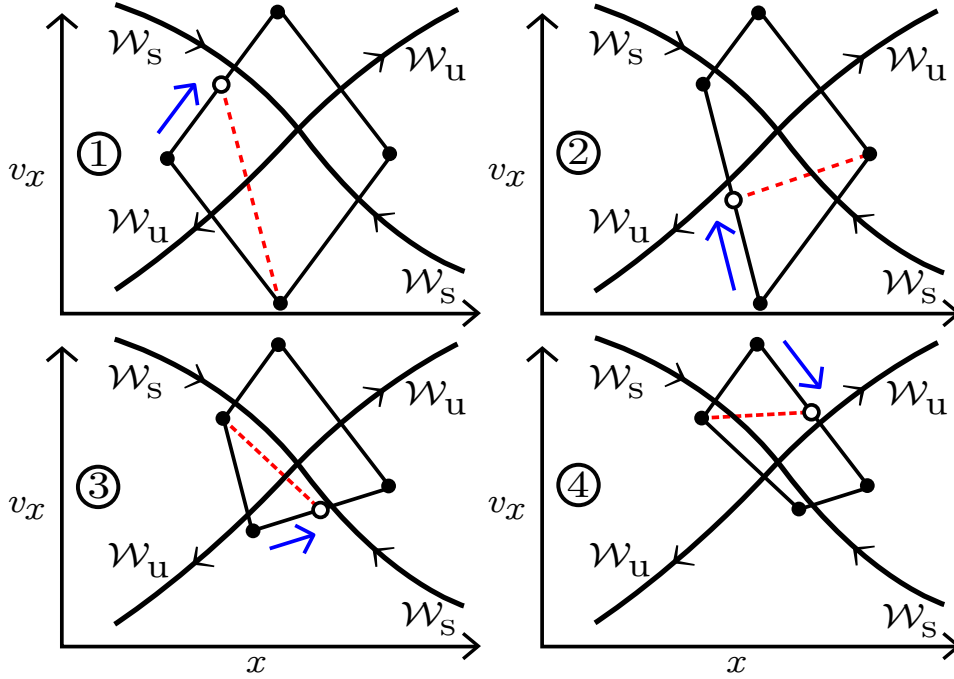


Figure 3.7.: Illustration of the BCM. This iterative method starts with a quadrangle having its four vertices in each of the four different areas of the phase space, which are separated by the stable \mathcal{W}_s and the unstable \mathcal{W}_u manifold. Successively shrinking the quadrangle yields the intersection of the manifolds. For further information, see text. Already published in Ref. [29].

To begin the BCM, four trajectories, initialized at each vertex of the quadrangle, have to be propagated both forward in and backward in time until they leave the barrier region. This procedure allows to assign each trajectory to one of the reactive and non-reactive areas in Table 3.1 and therefore is a self-consistency check if the BCM is initialized correctly. During the following iterations of the BCM a candidate vertex is successively chosen at the middle of each side of the quadrangle. At each candidate vertex, another trajectory is propagated both forward and backward in time and classified to one of the reactive areas in Table 3.1. Now, the to that area corresponding vertex of the current quadrangle is replaced by the candidate vertex. This procedure gradually shrinks the area of the quadrangle, as exemplary visualized in Fig. 3.7 for the first four iterative steps. Finally, its center converges to the intersection of the manifolds yielding x^{NHIM} and v_x^{NHIM} . Depending on the desired accuracy, the BCM can, e. g., be stopped if the relative error of this center point is small enough. For multidimensional systems the position $(x^{\text{NHIM}}, v_x^{\text{NHIM}})(\mathbf{y}, \mathbf{v}_y, t)$ of the NHIM for given orthogonal modes $(\mathbf{y}, \mathbf{v}_y)$ at a time t may be found pointwise using the BCM. Here, for any point sought on the NHIM, a new quadrangle has to be initialized in an appropriate section of the full phase space.

Since for any iteration of the BCM only a single trajectory has to be propagated and classified according to Table 3.1 the BCM is much faster when compared to the nested iteration method based on finding the stable and the unstable manifolds directly. An in detail comparison can be found in Ref. [68], which also introduces a fallback method to deal with the sometimes arising situation in which the stable and the unstable manifolds are so strongly deformed that their intersection is located outside a valid quadrangle. Using this fallback method, the full quadrangle can “walk” along the manifolds to find their intersection and ensure convergence even in a strongly nonlinear regime of the dynamics close to the NHIM.

3.4.2 Interpolating the NHIM using machine learning techniques

Using the BCM according to Sec. 3.4.1 the position $(x^{\text{NHIM}}, v_x^{\text{NHIM}})(\mathbf{y}, \mathbf{v}_y, t)$ of the NHIM can be obtained point-wise for given orthogonal modes $(\mathbf{y}, \mathbf{v}_y)$ and time t . According to the discussion in Sec. 2.1.3, to each point on the NHIM a vertical recrossing-free DS can be attached. In doing so, the DS (i.e., a co-dimension one hypersurface) is also just resolved at the individual points of the NHIM, as schematically sketched in Fig. 3.8 with blue dots. When performing rate calculations in the context of TST a possible approach is to propagate large ensembles of reactive trajectories. An individual trajectory reacts exactly when it pierces the recrossing-free DS attached to the NHIM and, hence, the precise time this piercing happens for any trajectory of the ensemble has to be individually obtained. The crux is that such a trajectory, as schematically sketched in Fig. 3.8, may pierce the DS on its way from reactant \mathcal{R} to product \mathcal{P} at a previously unknown time t_{crossing} and corresponding position $\mathbf{y}(t_{\text{crossing}})$ and velocity $\mathbf{v}_y(t_{\text{crossing}})$ of the orthogonal modes and usually not at some pre-calculated values of the DS which are symbolized by blue dots. Furthermore, to even detect such a piercing the instantaneous position on a reactive trajectory must be compared to the corresponding position of the DS from the time it enters the barrier region on, e.g., the reactant side until it leaves the barrier region to the product side, respectively. Here, computing the required position of the DS from scratch whenever it is needed would be numerically prohibitively expensive since even obtaining the DS at a single position using the efficient BCM requires the propagation of several dozens of trajectories. However, having a continuous and fast-to-obtain representation $(x^{\text{NHIM}}, v_x^{\text{NHIM}})(\mathbf{y}, \mathbf{v}_y, t)$ of the NHIM and, therefore, of the DS attached, would considerably reduce this numerical effort – provided that only a comparatively small number of pre-calculated points is needed to obtain it.

Nowadays, these requirements are fulfilled by machine learning methods which have, e.g., been applied within the field of theoretical chemistry for the interpolation of high-dimensional potential energy surfaces [69–79]. In our TST-group at the ITP1 we have successfully applied these machine learning methods in the context of TST. More specifically, in Refs. [29, 54] we have used artificial neural network (NN) to continuously interpolate the NHIM in driven multidimensional systems. Here, I will give a brief and

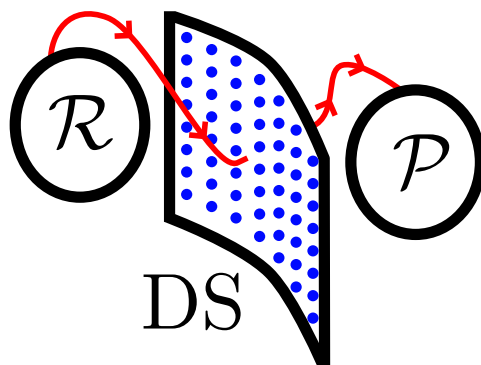


Figure 3.8.: Sketch of the phase space of a chemical reaction. A reactive trajectory (red) on its pathway from reactant \mathcal{R} to product \mathcal{P} crosses the DS which is a co-dimension one manifold. Here, the problem that a reactive trajectory pierces the DS not at the pre-calculated points (blue bullets) but somewhere in between is illustrated.

basic overview on how to set up and use these NNs and what advantages and disadvantages they imply. The interested reader, however, is referred to these references or the references therein.

To approximate functions of arbitrary complexity in any dimension a NN is a powerful tool [80]. Inspired by our current understanding of a human brain, where signals are processed and passed along between a large amount of neurons, an artificial NN consists of several neurons being connected in a very complex way. According to the sketch in Fig. 3.9 (a), such a NN is organized in different layers containing a various number of neurons (black circles). In the special type of artificial NN we are using, the *feed-forward* NN, each neuron of a given layer (the columns in Fig. 3.9 (a)) is connected to the output of any neuron of the previous layer. The first layer, called the *input layer*, just takes the input values and passes them on to the next layer. To represent the time-dependent NHIM of an n -dimensional rank-1 barrier this input layer consists of $(n - 1)$ neurons for the position \mathbf{y} of the orthogonal modes, $(n - 1)$ neurons for their velocities \mathbf{v}_y and an additional neuron for the time t . Now, a number of *hidden layers* with various amounts of neurons process the given information towards the output layer. In our case, the output layer consists of two neurons for the reaction coordinate x and the respective velocity v_x . Hence, such an artificial NN is set up to yield the representation $(x^{\text{NHIM}}, v_x^{\text{NHIM}})(\mathbf{y}, \mathbf{v}_y, t)$ of the time-dependent NHIM. The specific size and structure of such a network is highly dependent on the problem and has to be optimized during the training process.

The neurons of the hidden layers are able to transform a given input into a desired output. Similar to a human brain, a NN is able to learn the output for a specific input by finding patterns and dependencies in some *training data* provided to the network. This training data therefore has to provide the correct result for several input values of the network. Here, we use individual points $(x^{\text{NHIM}}, v_x^{\text{NHIM}})$ of the NHIM obtained

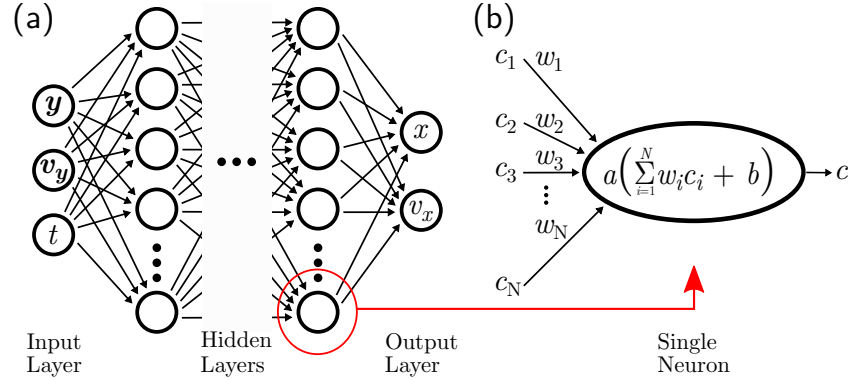


Figure 3.9.: (a): Sketch of a NN designed to continuously approximate $(x^{\text{NHIM}}, v_x^{\text{NHIM}})(\mathbf{y}, \mathbf{v}_y, t)$ for the time-dependent NHIM of an n -dimensional rank-1 barrier. Such a network consists of a number of hidden layers, each containing various neurons. Here, the input to the first layer, given by the $(n - 1)$ orthogonal modes \mathbf{y} , the associated velocities \mathbf{v}_y and time t is processed from layer to layer towards the output layer. Each neuron is connected to all neurons of a previous layer – a *feed-forward* neural network. (b): Sketch of a single neuron. Its output c is obtained by summing up the weighted outputs c_i of the neurons of a previous layer with respective weights w_i , adding up a bias b and passing the results into an activation function $a(x)$. In the process of *training*, the free parameters w_i and b of the hidden neurons are properly adjusted. Already published in Ref. [29].

using the BCM at various positions $(\mathbf{y}, \mathbf{v}_y)$ of the orthogonal modes and at various times t . By *learning* a set of free parameters of the network is adjusted. These parameters are incorporated into the artificial neurons. A sketch of a single neuron is given in Fig. 3.9 (b). It adds up the weighted inputs c_i of all neurons of the previous layer with separate weights w_i , respectively. To this sum, a *bias* b is added and the result is used as input for an *activation function* $a(x)$ to yield the output c of the neuron

$$c = a\left(\sum_{i=1}^N w_i c_i + b\right). \quad (3.5)$$

Here, we use $a(x) = \tanh(x)$ as activation function taking advantage of the fact that this function is smooth, nonlinear and bound for $x \rightarrow \pm\infty$. The nonlinearity ensures, that a NN is not simply a linear transformation of a given input and provides the necessary complexity to represent and interpolate the training data. However, the choice of an activation function is always dependent on the specific problem and other choices, e. g., the sigmoid function are also common.

Before training, the weights and biases of all neurons of the hidden layers are initialized randomly in a reasonable range of parameters. While training an artificial NN its current

output for a given input of the training data is compared to the known result of the training data. A typical procedure is to average the mean square difference of these known values and the current output of the net over all training points, denoted as the *cost function* which measures the quality of the NN. Lowering the cost-function will increase the networks capacity of reproducing correct output values. Therefore, the weights and biases are optimized iteratively using a gradient-based method, the *back-propagation* algorithm [54, 81]. To test if a trained network really is able to correctly interpolate between known points it is usually not trained on the full set of training data. Instead, the training data is split into two parts, the *training set* and the *verification set*. The network is only trained on the training set. The output of the network, however, is also checked against the verification set. Therefore, cost functions are defined individually for the two parts of the training data, the *training cost* and the *verification cost*. Only if both the training cost and the verification cost are low, a network is properly trained and is therefore able to interpolate correctly in between some given training data.

A well-trained artificial NN is able to continuously represent $(x^{\text{NHIM}}, v_x^{\text{NHIM}})(\mathbf{y}, \mathbf{v}_y, t)$ of the time-dependent NHIM, as has been shown in Ref. [29] for the two-dimensional model system according to Eq. (3.1) and in Ref. [54] for a three-dimensional extension of the model system. According to these references, training a NN needs an appropriate amount of computational time and also the time needed to generate the training data with the BCM needs to be taken into account here. Having properly trained a NN its evaluation time to obtain the position of the NHIM at any position in between the pre-calculated points is usually insignificant when compared to obtaining it by means of the BCM. Consequently, using a continuous representation of the NHIM and the DS attached with an artificial NN is only favorable if the same NHIM is evaluated at so many different positions that the saved time by not having to use the BCM exceeds the training time. This might be the case if a large ensemble of reactive trajectories is propagated to yield the reactive flux over a time-dependently driven barrier. In Sec. 4, three different methods are introduced to obtain instantaneous and phase-space resolved decay rates of the TS and, therefore, the reactive flux at least in a local neighborhood of the NHIM. Here, only the *ensemble method* according to Sec. 4.2 utilizes the propagation of reactive ensembles with several trajectories. However, even this method is designed in a way that only a rather small amount of trajectories has to be propagated and, therefore, it just directly uses the BCM.

In future applications as, e. g., the generalization of the decay rates to thermal systems or when obtaining reaction rates for ensembles which pierce the DS outside the local neighborhood of the NHIM these facts may change and methods may require the propagation of a large number of trajectories. Here, an artificial NN will provide a useful tool to numerically access regimes which would be inaccessible with respect to computational time when only using the BCM. For a more detailed discussion on possible further research, see Chap. 6.

A completely different aspect when representing the NHIM by means of machine learning techniques is the obtainable precision of these methods. The BCM allows to obtain individual points of the NHIM with a very high precision up to a relative error of 10^{-12} according to Ref. [68]. Although these high-precision points are used as training data of an artificial NN such a network usually is able to reproduce the NHIM at only a relative error of about 10^{-4} according to Ref. [54]. Consequently, the use of NN is only advisable, if high precision is not important. An exemplary application would be to classify a large number of trajectories into reactive and non-reactive trajectories and the specific point where the reaction happens is not sought for in high-precision. The methods presented in Chap. 4, however, follow a different approach. Here, very few but high precision points, obtained by the BCM, are used to obtain conclusive results for the decay rates of the TS.

3.5 Dynamics on the NHIM

The dynamics of trajectories on the time-dependent NHIM of a driven system provides substantial information both on the stability of the TS as well as on the decay rates of trajectories in a close neighborhood. According to Sec. 2.2.2, to any trajectory on the NHIM a unique mean stability can be assigned. Modifying the parameters, e. g., the amplitude or the frequency of the external driving has not only a huge influence on the dynamics on the NHIM, but also alters the stability of the TS. The methods to calculate the associated decay rates are introduced in Chap. 4 and further examined in Chap. 5 for the driven $\text{LiCN} \rightleftharpoons \text{LiNC}$ isomerization reaction. Here, the underlying methods needed to access the dynamics of trajectories on the NHIM is discussed.

The NHIM in a (driven) system is an invariant subspace of the full phase space. Trajectories inside it are mathematically trapped forever and, hence, will never “fall down” to either the reactant or to the product side. To access the dynamics of trajectories on the NHIM, however, is a difficult task because such a trapping will never be fully observed in a numerical simulation. The reason therefore is, that according to Sec. 2.1.1 any stretching and contraction rates on the NHIM are smaller than any of these rates away from the NHIM. Hence, the NHIM is unstable and any (possibly infinitesimally small) deviation from it grows exponentially fast in time in its local vicinity. This is automatically also true for the error any numerical integrator adds up when propagating a trajectory – even if this integrator is as precise as numerical double precision. As a consequence, any numerically obtained trajectory initialized in the NHIM usually leaves this unstable subspace when propagated for a long time and becomes either a reactant or a product. Exemplary, this departure of trajectories from the NHIM is visualized in Fig. 3.10 for a periodic trajectory on the NHIM of the two-dimensional model system according to Eq. (3.1). Depending on the strength of the external driving, the departure of trajectories is faster and slower and, hence, the trajectory is more or less stable.

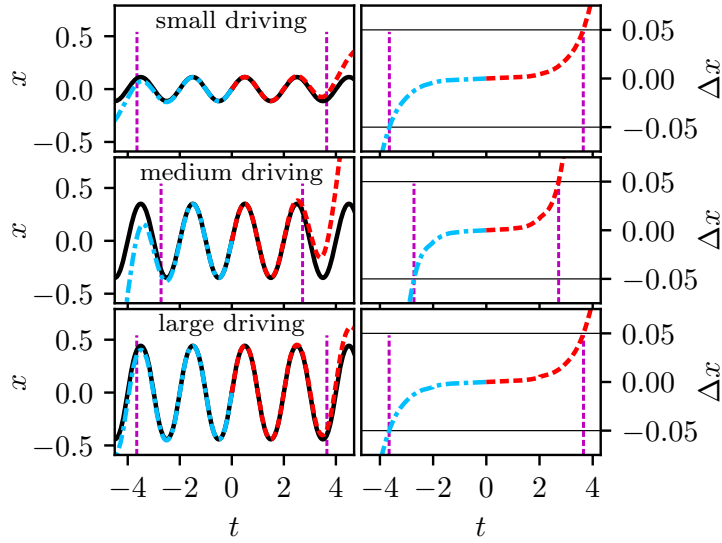


Figure 3.10.: Left column: The black solid line shows a periodic trajectory of the two-dimensional model system according to Eq. (3.1). This trajectory corresponds to the stable fixed point in Fig. 3.11. A second trajectory with an offset of $\Delta v_x = 10^{-3}$ at $t = 0$ is shown as a red/blue dashed line. Depending on the strength of the external driving (small: $\hat{x} = 0.1$, medium: $\hat{x} = 0.6$, large: $\hat{x} = 1.6$) it leaves the periodic trajectory faster or slower (the frequency of the driving is $\omega_x = \pi$ in any case). The associated stability indicated by the deviation in the reactive coordinate x is visualized in the right column. Here, the stability is minimal for medium driving.

Here, the possibility to control the stability of trajectories on the NHIM by modifying a parameter of the external driving is directly visible.

The drawback that trajectories on the NHIM are unstable can be turned into an advantage since, conversely, the error made with respect to the unstable degree of freedom of the NHIM when numerically propagating trajectories is just exponentially small for short integration times. Hence, when correcting this exponentially small deviation from the actual position of the NHIM just after a short time, the error made is negligible. In this thesis, I will refer to this correction as *stabilized integrator*. To give an example: a trajectory is initialized at time t_0 on the NHIM obtained with very high precision (rel. error of 10^{-12}) using the BCM. Afterwards, this trajectory is propagated for a fixed and appropriately chosen short time step Δt . In case of the model system according to Eq. (3.1) with standard parameters an adequate choice usually is $\Delta t = T$ but depending on the system or the external driving other choices might be reasonable. After this fixed time step Δt , the propagated trajectory at orthogonal modes $\mathbf{y}^{\text{traj}}(t_0 + \Delta t)$ and respective velocities $\mathbf{v}_y^{\text{traj}}(t_0 + \Delta t)$ might have left the NHIM by a distance Δx and by a velocity Δv_x in the unstable direction, as it is the case for the trajectories shown in

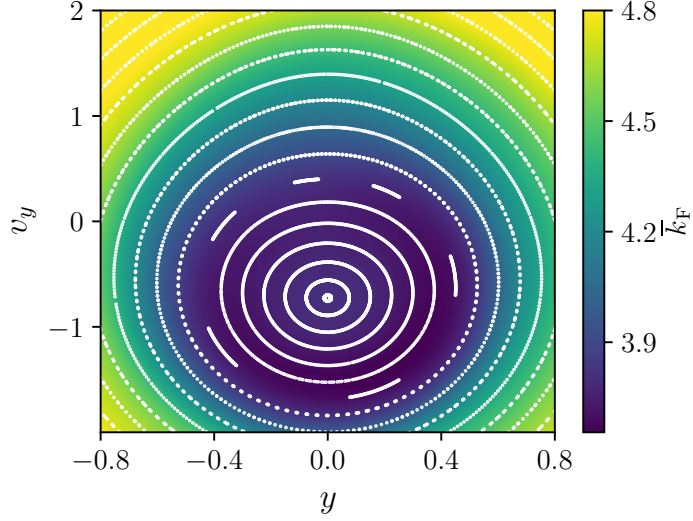


Figure 3.11.: PSOS for the two-dimensional model system according to Eq. (3.1). Selected trajectories on the NHIM are obtained using the stabilized propagator with $\Delta t = T = 2$. Their instantaneous positions $y(t = nT)$ and associated velocities $v_y(t = nT)$ on the NHIM are marked with a white dot at integer multiples n of the period T of the external driving. Apparently, the trajectories inside the time-periodically driven NHIM are located on stable tori around a periodic trajectory corresponding to the elliptic fixed point in their center. The color encoding gives the associated mean Floquet rates \bar{k}_F obtained as explained in Sec. 4.4. A similar figure has been published in Ref. [82].

Fig. 3.10. Therefore, its instantaneous position has to be compared to the associated position $(x^{\text{NHIM}}, v_x^{\text{NHIM}})(\mathbf{y}^{\text{traj}}, \mathbf{v}_y^{\text{traj}}, t_0 + T)$ on the NHIM, again obtained using a very precise BCM calculation. Assuming that Δt is sufficiently small such that the exponentially small deviation from the NHIM is negligible compared to the movement of the trajectory in the orthogonal modes, it is projected back onto the NHIM by setting $\Delta x = 0$ and $\Delta v_x = 0$. This projection is repeated after each time step Δt . In doing so, a trajectory is stabilized to the NHIM and a departure as in Fig. 3.10 will be prevented. A further discussion on the departure of trajectories from the unstable NHIM can be found in Ref. [68].

An alternative method to stabilize trajectories to the NHIM was examined in a master's thesis [83] at our institute and was published in Ref. [84]. In contrast to the therein used machine-learning based method, the BCM is considerably slower but more accurate since it in principle allows to obtain the NHIM with machine precision. If, however, e.g., a NN is already trained and performance is desired, such a machine learning based stabilization provides a faster and less precise alternative to the method described in this work.

Using a stabilized integrator allows to propagate trajectories on the NHIM for a very long time what is the basic requirement to examine the dynamics on the NHIM by means of a PSOS. Therefore, several trajectories initialized at various positions on the NHIM are propagated for many oscillations of a time-periodically driven barrier. After integer multiples of the period T , their instantaneous position $(\mathbf{y}, \mathbf{v}_\mathbf{y})$ on the NHIM can be monitored. Exemplary for the two-dimensional model system according to Eq. (3.1), such a PSOS is displayed in Fig. 3.11 with white dots. Here, the existence of ellipses (quasi-periodic trajectories) around a stable fixed point (periodic trajectory) is obvious and, hence, the trajectories on the time-dependent NHIM are located on regular tori. The PSOS in Fig. 3.11 is also some kind of consistency check for the stabilized integrator since too large errors in projecting back onto the NHIM would make the trajectories leave the tori for large integration times.

Whereas the dynamics of trajectories on the NHIM according to Fig. 3.11 is very regular, the situation usually becomes much more complicated – depending on the amplitude and the frequency of the external driving. Exemplary, the corresponding dynamics on the NHIM will be examined in Sec. 5.3 by means of the periodically driven LiCN isomerization reaction. Here, the tori are structured much more complicated and additional stable and unstable fixed points arise in the corresponding PSOS. This emergence of additional fixed points via bifurcations when gradually changing the parameters of the external driving has been further examined in a Bachelor’s thesis [85] at our institute.

4

Phase-space resolved decay rates for driven systems

This section starts in Sec. 4.1 with explaining the term *phase-space resolved decay rates* in the context of TST for driven systems. Afterwards, three different methods are introduced which, ultimately, yield the same decay rate. Whereas in the *ensemble method* according to Sec. 4.2 an ensemble of reactive trajectories is propagated according to the EOM, the *local manifold analysis*, introduced in Sec. 4.3, skips this time-consuming step using a linearization of the dynamics close to the TS. The third method, referred to as *Floquet method* in Sec. 4.4, uses the stability of trajectories on the NHIM to obtain phase-space resolved decay rates. Essential parts of this Chapter have been published in Ref. [82].

4.1

Decay rates close to transition states in driven systems

Trajectories in the intermediate TS of a rank-1 saddle between reactants and products are mathematically bound to the barrier region forever. They are embedded in an invariant manifold, called the NHIM. The NHIM is unstable and trajectories having just the smallest deviation from it will depart to either the reactant or the product side.

In the case of a static barrier, the energy is strictly conserved and trajectories on the NHIM are periodic. Other trajectories, which are located in a local neighborhood of such a periodic trajectory on the NHIM, depart exponentially fast to either the reactant or to the product side. This departure of trajectories is associated to a rate, referred to as reactant population close to the TS, see Sec. 2.2.2.

If a rank-1 saddle is time-periodically driven, trajectories in a non-chaotic regime of the NHIM are located on regular tori, see, e. g., Fig. 3.11 for the two-dimensional driven

model system or Fig. 5.16 for the driven $\text{LiCN} \rightleftharpoons \text{LiNC}$ isomerization reaction. Energy in those driven systems is usually not conserved and the position $(x^{\text{NHIM}}, p_x^{\text{NHIM}})(\mathbf{y}, \mathbf{v}_y, t)$ of the NHIM for given orthogonal modes \mathbf{y} and \mathbf{p}_y becomes time-dependent.

In such a driven system the exponentially fast decay of the number of reactants $N_{\text{react}}(\mathbf{y}, \mathbf{p}_y, t)$ in the local neighborhood of a specific position $(\mathbf{y}, \mathbf{p}_y)$ on the NHIM at a given time t becomes explicitly time-dependent

$$\frac{d}{dt} N_{\text{react}}(\mathbf{y}, \mathbf{p}_y, t) = -k(\mathbf{y}, \mathbf{p}_y, t) N_{\text{react}}(\mathbf{y}, \mathbf{p}_y, t) , \quad (4.1)$$

where

$$\begin{aligned} k(\mathbf{y}, \mathbf{p}_y, t) &= -\frac{1}{N_{\text{react}}(\mathbf{y}, \mathbf{p}_y, t)} \frac{d}{dt} N_{\text{react}}(\mathbf{y}, \mathbf{p}_y, t) \\ &= -\frac{d}{dt} \ln[N_{\text{react}}(\mathbf{y}, \mathbf{p}_y, t)] \end{aligned} \quad (4.2)$$

is the *instantaneous* and *phase-space resolved decay rate* of reactant population close to the position \mathbf{y} and \mathbf{p}_y of the TS.

Within a local neighborhood x and p_x of a (time-periodically driven) NHIM, departing trajectories in the unstable direction of the barrier approximately follow an associated trapped trajectory with orthogonal modes $\mathbf{y}(t)$ and $\mathbf{p}_y(t)$ when projected onto the NHIM. The corresponding instantaneous decay rates $k(\mathbf{y}, \mathbf{p}_y, t)$ of reactant population close to these positions $(\mathbf{y}, \mathbf{p}_y)$ on the NHIM alter over time. This effect also occurs even in the case of a time-independent multidimensional barrier according to Sec. 2.2.2 along the periodic trajectories on the NHIM.

If the barrier is time-periodically driven with a certain period T and we regard a periodic trajectory on the NHIM with the same period, then also the associated instantaneous decay rate $k(\mathbf{y}, \mathbf{p}_y, t)$ is periodic with T . In the more general and more frequent case of a quasi-periodic trajectory on the NHIM, the instantaneous decay rate of such a bound trajectory will also be quasi-periodic.

Usually, the variation of the instantaneous decay rates associated with a specific trajectory on the NHIM is rather small and, therefore, reactive trajectories initialized on the reactant side in a close neighborhood x and p_x to such a trapped trajectory depart “approximately exponentially fast” to the product side according to a mean decay rate – at least in a local neighborhood of the NHIM. This fact was already briefly mentioned in Sec. 2.2.2. The mean exponential departure of these trajectories is obtained by averaging the instantaneous decay rates $k(\mathbf{y}, \mathbf{p}_y, t)$ along a specific trajectory on such a stable torus. Here, an averaged *mean decay rate* associated with this torus can be obtained

$$\bar{k}|_{\text{torus}} = \frac{1}{t_1 - t_0} \int_{t_0}^{t_1} k(\mathbf{y}, \mathbf{p}_y, t) dt \quad \text{with } t_0 < t_1 . \quad (4.3)$$

The interval $[t_0, t_1]$ of the integral in Eq. (4.3) has to be chosen such that it covers the relevant timescale of a system. This might be a full period T , if the respective trajectory

on the NHIM is periodic, or several rounds on a torus to average over a quasi-periodic trajectory.

According to Eq. (4.3), the mean decay rate only depends on the respective torus but not on a specific position on it. Since quasi-periodic trajectories usually cover the full area of such a torus when propagated for long enough time, any trajectory initialized somewhere on the same torus is associated with the same mean decay rate although the corresponding instantaneous decay rates at a given time t might be completely different. Exemplary, this fact is visualized in Fig. 3.11 for the two-dimensional model system. Here, the mean decay rates k_F , obtained via the Floquet method according to Sec. 4.4 and displayed as color encoding, perfectly match the concentric ellipses of the PSOS given in white dots.

4.2 Ensemble method

A simple and intuitive method to numerically obtain instantaneous decay rates of reactant population close to a trajectory in the TS according to Eq. (4.2) is visualized in Fig. 4.1. In the local neighborhood (x, p_x) of a point on this trajectory the dynamics is linear to a good approximation and, therefore, the fibers of the stable \mathcal{W}_s and of the unstable \mathcal{W}_u manifold appear as straight lines in Fig. 4.1. They intersect in the corresponding point $(x^{\text{NHIM}}, p_x^{\text{NHIM}})(\mathbf{y}, \mathbf{p}_y, t_0)$ of the regarded bound trajectory on the NHIM at time t_0 .

In this (x, p_x) cross section a linear ensemble of N_{react} reactive trajectories is initialized equidistantly and parallel to the fiber of the unstable manifold \mathcal{W}_u with a small distance Δx on the reactant side, see red dots in Fig. 4.1. Thereby, the initial positions and momenta in the orthogonal modes are set to correspond to $(\mathbf{y}(t_0), \mathbf{p}_y(t_0))$. If Δx is chosen small enough such that the approximation of linear dynamics holds, this ensemble will evenly and asymptotically fast approach the stable manifold \mathcal{W}_s , while following the trajectory on the NHIM with respect to the orthogonal modes. At the same time, it is stretched exponentially fast in the direction of the unstable manifold \mathcal{W}_u .

In Fig. 4.1, this fact is visualized in diamonds indicating the according to the EOM propagated initial ensemble at some time $t_1 > t_0$ with the origin of coordinates fixed to the trajectory on the NHIM. Now, some of the initially N_{react} reactive trajectories may have pierced the DS to the product side $x > x^{\text{NHIM}}$ (blue diamonds) whereas others are still reactants (red diamonds). According to Eq. (4.2), this decay of the number of reactants is according to Eq. (4.2) associated to a rate $k_{\text{ens}}(\mathbf{y}, \mathbf{p}_y, t) = k(\mathbf{y}, \mathbf{p}_y, t)$, which is referred to as *instantaneous ensemble rate* to emphasize that it is obtained by propagating an ensemble of reactive trajectories according to the EOM.

To obtain the time-dependent number of reactants $N_{\text{react}}(\mathbf{y}, \mathbf{p}_y, t)$ any trajectory of the initial ensemble is propagated in time separately and for each trajectory the corresponding DS is individually obtained. At the specific time $t = t^+$ a trajectory crosses

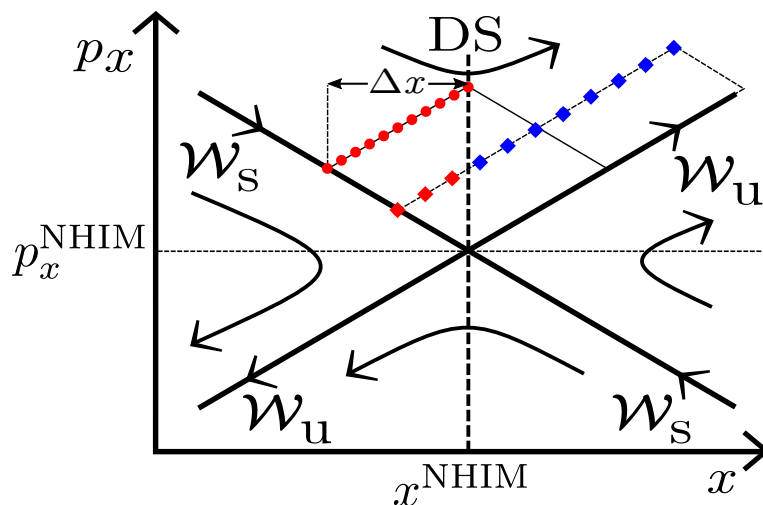


Figure 4.1.: Phase-space section (x, p_x) in a very close neighborhood of a point of the NHIM, $(x^{\text{NHIM}}, p_x^{\text{NHIM}})(\mathbf{y}, \mathbf{p}_y, t)$, which is given by the intersection of the fibers of the stable \mathcal{W}_s and the unstable \mathcal{W}_u manifold corresponding to the orthogonal modes $(\mathbf{y}, \mathbf{p}_y)$ at the respective time t . Here, the dynamics is linear and the manifolds are not curved. A reactive ensemble (red dots) is initialized parallel to the unstable manifold \mathcal{W}_u at initial time t_0 with a distance Δx equidistantly in between the stable manifold and the DS (vertical dashed line). By propagation in time it approaches the unstable manifold exponentially slow while being stretched exponentially fast in direction of the unstable manifold, as indicated in diamonds. After a certain time $t_0 + t$ some of these trajectories pierced the DS to the product side (blue diamonds) while others are still reactant (red diamonds).

its individual DS the corresponding the number of reactants decreases by one and the propagation of the respective trajectory can be stopped.

Obtaining decay rates by means of the ensemble method is conceptually very simple as it only requires to propagate trajectories (also for the BCM) and to count the time-dependent number of reactants. However, two technical subtleties have to be considered in its application. First of all, the ensemble of reactive trajectories is initialized close to a bound trajectory on the NHIM and approximately follows this trajectory. For longer propagation times t , however, this approximation may break down and the corresponding positions $(\mathbf{y}(t), \mathbf{p}_y(t))$ of the various reactive trajectories may differ from the respective position $(\mathbf{y}(t), \mathbf{p}_y(t))$ of the bound trajectory on the NHIM. In that case, the decay rates associated with these “run away” trajectories would correspond to a different bound trajectory on the NHIM and therefore would obfuscate the desired result.

The other difficulty lies in the nature of the dynamics close to the NHIM. Due to the exponential stretching of the initially equidistant ensemble a lot of its trajectories

will react very fast and only a minority of trajectories will stay on the reactant side for longer propagation times. In other words, the decrease in the number of reactants over time will be fast in the beginning but exponentially slower with longer propagation time and, therefore, $N_{\text{react}}(\mathbf{y}, \mathbf{p}_y, t)$ is a step function with exponentially increasing stepsize. This, however, means that the density of points of this discrete function is exponentially decreasing and, consequently, the error of its numeric derivative is increasing over time.

A simple solution to these technical difficulties for longer integration times is to propagate the initial ensemble only for a short time Δt and, afterwards, initialize a new ensemble close to the respective new position $(\mathbf{y}(t + \Delta t), \mathbf{p}_y(t + \Delta t))$ of the same bound trajectory on the NHIM. The so-obtained parts of the ensemble rate can afterwards be patched together to yield the full instantaneous ensemble rate of the respective bound trajectory on the NHIM.

Whereas, e.g., in Refs. [29, 53, 54, 86] thousands to millions of reactive trajectories had to be propagated to somehow resolve a rate constant, with the ensemble method introduced here instantaneous decay rates of reactant population close to the TS can be adequately resolved by propagating just a few tens to hundreds of reactive trajectories.

Although being conceptually simple, the ensemble method is numerically very expensive since for each reactive trajectory the instantaneous position of the DS is obtained individually using the BCM. Whereas in principle machine learning methods are able to provide a much faster access to the NHIM, they have proven to be too imprecise for this task [87]. Since trajectories are initialized in a very close neighborhood of the NHIM (usually $\Delta x = 10^{-2}$ to 10^{-3} for the two-dimensional model system according to Eq. (3.1)), highly precise knowledge of the position of the NHIM is crucial for the ensemble method. Therefore, using the rather expensive BCM is necessary here.

4.3 | Local manifold analysis

Propagating reactive trajectories according to the ensemble method of Sec. 4.2 is just one way to obtain instantaneous decay rates of reactant population close to the TS. Alternatively, the geometry of the phase space can be utilized in a regime very close to the NHIM. Here, the dynamics is linear to a good approximation and an analysis of the slopes of its stable and unstable manifolds – referred to as the local manifold analysis (LMA) – provides a considerably faster approach to obtain decay rates of the TS. In a sense, the ensemble method according to Sec. 4.2 and the LMA are based on the same central idea of linear dynamics in a close neighborhood of the NHIM. Thus, the LMA can be seen as an extension to the ensemble method which skips the propagation of a possibly large number of reactive trajectories using a linearization of the dynamics. In doing so, just very few calls of the BCM are needed. From another perspective, the ensemble method provides a possibility to verify the LMA with respect to the assumptions made when skipping the actual propagation of trajectories. If applied

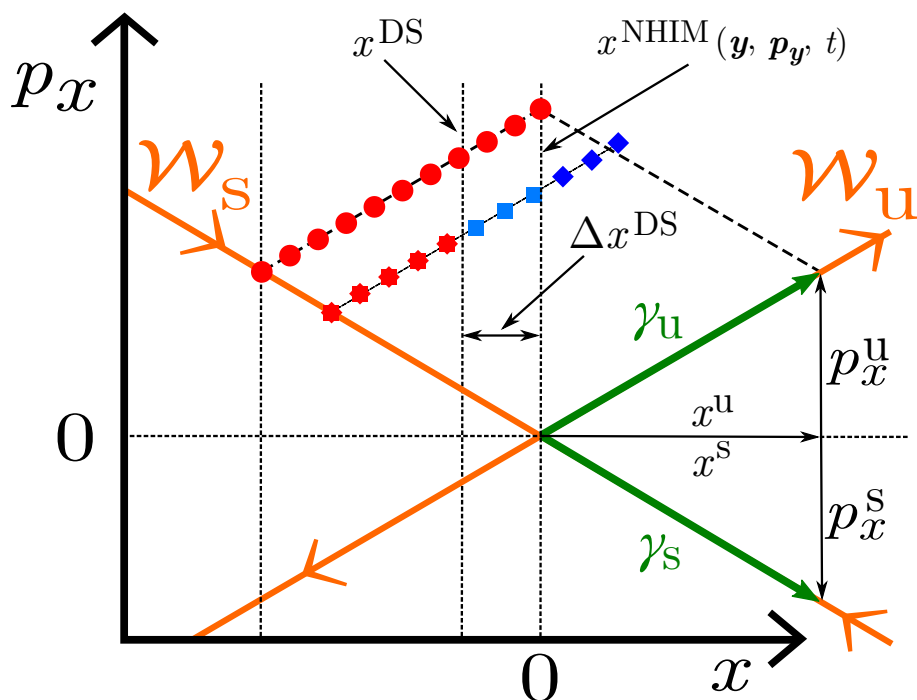


Figure 4.2.: Schematic (x, p_x) cross section of the phase space in a close neighborhood $(\mathbf{y}, \mathbf{p}_y, t)$ of a point on a specific trajectory on the NHIM. This figure illustrates two contributions of a reactive ensemble to a decay rate. One is based on the ensemble moving with respect to the trajectory on the NHIM (dark blue diamonds), the other is based on a “relative movement” of the DS for an ensemble which turned out of this (x, p_x) -plane (light blue squares). For further information, see text.

correctly both methods ultimately yield the same instantaneous decay rate of reactant population close to the TS.

To explain the LMA we consider an n -dimensional Hamiltonian system at time t for which a state is characterized by a phase space vector

$$\boldsymbol{\gamma}(t) = (x(t), \mathbf{y}(t), p_x(t), \mathbf{p}_y(t))^T. \quad (4.4)$$

Here, x denotes the reaction coordinate with conjugated momentum p_x and \mathbf{y} are the $(n-1)$ -dimensional orthogonal modes with conjugated momenta \mathbf{p}_y . In Fig. 4.2 an (x, p_x) cross section of the full phase space of such a system is sketched in a close neighborhood to a point $(\mathbf{y}, \mathbf{p}_y, t)$ of a specific trajectory on the NHIM. Since the dynamics is linear here, the fibers of the stable \mathcal{W}_s and the unstable \mathcal{W}_u manifolds appear as straight lines. They intersect in a point $(x^{\text{NHIM}}, p_x^{\text{NHIM}})(\mathbf{y}, \mathbf{p}_y, t)$ of a specific trajectory on the NHIM. Without loss of generality, the origin of coordinates is instantaneously attached to this trajectory.

To obtain decay rates of reactant population in a close neighborhood of the TS we start imagining a linear ensemble of reactive trajectories, see red bullets in Fig. 4.2. Similar to the ensemble method according to Sec. 4.2, this ensemble is initialized parallel to the unstable manifold \mathcal{W}_u at a specific time t in our cross section with a small x -span in between the fiber of the stable manifold and the DS attached to the point $(\mathbf{y}, \mathbf{p}_y, t)$ of the regarded trajectory on the NHIM.

When propagated for a small time Δt it will, in general, turn out of the $(x, p_x)(\mathbf{y}(t + \Delta t), \mathbf{p}_y(t + \Delta t), t + \Delta t)$ -plane which is instantaneously attached to the regarded trajectory on the NHIM towards some other orthogonal modes $\mathbf{y}(t + \Delta t)$ and $\mathbf{p}_y(t + \Delta t)$. Since the dynamics is linear in a close neighborhood of the NHIM, this out-of-plane ensemble will still be located on a straight line. However, it will pierce the DS at some generally different position $x^{\text{DS}}(t + \Delta t) \neq 0$. Still, one can imagine to project back the ensemble into the $(x, p_x)(\mathbf{y}(t + \Delta t), \mathbf{p}_y(t + \Delta t), t + \Delta t)$ -plane attached to the regarded trajectory on the NHIM. As sketched in Fig. 4.2, this projected ensemble at time $t + \Delta t$ will also be linear and the difference $\Delta x^{\text{DS}}(t + \Delta t)$ between the position $x^{\text{DS}}(t + \Delta t)$ at which the out-of-plane pierces the DS and the position $x = 0$ of the DS attached to the trajectory on the NHIM is directly visible. By geometric considerations one can calculate the instantaneous decay of reactant population towards the product side – provided that the position $x^{\text{DS}}(t + \Delta t)$ is known.

According to Fig. 4.2, two effects need to be considered when calculating decay rates of reactant population in a close neighborhood of a specific trajectory on the NHIM. As a first contribution to the decay rate, some fraction of this propagated and projected ensemble at time $t + \Delta t$ will have pierced the DS attached to the NHIM at position $x = 0$ towards the product side, see dark blue diamonds in Fig. 4.2. The associated instantaneous decay rate $k^{\text{ens}}(t)$ arises from the movement of the ensemble relative to the trajectory on the NHIM. This movement is prescribed by the stable and the unstable manifold and can be expressed, as will be shown in Sec. 4.3.1, solely from the slopes of their fibers. However, depending on the positions $(\mathbf{y}, \mathbf{p}_y)$ the initially in-plane ensemble has turned to, outside the instantaneous (x, p_x) cross section attached to the regarded trajectory on the NHIM, the ensemble has actually pierced the DS at position $x^{\text{DS}} \neq 0$. Consequently, an additional fraction of its trajectories, see light blue squares in Fig. 4.2, has contributed to a decay rate by $k^{\text{DS}}(t)$ due to a “relative movement” of the DS. This second part of the total decay rate will be derived in Sec. 4.3.2.

When regarding both effects, the total instantaneous decay rate of reactant population close to the TS for a point $(\mathbf{y}(t), \mathbf{p}_y(t))$ of a specific trajectory on the NHIM at a certain time t yields

$$k_{\text{M}}(\mathbf{y}, \mathbf{p}_y, t) = k^{\text{ens}}(\mathbf{y}, \mathbf{p}_y, t) + k^{\text{DS}}(\mathbf{y}, \mathbf{p}_y, t) . \quad (4.5)$$

Here, the name k_{M} is to emphasize that it is obtained by the LMA.

In the special case of a one-dimensional system characterized by a phase space (x, p_x) , an “in plane” initialized ensemble cannot turn out of plane – because of the non-existing

orthogonal modes – and, thus, $k^{\text{DS}}(t) = 0$. Consequently, Eq. (4.5) simplifies to

$$k_{\text{M}}^{\text{1D}}(t) = k^{\text{ens}}(t) \quad (4.6)$$

and yields the time-dependent decay rate of the TS trajectory – which is the only trajectory on the NHIM of a one-dimensional system.

4.3.1 The ensemble part

In this section the term $k^{\text{ens}}(\mathbf{y}, \mathbf{p}_{\mathbf{y}}, t)$ of Eq. (4.5) will be discussed. It describes the movement of the imagined ensemble relative to a corresponding trajectory on the NHIM. This movement can be adequately described by projecting the ensemble into the (x, p_x) -plane which is instantaneously attached to this trajectory. Because of this projection, a quasi-one-dimensional system emerges and, thus, we will formally derive $k_{\text{M}}^{\text{ens}}(t)$ for a one-dimensional system. Afterwards, the result will be generalized to multidimensional systems including the orthogonal modes.

We start considering a one-dimensional and time-dependent Hamiltonian system with equations of motion of the form

$$\dot{\boldsymbol{\gamma}}(t) = \begin{pmatrix} 0 & 1 \\ -1 & 0 \end{pmatrix} \frac{\partial^2 \mathcal{H}(t)}{\partial \boldsymbol{\gamma}(t)^2} \boldsymbol{\gamma}(t) \equiv \mathbf{J}(t) \boldsymbol{\gamma}(t) \quad (4.7)$$

for the state $\boldsymbol{\gamma}(t) = (x(t), p_x(t))^{\text{T}}$ with position $x(t)$ and conjugated momentum $p_x(t)$ at time t . Here, $\mathcal{H}(t)$ is the Hamiltonian of the system and $\mathbf{J}(t)$ is the corresponding Jacobian. In a close neighborhood of the NHIM the dynamics is linear and the unstable \mathcal{W}_{s} as well as the stable manifold \mathcal{W}_{u} appear approximately as straight lines, see Fig. 4.2, whose orientations are given by the vectors

$$\boldsymbol{\gamma}^{\text{u}}(t) = \begin{pmatrix} x^{\text{u}}(t) \\ p_x^{\text{u}}(t) \end{pmatrix} \quad \text{and} \quad \boldsymbol{\gamma}^{\text{s}}(t) = \begin{pmatrix} x^{\text{s}}(t) \\ p_x^{\text{s}}(t) \end{pmatrix}. \quad (4.8)$$

In this linear regime, the dynamics is described by a fundamental matrix $\boldsymbol{\sigma}(t, t_0)$ which is defined by a differential equation

$$\frac{d\boldsymbol{\sigma}(t, t_0)}{dt} = \mathbf{J}(t) \boldsymbol{\sigma}(t, t_0) \quad \text{with} \quad \boldsymbol{\sigma}(t_0, t_0) = \mathbb{1}. \quad (4.9)$$

Hence, the fundamental matrix $\boldsymbol{\sigma}(t, t_0)$ can be obtained by integrating Eq. (4.9) from an known initial state $\boldsymbol{\gamma}(t_0)$ a time t_0 . In the linearized dynamics, it serves as a propagator, i. e., $\boldsymbol{\gamma}(t) = \boldsymbol{\sigma}(t, t_0) \boldsymbol{\gamma}(t_0)$.

According to Fig. 4.2, the LMA starts imagining a linear ensemble which is initialized symmetrically ($x^{\text{u}}(t_0) = x^{\text{s}}(t_0)$) at time t_0 and described by

$$\boldsymbol{\gamma}_{\text{E}}(a, t_0) = \begin{pmatrix} (a-1) x^{\text{u}}(t_0) \\ -p_x^{\text{s}}(t_0) + a p_x^{\text{u}}(t_0) \end{pmatrix}. \quad (4.10)$$

Here, $a \in [0, 1]$ is a line parameter parametrizing the ensemble in between the stable manifold and the DS. Hence, $a = 0$ corresponds to the intersection of the ensemble with the stable manifold and $a = 1$ to the trajectory currently piercing the DS.

Similar to the ensemble method, an instantaneous decay rate for the flux of this initial ensemble from the reactant side towards the product side can be obtained by monitoring the instantaneous decrease in the number of reactants $N_{\text{react}}(t)$

$$k(t) = -\frac{d}{dt} \ln(N_{\text{react}}(t)) . \quad (4.11)$$

However, unlike propagating the reactive ensemble directly using the EOM, here, the parametrization (4.10) by means of the line parameter a can be used to obtain the reactive flux according to the linearized dynamics. Therefore, the specific parameter $a_{\text{DS}}(t) \in [0, 1]$ associated with the time-dependent crossing point of the linear ensemble with the DS at a specific time t is sought for. By construction, initially $a_{\text{DS}}(t_0) = 1$ and all reactive trajectories are located on the reactant side, see red bullets in Fig. 4.2. However, at a certain time $t > t_0$ some of the trajectories initialized on the reactant side have crossed the DS to the product side (dark blue diamonds in Fig. 4.2). Since $a \in [0, 1]$ still parametrizes the full linear ensemble which becomes stretched exponentially fast in the unstable direction because of the dynamics close to the NHIM, now, $a_{\text{DS}}(t)$ is smaller than one. In other words, $a_{\text{DS}}(t) \in [0, 1]$ describes the instantaneous fraction of the linear ensemble that is still on the reactant side at a given time t . Consequently, the decrease of the number of reactants is directly proportional to the change of the line parameter $a_{\text{DS}}(t)$. Thus, N_{react} in Eq. 4.11 can be re-expressed in terms of $a_{\text{DS}}(t)$

$$k(t) = -\frac{d}{dt} \ln(a_{\text{DS}}(t)) , \quad (4.12)$$

and, consequently, to calculate the instantaneous decay rate at a specific time t , we first need to determine the time-dependent intersection $a_{\text{DS}}(t)$ of our linear ensemble with the DS.

Using to the fundamental matrix defined in (4.9) the initial ensemble $\gamma_{\text{E}}(a, t_0)$ according to Eq. (4.10) can be propagated to $t > t_0$ by

$$\gamma_{\text{E}}(a, t) = \sigma(t, t_0) \gamma_{\text{E}}(a, t_0) . \quad (4.13)$$

Thereby, we keep the origin of the reference frame fixed to the regarded trajectory on the NHIM and, consequently, the dividing surface at time t is still located at $x = 0$. This fact yields a conditional equation

$$\sigma(t, t_0) \gamma_{\text{E}}(a_{\text{DS}}(t), t_0) \cdot \mathbf{e}_x \stackrel{!}{=} 0 \quad (4.14a)$$

$$\Leftrightarrow \sigma_{x,x}(t, t_0) [a_{\text{DS}}(t) - 1] x^{\text{u}}(t_0) + \sigma_{x,p_x}(t, t_0) [-p_x^{\text{s}}(t_0) + a_{\text{DS}}(t) p_x^{\text{u}}(t_0)] \stackrel{!}{=} 0 \quad (4.14b)$$

to determine

$$a_{\text{DS}}(t) = \frac{\sigma_{x,x}(t, t_0) x^{\text{u}}(t_0) + \sigma_{x,p_x}(t, t_0) p_x^{\text{s}}(t_0)}{\sigma_{x,x}(t, t_0) x^{\text{u}}(t_0) + \sigma_{x,p_x}(t, t_0) p_x^{\text{u}}(t_0)} . \quad (4.15)$$

Here, e. g., σ_{x,p_x} is the x,p_x -component of the matrix σ . As a test: Eq. (4.15) is valid for any time t . Thus, it especially holds for the initial time $t = t_0$. Consequently, at $t = t_0$, with $\sigma(t_0, t_0) = \mathbb{1}$ this equation results in $a_{\text{DS}}(t_0) = 1$ since all trajectories of the initial ensemble are still located on the reactant side.

To obtain an instantaneous rate according to Eq. (4.12) at this initial time t_0 , the time derivative of $a_{\text{DS}}(t_0)$ is needed which can be obtained using the quotient rule

$$\left(\frac{da_{\text{DS}}(t)}{dt} \right) \Big|_{t=t_0} = - \frac{d\sigma_{x,p_x}(t_0, t_0)}{dt} \frac{p_x^u(t_0) - p_x^s(t_0)}{x^u(t_0)}. \quad (4.16)$$

Using Eq. (4.9) this equation can be simplified by

$$\frac{d\sigma_{x,p_x}(t_0, t_0)}{dt} = (\mathbf{J}(t_0) \sigma(t_0, t_0))_{x,p_x} = \mathbf{J}_{x,p_x}(t_0), \quad (4.17)$$

where again $\sigma(t_0, t_0) = \mathbb{1}$ is used.

In conclusion, the instantaneous decay rate $k(t_0) \equiv k^{\text{ens}}(t_0)$ of the TS of a one-dimensional and time-dependent system at a specific time t_0 yields

$$k^{\text{ens}}(t_0) = \mathbf{J}_{x,p_x}(t_0) \frac{p_x^u(t_0) - p_x^s(t_0)}{x^u(t_0)}, \quad (4.18)$$

using a geometrical analysis of the stable and unstable manifolds in a linear regime close to the associated NHIM of a barrier. Since, e. g., $p_x^u(t_0)/x^u(t_0)$ is the slope of the fiber of the unstable manifold in Fig. 4.2, the instantaneous decay rate $k^{\text{ens}}(t_0)$ is according to Eq. (4.18) given by the difference of the slopes of the fibers of the unstable and the stable manifold – multiplied by the (x, p_x) -entry of the corresponding Jacobian. Since an analysis according to Eq. (4.18) can be done not only for t_0 but for any time t , the corresponding rate $k^{\text{ens}}(t)$ yields the ensemble part of Eq. (4.5).

Although being derived for a one-dimensional system in which the NHIM contains only the single TS trajectory, Eq. (4.18) is also valid for multidimensional systems including the orthogonal modes. In that case, however, an infinite number of trajectories is located on the NHIM, and each trajectory is characterized by its own decay rate. For a point $(\mathbf{y}(t), \mathbf{p}_y(t))$ of such a trajectory on the NHIM at a given time t , the ensemble part of the LMA yields

$$k^{\text{ens}}(\mathbf{y}, \mathbf{p}_y, t) = \left[\mathbf{J}_{x,p_x}(t) \frac{p_x^u(t) - p_x^s(t)}{x^u(t)} \right] \Big|_{(\mathbf{y}, \mathbf{p}_y, t)}. \quad (4.19)$$

Hence, it is obtained geometrically from the difference of the slopes of the stable and the unstable manifold (times the Jacobian prefactor).

4.3.2 The DS part

In this section the second part $k^{\text{DS}}(\mathbf{y}, \mathbf{p}_y, t)$ of Eq. (4.5) is derived which considers the “relative movement” of the DS for an ensemble that has turned out of the (x, p_x) -plane instantaneously attached to a specific trajectory on the NHIM. As visualized in Fig. 4.2, such an out-of-plane ensemble will, in general, pierce the DS at some other position $x^{\text{DS}} \neq 0$. As a consequence, the number of reactants changes by some amount ΔN_{react} , depicted by the light blue squares in Fig. 4.2. According to Eq. (4.11), this change ΔN_{react} contributes to the decay rate by

$$k^{\text{DS}}(t) = -\frac{\Delta \dot{N}_{\text{react}}(t)}{N_{\text{react}}(t)}. \quad (4.20)$$

For an infinitesimal time step Δt the change ΔN_{react} in Eq. (4.20) can be expressed by

$$\Delta N_{\text{react}}(t) = \frac{\Delta x^{\text{DS}}(t + \Delta t)}{x^u(t)} N_{\text{react}}(t). \quad (4.21)$$

Here, $x^u(t) = x^s(t)$ is the x -span of an imagined ensemble of $N_{\text{react}}(t)$ reactive trajectories which are initialized at time t according to Fig. 4.2 in an $(x, p_x)(\mathbf{y}, \mathbf{p}_y, t)$ cross section of the full phase space. The difference $\Delta x^{\text{DS}}(t + \Delta t)$ is measured in between the position $x^{\text{DS}}(t + \Delta t)$ at which the out-of-plane ensemble pierces the DS and the position $x^{\text{NHIM}} = 0$ of the regarded trajectory on the NHIM. The term $\Delta x^{\text{DS}}(t + \Delta t)/x^u(t)$ on the right-hand side of Eq. (4.21) is exactly the fraction by which the initial number of reactants $N_{\text{react}}(t)$ is reduced by the “relative movement” of the DS. To give an example, if the DS at time $t = t + \Delta t$ would have moved towards $x < 0$ for half the span $x^u(t)$ of the initial ensemble at time t , the change $\Delta N_{\text{react}}(t)$ would be $N_{\text{react}}(t)/2$. In reality, the correction $\Delta N_{\text{react}}(t_0)$ is much smaller since the time-step Δt is assumed to be infinitesimal.

By means of Eq. (4.21) the rate $k^{\text{DS}}(t)$ in Eq. (4.20) yields

$$k^{\text{DS}}(t) = -\frac{\Delta \dot{x}^{\text{DS}}(t + \Delta t)}{x^u(t)}. \quad (4.22)$$

Hence, the derivative of the distance $\Delta x^{\text{DS}}(t + \Delta t)$ with respect to Δt is sought for. Since Δt is small, the distance $\Delta x^{\text{DS}}(t + \Delta t)$ and its time-derivative are assumed to be of the form

$$\Delta x^{\text{DS}}(t + \Delta t) = c(\mathbf{y}, \mathbf{p}_y, t) \Delta p_x(t) \Delta t, \quad (4.23a)$$

$$\Delta \dot{x}^{\text{DS}}(t + \Delta t) = c(\mathbf{y}, \mathbf{p}_y, t) \Delta p_x(t), \quad (4.23b)$$

i. e., the leading order of a Taylor expansion in Δt and Δp_x with an expansion coefficient $c(\mathbf{y}, \mathbf{p}_y, t)$ which may depend on the orthogonal modes for a given time t . Here, at time t , $\Delta p_x(t)$ is the p_x -distance of a specific trajectory towards the regarded trajectory on the NHIM.

The ansatz (4.23) is reasonable since $\Delta x^{\text{DS}}(t + \Delta t)$ is zero for a trajectory initialized with $\Delta p_x = 0$ directly on the NHIM in the respective (x, p_x) cross section. Such a trajectory will exactly follow the regarded trajectory on the NHIM and not move out of the attached cross section. Any other trajectory which is initialized with a distance Δp_x to the NHIM, however, will leave this cross section and will, therefore, see a DS that is shifted by $\Delta x^{\text{DS}}(t + \Delta t)$ at time $t + \Delta t$.

At time t and for infinitesimally small Δt the currently reacting trajectory of an ensemble initialized as explained in Fig. 4.2 will be located exactly at the top corner of the marked parallelogram at position $x^{\text{top}}(t) = 0$, $p_x^{\text{top}}(t) = -p_x^{\text{s}}(t) + p_x^{\text{u}}(t)$ according to Eq. (4.8), and at the orthogonal modes $(\mathbf{y}^{\text{top}}, \mathbf{p}_y^{\text{top}}) = (\mathbf{y}(t), \mathbf{p}_y(t))$. Using the respective equations of motion this single trajectory can be propagated for Δt towards a position $(x^{\text{top}}, p_x^{\text{top}}, \mathbf{y}^{\text{top}}, \mathbf{p}_y^{\text{top}})(t + \Delta t)$ which will, in general, be out of the (x, p_x) -plane attached to the position of the trajectory on the NHIM at time $t + \Delta t$. Now, the x -position of the DS for this out-of-plane trajectory is given by the x -position of its corresponding NHIM

$$x^{\text{DS}}(t + \Delta t) = x^{\text{NHIM}}(\mathbf{y}^{\text{top}}(t + \Delta t), \mathbf{p}_y^{\text{top}}(t + \Delta t), t + \Delta t) , \quad (4.24)$$

which can be found using the BCM and, consequently, the distance $\Delta x^{\text{DS}}(t + \Delta t)$, according to Fig. 4.2, is determined. Thus, the expansion coefficient

$$c(\mathbf{y}, \mathbf{p}_y, t) = \left[\frac{\Delta x^{\text{DS}}(t + \Delta t)}{\Delta t (p_x^{\text{u}}(t) - p_x^{\text{s}}(t))} \right] \Big|_{\mathbf{y}, \mathbf{p}_y, t} \quad (4.25)$$

can be obtained according to Eq. (4.23a) with $\Delta p_x(t) = p_x^{\text{u}}(t) - p_x^{\text{s}}(t)$ for the currently reacting trajectory at the top corner of the parallelogram in Fig. 4.2.

To put it all in a nutshell, to obtain the coefficient in Eq. (4.25) only a single trajectory has to be propagated according to the equations of motion for a small time-step Δt . Afterwards, the BCM is used to find the corresponding position of the DS. With this expansion coefficient the rate $k^{\text{DS}}(t)$ according to Eq. (4.22) yields

$$k^{\text{DS}}(\mathbf{y}, \mathbf{p}_y, t) = -c(\mathbf{y}, \mathbf{p}_y, t) \left[\frac{p_x^{\text{u}}(t) - p_x^{\text{s}}(t)}{x^{\text{u}}(t)} \right] \Big|_{\mathbf{y}, \mathbf{p}_y, t} = - \left[\frac{\Delta x^{\text{DS}}(t + \Delta t)}{x^{\text{u}}(t) \Delta t} \right] \Big|_{\mathbf{y}, \mathbf{p}_y, t} . \quad (4.26)$$

4.4 Floquet method

Both the ensemble method introduced in Sec. 4.2 and the LMA according to Sec. 4.3 are in principle based on the propagation of an ensemble of reactive trajectories to obtain decay rates of reactant population close to the TS. The latter, however, skips the actual propagation utilizing the properties of the linearized dynamics in the close neighborhood of the NHIM. If applied correctly, both methods yield the same instantaneous decay rates. According to Eq. (4.3), a corresponding mean decay rate can be obtained by appropriately averaging over the corresponding instantaneous decay rates of periodic or quasi-periodic trajectories on the NHIM.

In 2015, an alternative method to calculate the mean decay rate of reactant population close to the TS for one-dimensional time-periodically driven barriers was introduced by Craven, Bartsch and Hernandez [88]. In one-dimensional systems only the TS trajectory is located on the NHIM of the moving barrier. According to Ref. [88], the mean decay rate associated to this TS trajectory can be obtained directly from an analysis of its intrinsic stability – without propagating any reactive trajectory ensembles. The generalization of this *Floquet method* in order to obtain the mean decay rates of the in principle infinitely many quasi-periodic trajectories located on the NHIM of a multidimensional and time-periodically driven rank-1 barrier was done in our group at the ITP1 which resulted in several publications [29, 82, 84, 89].

According to Ref. [88], the information on the stability of the TS trajectory is encoded in the associated 2-dimensional *stability* or *monodromy matrix* [90]. The monodromy matrix $\mathbf{M}(T) = \boldsymbol{\sigma}(t_0 + T, t_0)$ is a special case of the fundamental matrix $\boldsymbol{\sigma}(t, t_0)$ already defined in Eq. (4.9) for a full period T of a periodic trajectory on the NHIM. For a one-dimensional system, it is obtained numerically by propagating $\mathbf{1}_2$ from an initial time t_0 towards $t_0 + T$ according to Eq. (4.9). Therefore, the Jacobian $\mathbf{J}(t)$ has to be calculated instantaneously according to Eq. (4.7) for the TS trajectory. Using the eigenvalues of the monodromy matrix the corresponding *Floquet exponents* can be defined

$$\mu_{l,s} = \frac{1}{T} \ln |m_{l,s}| . \quad (4.27)$$

Here, m_l is the larger eigenvalue and m_s is the smaller eigenvalue of $\mathbf{M}(T)$, respectively. Floquet exponents are a measure on how exponentially fast initially neighboring trajectories separate from each other [90] and, as a consequence, they are directly related to the dynamics prescribed by the stable and the unstable manifold in a close neighborhood of the TS. Since the TS is unstable with respect to the unstable degree of freedom – which is the only degree of freedom in a one-dimensional system – initially neighboring trajectories depart exponentially fast from the periodic TS trajectory, at least in its local neighborhood. This exponential separation is associated with a rate, referred to as the *Floquet rate*

$$k_F = \mu_l - \mu_s , \quad (4.28)$$

which is simply obtained by the difference of the two Floquet exponents. Since these Floquet exponents are obtained for a full period of the external driving, the Floquet-rate is an integrated quantity corresponding to the mean decay rate of reactant population close to the TS trajectory.

When changing to an ($n > 1$)-dimensional and time-periodically driven rank-1 barrier the situation becomes fundamentally different. As introduced in Sec. 2.1 and Sec. 3.2 the NHIM in these multidimensional systems is a $(2n - 2)$ -dimensional and non-trivially curved manifold moving in the barrier region. Inside this manifold, an infinite number of trajectories is trapped. However, just very few bound trajectories are periodic whereas nearly all of them usually show quasi-periodic behavior – as long as the dynamics in the orthogonal modes is not chaotic. For further details to the dynamics on the multidimensional NHIM see Sec. 3.5.

In the special case of periodic trajectories on the multidimensional driven NHIM, Floquet rates can still be obtained using the corresponding $2n$ -dimensional monodromy matrix. However, in the more general case of a quasi-periodic trajectory on the multidimensional NHIM the $2n$ -dimensional fundamental matrix $\sigma(t, t_0)$ according to Eq. (4.9) is needed to obtain decay rates. When calculated for a specific trajectory on the NHIM, the fundamental matrix – as a generalization of the monodromy matrix – also encodes the information on the trajectory’s stability. As in the one-dimensional case introduced in Ref. [88], two of its eigenvalues are corresponding to the unstable degree of freedom of the saddle. In that direction, trajectories will separate exponentially fast at least in a local neighborhood of the NHIM and, hence, the associated Floquet exponents (4.29) are not going to vanish. However, as the name indicates, the dynamics in all $(n - 1)$ stable directions of a rank-1 saddle is *stable* and initially neighboring trajectories do not separate exponentially fast with respect to these stable degrees of freedom – as long as the dynamics on the NHIM is not chaotic. Consequently, the corresponding Floquet exponents vanish, meaning that the related eigenvalues have an absolute value of one.

The decay rate of reactant population in the close neighborhood of such a quasi-periodic trajectory on the multidimensional NHIM still results, as given in Eq. (4.28), from the difference of the two non-vanishing Floquet exponents. Again, this decay rate has to be understood as a mean rate, integrated over the movement of a trajectory on the corresponding stable torus. Since the eigenvalues of $\sigma(t, t_0)$ will, in general, depend on the propagation time t of Eq. (4.9), Eq. (4.27) needs to be modified

$$\mu_{l,s} = \lim_{t \rightarrow \infty} \frac{1}{t} \ln |m_{l,s}(t)| . \quad (4.29)$$

Numerically, obtaining this infinite time limit is impossible and the integration time t must in practice be chosen sufficiently large to cover the relevant dynamics of the regarded trajectory on the NHIM, e. g., several rounds on a stable torus. In doing so, the Floquet rates for multidimensional systems are a specific property of the regarded trajectory and, therefore, will in general be different for various bound trajectories.

4.5 Applications

The methods introduced in Chapters 3 and 4 have been successfully applied to various systems in several theses which were, in part, supervised by me. In a Master's thesis [83], Floquet rates were obtained for the first time for stabilized trajectories on the time-periodically driven NHIM of the two-dimensional model system (3.1). Therefore, a continuous representation of the NHIM based on neural networks was used. The results are published in Ref. [84]. The continuous representation of the NHIM may significantly speed up rate calculations, a fact that has already been used in a Bachelor's thesis [91]. Representing the driven NHIM by machine learning methods is especially advisable for multidimensional systems. A first approach towards higher dimensions was done in a Master's thesis [92] by means of representing the NHIM of a three-dimensional extension of the model system with machine learning methods. The corresponding results are published in Ref. [54]. An application of the methods of Chapter 4 to this three-dimensional model system will be straightforward, yet remains to be done. Another extension to the existing theory for the reaction dynamics close to the NHIM of a driven rank-1 saddle was done by switching to a time-periodically driven two-saddle system in the context of a Master's thesis [93]. An important result of this work is, that trajectories bound to the barrier region can not only be found on the local NHIMs of either saddle but also bouncing in between them. These bouncing trajectories can, at least in a one-dimensional system, be used to attach a DS which minimizes possible recrossings with respect to both saddles. The results for the two-saddle system are currently submitted in Ref. [94]. For thermal systems, first steps in applying the current methods have also already been done and may be published soon, see Ref. [95].

Apart from developing methods by means of model systems, many of them were already applied to more realistic examples of reactions. In a Bachelor's thesis [96] the influence of the rotation of the moon on capturing asteroids at Lagrange points in space was examined. And in the field of spintronics, where equations of motion are known for the description of a spin flipping between two stable states within a solid, the methods of the Chapters 3 and 4 were successfully applied both in a Master's thesis [97] as well as in a Bachelor's thesis [98]. Here, a focus, also for future work, is on the control of these spin flips by an external field.

The influence of a time-dependent external field on the reaction dynamics close to the TS in order to control reactions and manipulate reaction rates in a future application will also be the topic of Chapter 5 where a more realistic chemical system is examined – the $\text{LiCN} \rightleftharpoons \text{LiNC}$ isomerization reaction.

5

Isomerization of LiCN

In this section, the methods introduced in Chapters 3 and 4 are applied to the driven $\text{LiCN} \rightleftharpoons \text{LiNC}$ isomerization reaction. After introducing a mathematical description of this system in Sec. 5.1 the following Secs. 5.2 and 5.3 present the results of the non-driven and the driven isomerization reaction, respectively. A main focus is thereby on the effects of the periodic driving on the obtained decay rates. Essential parts of this Chapter have been published in Ref. [99].

5.1 Mathematical description

The three atom molecule LiCN consists of a lithium (Li) atom bound to a carbon (C) and a nitrogen (N) atom, where the latter two form a strongly bound cyanide anion. Being an isomeric molecule, it has two stable conformations, LiCN and LiNC



The Li atom is able to orbit around the cyanide between the two conformations. Its motion can be described semiclassically in Born-Oppenheimer approximation, since analytical approximations to the energy surface [1] and to the dipole surface [2] are known from literature. This section presents how to find mathematical equations of motion for the Li atom orbiting around the cyanide and what assumptions are made therein.

5.1.1 A suitable coordinate system

According to Fig. 5.1 the molecule can be described by a lithium atom (Li) at position \mathbf{r}_{Li} , a carbon atom (C) at position \mathbf{r}_{C} and a nitrogen atom (N) at position \mathbf{r}_{N} . The space-fixed Cartesian coordinate system is chosen such, that all three atoms are located

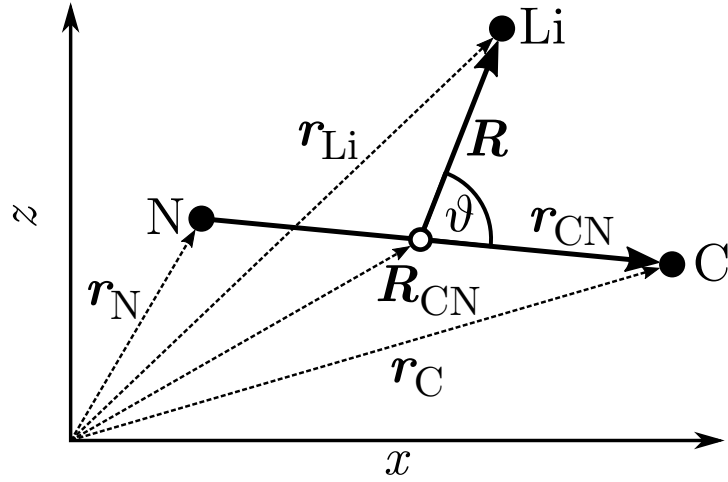


Figure 5.1.: Space-fixed coordinate system to describe the $\text{LiCN} \rightleftharpoons \text{LiNC}$ isomerization reaction. The three atoms lithium (Li), carbon (C) and nitrogen (N) are located at positions \mathbf{r}_{Li} , \mathbf{r}_{C} , and \mathbf{r}_{N} in the (x, z) plane of a globally fixed coordinate system. The vector \mathbf{R} connects the center of mass of the cyanide at position \mathbf{R}_{CN} with the lithium atom, the relative distance between carbon and the nitrogen atom is denoted by \mathbf{r}_{CN} . The angle between \mathbf{R} and \mathbf{r}_{CN} is labeled ϑ .

in the (x, z) -plane. The center of mass of the cyanide at position \mathbf{R}_{CN} is given by

$$\mathbf{R}_{\text{CN}} = \frac{m_{\text{C}} \mathbf{r}_{\text{C}} + m_{\text{N}} \mathbf{r}_{\text{N}}}{M_{\text{CN}}}, \quad (5.2)$$

where $m_{\text{C}} = 12 \text{ u}$ is the mass of ^{12}C , $m_{\text{N}} = 14.003074004(2) \text{ u}$ the mass of ^{14}N and $M_{\text{CN}} = m_{\text{C}} + m_{\text{N}}$ their total mass [100]. The relative distance between the nitrogen and the carbon atom \mathbf{r}_{CN} is given by

$$\mathbf{r}_{\text{CN}} = \mathbf{r}_{\text{C}} - \mathbf{r}_{\text{N}}. \quad (5.3)$$

The oriented distance of the lithium atom to the center of mass of the cyanide is

$$\mathbf{R} = \mathbf{r}_{\text{Li}} - \mathbf{R}_{\text{CN}}, \quad (5.4)$$

and the angle between \mathbf{R} and \mathbf{r}_{CN} is labeled $\vartheta = \angle(\mathbf{R}, \mathbf{r}_{\text{CN}})$. Consequently, the conformation near $\vartheta = 0$ corresponds to LiCN and the conformation near $\vartheta = \pi$ to LiNC.

We assume the initial velocities of the individual atoms to be strictly within the (x, z) -plane. Since the potential energy surface describing the motion of the Li atom relative to the cyanide is a function of $R = |\mathbf{R}|$ and ϑ (see Sec. 5.1.2), the propagation of the LiCN molecule in this model is also strictly in-plane. Even if the movement of the molecule is coupled to an external electric field oriented within this (x, z) -plane, the corresponding dipole surface (see Sec. 5.1.3) does not violate this restriction.

Without further assumptions, the three atoms moving in a plane are described by six independent position variables $\mathbf{r}_{\text{Li}} = (r_{\text{Li}}^{(x)}, r_{\text{Li}}^{(z)})^T$, $\mathbf{r}_{\text{C}} = (r_{\text{C}}^{(x)}, r_{\text{C}}^{(z)})^T$ and $\mathbf{r}_{\text{N}} = (r_{\text{N}}^{(x)}, r_{\text{N}}^{(z)})^T$, and the respective velocities. The Lagrangian \mathcal{L} of the system is given by

$$\mathcal{L} = \frac{1}{2} (m_{\text{Li}} \dot{\mathbf{r}}_{\text{Li}}^2 + m_{\text{C}} \dot{\mathbf{r}}_{\text{C}}^2 + m_{\text{N}} \dot{\mathbf{r}}_{\text{N}}^2) - U(\mathbf{r}_{\text{Li}}, \mathbf{r}_{\text{C}}, \mathbf{r}_{\text{N}}, t) \quad (5.5)$$

with U describing all interactions of the individual atoms and their coupling to a (possibly time-dependent) external field. The mass of the ${}^7\text{Li}$ atom is $m_{\text{Li}} = 7.016\,003\,44(3) \text{ u}$ [100].

The movement of the center of mass \mathbf{R}_{s} of LiCN

$$\mathbf{R}_{\text{s}} = \frac{m_{\text{Li}} \mathbf{r}_{\text{Li}} + m_{\text{C}} \mathbf{r}_{\text{C}} + m_{\text{N}} \mathbf{r}_{\text{N}}}{M} \quad (5.6)$$

can be separated. Here, $M = m_{\text{Li}} + m_{\text{C}} + m_{\text{N}}$ is the total mass of the molecule. Using the coordinate transformations

$$\mathbf{r}_{\text{Li}} = \mathbf{R}_{\text{s}} + \frac{M_{\text{CN}}}{M} \mathbf{R}, \quad (5.7a)$$

$$\mathbf{r}_{\text{C}} = \mathbf{R}_{\text{s}} - \frac{m_{\text{Li}}}{M} \mathbf{R} + \frac{m_{\text{N}}}{M_{\text{CN}}} \mathbf{r}_{\text{CN}}, \quad (5.7b)$$

$$\mathbf{r}_{\text{N}} = \mathbf{R}_{\text{s}} - \frac{m_{\text{Li}}}{M} \mathbf{R} - \frac{m_{\text{C}}}{M_{\text{CN}}} \mathbf{r}_{\text{CN}} \quad (5.7c)$$

together with Eq. (5.5) yields a Lagrangian of the form

$$\mathcal{L} = \frac{1}{2} M \dot{\mathbf{R}}_{\text{s}}^2 + \frac{\mu_1}{2} \dot{\mathbf{R}}^2 + \frac{\mu_2}{2} \dot{\mathbf{r}}_{\text{CN}}^2 - U(\mathbf{R}, \mathbf{r}_{\text{CN}}, t). \quad (5.8)$$

Here, $\mu_1 = (1/m_{\text{Li}} + 1/M_{\text{CN}})^{-1}$ is the LiCN reduced mass and $\mu_2 = (1/m_{\text{C}} + 1/m_{\text{N}})^{-1}$ is the cyanide reduced mass. Within the frame of the Lagrangian (5.8) the center of mass movement is separated.

So far, the molecule was described in the spatially fixed Cartesian coordinate system (x, z) . Now, this system is switched to a new one (x', z') attached to the center of mass between the carbon and the nitrogen atom with the z' -axis being in direction of the molecule's \mathbf{R} -vector (see Fig. 5.2). In this *body-fixed reference frame* [101], analytic expressions for both the energy surface and for the dipole surface are known from literature [1, 2]. The meaning of \mathbf{R} , \mathbf{r}_{CN} , and ϑ is still the same as in the space-fixed coordinate system of Fig. 5.1, but there is an additional angle $\alpha = \angle(\hat{\mathbf{e}}_z, \mathbf{R})$ introduced to describe the total rotation of the molecule within the (x, z) -plane. Here, $\hat{\mathbf{e}}_z$ is the unit vector in z -direction of the space-fixed coordinate system.

Assuming that the vibrations of the cyanide anion have a very high frequency as the bond between carbon and nitrogen is very stiff, $|\mathbf{r}_{\text{CN}}|$ is replaced by the equilibrium cyanide bond length $r_e = 2.186 a_0$ [101, 102] with a_0 being Bohr's radius [61]. Consequently, the representation of the two vectors \mathbf{R} and \mathbf{r}_{CN} can be obtained

$$\mathbf{R} = |\mathbf{R}| \hat{\mathbf{e}}_{\mathbf{R}} = R (\sin(\alpha), \cos(\alpha))^T, \quad (5.9a)$$

$$\mathbf{r}_{\text{CN}} = |\mathbf{r}_{\text{CN}}| \hat{\mathbf{e}}_{\mathbf{r}_{\text{CN}}} = r_e (\sin(\alpha + \vartheta), \cos(\alpha + \vartheta))^T, \quad (5.9b)$$

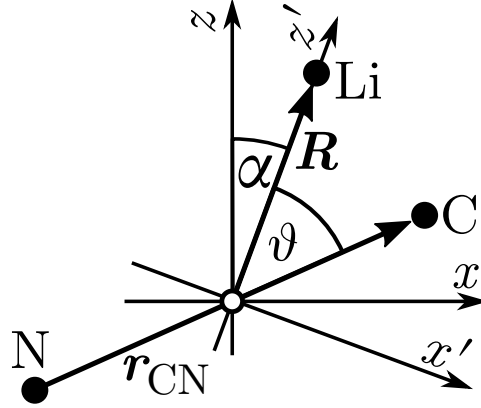


Figure 5.2.: Body-fixed coordinate system (x', z') attached to the center of mass of the cyanide with the z' -axis being in direction of the molecule's \mathbf{R} -vector. The meaning of \mathbf{R} , r_{CN} , and ϑ is still the same as in the space-fixed reference frame with directions (x, z) explained in Fig. 5.1. However, now an additional angle α is introduced between the z -axis of the space-fixed coordinate system and the vector \mathbf{R} (and therefore the z' -direction) to consider possible rotations of the LiCN molecule within the (x, z) -plane.

including the rotation angle α of the body-fixed coordinate system of Fig. 5.2. The respective velocities $\dot{\mathbf{R}}$ and $\dot{\mathbf{r}}_{\text{CN}}$ yield

$$\dot{\mathbf{R}} = R \dot{\alpha} (\cos(\alpha), -\sin(\alpha))^{\text{T}} + \dot{R} (\sin(\alpha), \cos(\alpha))^{\text{T}}, \quad (5.10a)$$

$$\dot{\mathbf{r}}_{\text{CN}} = r_e (\dot{\alpha} + \dot{\vartheta}) (\cos(\alpha + \vartheta), -\sin(\alpha + \vartheta))^{\text{T}}. \quad (5.10b)$$

Using the relations $\dot{\mathbf{R}}^2 = R^2 \dot{\alpha}^2 + \dot{R}^2$ and $\dot{\mathbf{r}}_{\text{CN}}^2 = r_e^2 (\dot{\alpha} + \dot{\vartheta})^2$ on the Lagrangian (5.8) yields its representation in the body-fixed reference frame

$$\mathcal{L} = \frac{1}{2} M \dot{\mathbf{R}}_s^2 + \frac{\mu_1}{2} (R^2 \dot{\alpha}^2 + \dot{R}^2) + \frac{\mu_2}{2} r_e^2 (\dot{\alpha} + \dot{\vartheta})^2 - U(\alpha, R, \vartheta, t). \quad (5.11)$$

With Hamilton's formalism and assuming a fixed bond length r_e , the generalized momenta of the system can be obtained

$$\mathbf{p}_{\mathbf{R}_s} = \frac{\partial \mathcal{L}}{\partial \dot{\mathbf{R}}_s} = M \dot{\mathbf{R}}_s, \quad (5.12a)$$

$$p_R = \frac{\partial \mathcal{L}}{\partial \dot{R}} = \mu_1 \dot{R}, \quad (5.12b)$$

$$p_{\vartheta} = \frac{\partial \mathcal{L}}{\partial \dot{\vartheta}} = \mu_2 r_e^2 (\dot{\alpha} + \dot{\vartheta}), \quad (5.12c)$$

$$p_{\alpha} = \frac{\partial \mathcal{L}}{\partial \dot{\alpha}} = \mu_1 R^2 \dot{\alpha} + \mu_2 r_e^2 (\dot{\alpha} + \dot{\vartheta}), \quad (5.12d)$$

to construct the complete Hamiltonian of LiCN

$$\begin{aligned}
 \mathcal{H} &= \mathcal{H}_{\text{com}} + \mathcal{H}_{\text{rot}} + \mathcal{H}_{\text{rel}} , \\
 \mathcal{H}_{\text{com}} &= \frac{\mathbf{p}_{\mathbf{R}_s}^2}{2M} , \\
 \mathcal{H}_{\text{rot}} &= \frac{1}{\mu_1 R^2} \left(\frac{p_\alpha^2}{2} - p_\alpha p_\vartheta \right) , \\
 \mathcal{H}_{\text{rel}} &= \frac{p_R^2}{2\mu_1} + \frac{1}{2} \left(\frac{1}{\mu_1 R^2} + \frac{1}{\mu_2 r_e^2} \right) p_\vartheta^2 + U(\alpha, R, \vartheta, t) .
 \end{aligned} \tag{5.13}$$

Here, \mathcal{H}_{com} is the Hamiltonian for the center of mass movement, \mathcal{H}_{rot} describes the overall rotation of the molecule and \mathcal{H}_{rel} the movement of the individual atoms relative to each other. Without further assumptions, Hamiltonian (5.13) describes the movement of three atoms in a planar space, yielding five degrees of freedom in the system, as the carbon atom and the nitrogen atom are coupled at a fixed distance r_e .

Since the external driving $U(\alpha, R, \vartheta, t)$ only depends on the orientation of the molecule, internal degrees of freedom and time, but not on the molecule's absolute position in space, the center of mass movement separates and can be neglected in further treatment. This effectively reduces the degrees of freedom of the LiCN model by two to a three-dimensional position space (α, R, ϑ) or a seven-dimensional extended phase space including the associated momenta and time.

Under special circumstances, additional assumptions can be made to further reduce the dimensionality of the system. Therefore, the potential $U(\alpha, R, \vartheta, t)$ is examined in the next two subsections 5.1.2 and 5.1.3.

5.1.2 Potential energy surface in the absence of external fields

In the absence of external fields, the potential energy surface U_{pes} of the molecule

$$U(\alpha, R, \vartheta, t) = U_{\text{pes}}(R, \vartheta) \tag{5.14}$$

is independent of its overall orientation, as the intrinsic energy of the molecule is the same for any orientation α . Hence, the potential energy surface depends only on R and ϑ , the intrinsic degrees of freedom.

Early calculations to obtain the potential energy surface of the LiCN molecule were done in 1973 by Clementi et al. using Hartree-Fock based methods [103]. In this early stage of research, individual points on the energy surface of LiCN were obtained, but their analytic connection was a challenging task [104]. In 1982 Essers et al. solved this problem performing a set of ab initio self-consistent field (SCF) calculations. As a result, they provided a fully analytical function accurately fitting the region of interest of the LiCN potential energy surface for performing nuclear-motion calculations [1].

According to Ref. [1], the bond between the Li atom and the cyanide in LiCN is highly ionic since the cyanide has a very large electron affinity (experimental value:

$\chi = 3.82$ [105]), and the ionization potential of the Li atom is small. Consequently, the bond of LiCN is dominated by Coulomb forces and in a good approximation the molecule may be thought to consist of two closed-shell ions. Ref. [1] gives an example for the dipole moment of these shells: at a distance of $4.8 a_0$ between the lithium atom and the center of mass of the cyanide in a triangular structure 84.7% of the SCF dipole moment arises from the separation of charge. The polarization of the CN^- anion contributes with 14.4%, and the polarization of the Li^+ ion with only 0.1% to the total dipole moment. The remaining 0.8% are due to exchange and penetration effects. See Sec. 5.1.3 for a more detailed discussion on the dipole moment of LiCN.

According to Ref. [1] the self-consistent field (SCF) interaction energy between the two closed-shell ions Li^+ and CN^- is split up into two parts, a long-range part corresponding to electrostatic and induction energy of classical electrostatic theory and a short-range part arising from exchange and penetration effects.

In terms of Legendre polynomials $P_L(\cos(\vartheta))$ of order L [106], the classical electrostatic energy of the long-range part is given by the expression [102]

$$U_{\text{el}}(R, \vartheta) = \sum_{L=0}^{\infty} R^{-L-1} P_L(\cos(\vartheta)) \langle Q_{L,0} \rangle \quad (5.15)$$

for the body-fixed reference frame defined in Fig. 5.2 (remember, that the overall orientation α of the molecule can be neglected in the absence of external fields). In Eq. (5.15), $\langle Q_{L,0} \rangle$ is the expectation value of the multipole moment of order L of the CN^- ion. Up to $L = 6$, the values of these multipole moments have been obtained in Ref. [102] and are also listed in Table A.1 in Appendix A.

A formula for the classical induction energy of the long-range part can be found e. g. in Ref. [1]

$$U_{\text{ind}}(R, \vartheta) = \sum_{l_1, l_2=0}^{\infty} R^{-l_1-l_2-2} \sum_{L=|l_1-l_2|}^{l_1+l_2} P_L(\cos(\vartheta)) C_{l_1, l_2, L}, \quad (5.16)$$

again for the coordinates (R, ϑ) of the body-fixed reference frame. Analytic expressions for the induction coefficients $C_{l_1, l_2, L}$ are given in Ref. [1] together with their numerical values up to $l_1 = l_2 = 3$ and $L = 6$. The latter can also be found in Table A.2 in Appendix A.

A theory for the short range energy, which describes the exchange and penetration effects of the two closed-shell ions based on the properties of the individual shells is hard to find, as for shorter distances these shells cease to be identifiable. In Ref. [102], this problem is solved by fitting a function of the form

$$U_{\text{sr}}(R, \vartheta) = \sum_{L=0}^{\infty} D_L(R) P_L(\cos(\vartheta)), \quad (5.17)$$

with the short-range parameters $D_L(R)$ to take into account the difference between the SCF calculations and the long-range interaction part. In principle, this expansion is ex-

act, since the Legendre polynomials $P_L(\cos(\vartheta))$ are complete on the interval $[-1, 1]$ [107]. The short-range parameters $D_L(R)$ were obtained according to Refs. [102, 108] via Gauss-Legendre quadrature at several individual points, where the series (5.17) converges after $L = 6$. The various results are fitted by the analytic form

$$D_L(R) = \exp(-A_L - B_L R - C_L R^2) . \quad (5.18)$$

The fit parameters A_L , B_L and C_L were obtained for $L \in (0, 9)$ in Ref. [1] and can also be found in Table A.3 in Appendix A.

Reference [1] gives a formula for the total SCF potential energy surface of the LiCN molecule

$$U_{\text{pes}}(R, \vartheta) = [U_{\text{el}}(R, \vartheta) + U_{\text{ind}}(R, \vartheta)] F(R) + U_{\text{sr}}(R, \vartheta) , \quad (5.19)$$

with $F(R)$ being an isotropic damping function represented by the Gaussian form

$$F(R) = 1 - \exp(-a(R - R_0)^2) . \quad (5.20)$$

According to Ref. [1], optimal values for the parameters in this damping function are $a = 1.5156 a_0^{-2}$ and $R_0 = 1.9008 a_0$.

Described in the intrinsic coordinates R and ϑ of the body-fixed reference frame of Fig. 5.2, the potential energy surface U_{pes} of the LiCN molecule according to Eq. (5.19) is very flat in the angular coordinate ϑ , see Fig. 5.3. Thus, the Li atom can orbit around the cyanide. There are two local minima on this energy surface corresponding to the linear structures LiCN ($\vartheta = 0$) and LiNC ($\vartheta = \pi$) [1]. In between these two minima a rank-1 saddle represents the bottleneck of the isomerization reaction, visualized by the equipotential lines in Fig. 5.3.

Using the analytical expression (5.19) for $U_{\text{pes}}(R, \vartheta)$, the Lagrangian (5.11) for the LiCN \rightleftharpoons LiNC isomerization reaction in the absence of external fields changes to

$$\mathcal{L} = \frac{1}{2} M \dot{\mathbf{R}}_s^2 + \frac{\mu_1}{2} \left(R^2 \dot{\alpha}^2 + \dot{R}^2 \right) + \frac{\mu_2}{2} r_e^2 \left(\dot{\alpha} + \dot{\vartheta} \right)^2 - U_{\text{pes}}(R, \vartheta) . \quad (5.21)$$

Now, $\partial \mathcal{L} / \partial \alpha = 0$ and therefore $p_\alpha = \partial \mathcal{L} / \partial \dot{\alpha}$ is conserved. Choosing appropriate initial conditions with $p_\alpha = 0$ (non-rotating molecules) simplifies the full Hamiltonian (5.13) to the *classical rotationless two degrees of freedom Hamiltonian*

$$\mathcal{H} = \frac{p_R^2}{2\mu_1} + \frac{1}{2} \left(\frac{1}{\mu_1 R^2} + \frac{1}{\mu_2 r_e^2} \right) p_\vartheta^2 + U_{\text{pes}}(R, \vartheta) , \quad (5.22)$$

which can also be found in the literature, e. g. in Refs. [109, 110]. Using Hamilton's

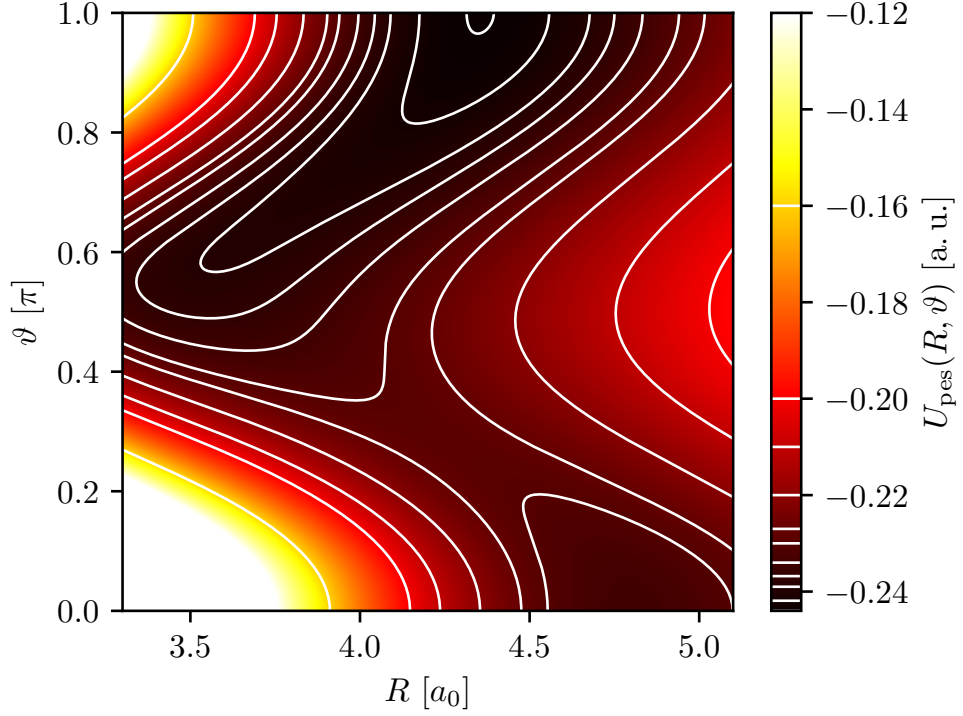


Figure 5.3.: Potential energy surface $U_{\text{pes}}(R, \vartheta)$ of the LiCN molecule according to Eq. (5.19), given in terms of the intrinsic coordinates R and ϑ of the body-fixed reference frame of Fig. 5.2. Due to the absence of external fields, the potential energy surface describes the interaction of the individual atoms and does not depend on the overall orientation α of the molecule. Along the angular coordinate ϑ the potential energy surface is very flat, allowing the Li atom to orbit around the cyanide between the two (meta)-stable structures LiCN (near $\vartheta = 0$) and LiNC (near $\vartheta = \pi$).

formalism, the equations of motion can be derived

$$\frac{\partial \mathcal{H}}{\partial p_\vartheta} = \left(\frac{1}{\mu_1 R^2} + \frac{1}{\mu_2 r_e^2} \right) p_\vartheta = \dot{\vartheta} , \quad (5.23a)$$

$$-\frac{\partial \mathcal{H}}{\partial \vartheta} = -\frac{dU_{\text{pes}}(R, \vartheta)}{d\vartheta} = \dot{p}_\vartheta , \quad (5.23b)$$

$$\frac{\partial \mathcal{H}}{\partial p_R} = \frac{p_R}{\mu_1} = \dot{R} , \quad (5.23c)$$

$$-\frac{\partial \mathcal{H}}{\partial R} = \frac{p_\vartheta^2}{\mu_1 R^3} - \frac{dU_{\text{pes}}(R, \vartheta)}{dR} = \dot{p}_R . \quad (5.23d)$$

All in all, the dynamics of the LiCN \rightleftharpoons LiNC isomerization reaction in the absence of external fields can be obtained numerically for the state $\zeta(t) = (\vartheta, p_\vartheta, R, p_R)^T$ by solving

a first order differential equation of the form

$$\dot{\zeta}(t) = \begin{pmatrix} \dot{\vartheta} \\ \dot{p}_\vartheta \\ \dot{R} \\ \dot{p}_R \end{pmatrix} = \begin{pmatrix} \left(\frac{1}{\mu_1 R^2} + \frac{1}{\mu_2 r_e^2} \right) p_\vartheta \\ -\frac{dU_{\text{pes}}(R, \vartheta)}{d\vartheta} \\ \frac{p_R}{\mu_1} \\ \frac{p_\vartheta^2}{\mu_1 R^3} - \frac{dU_{\text{pes}}(R, \vartheta)}{dR} \end{pmatrix}. \quad (5.24)$$

In the present work, this is done by a fourth order Runge-Kutta algorithm [111]. Therefore, the first derivatives of U_{pes} with respect to R and ϑ have been implemented in C++ using the Legendre polynomials and their derivatives given in Appendix A.

5.1.3 Coupling to a time-periodically driven external field

An electric dipole with dipole moment $\boldsymbol{\mu}$ exposed to a time-dependent external electric field $\boldsymbol{E}(t)$ results in a potential energy [112]

$$U_{\text{dip}}(t) = -\boldsymbol{\mu} \cdot \boldsymbol{E}(t). \quad (5.25)$$

To be able to perform nuclear-motion calculations for the $\text{LiCN} \rightleftharpoons \text{LiNC}$ isomerization reaction not only the potential energy surface but also a continuous representation of the molecule's dipole moment $\boldsymbol{\mu}$, the *dipole surface*, is needed, e. g. if the movement of the molecule should be coupled to an external (possibly time-dependent) electric field, like in Eq. (5.25). Individual points on the dipole surface have been obtained using SCF methods by Essers, Tennyson and Wormer in 1982 [1], but a continuous connection of these individual points was a challenging task.

Motivated by the success of Wormer and co-workers in representing the SCF potential energy surface in terms of analytic long- and short-range expressions for the interactions between two closed-shell ions [1, 102] (see discussion in Sec. 5.1.2), Brocks, Tennyson and van der Avoird were able to provide analytical expressions for the dipole moment of LiCN in 1984 [2]. The following paragraphs sum up their findings and give a brief overview on the methods used and the assumptions made.

A body-fixed reference system according to Fig. 5.2 is used to describe the movement of the LiCN molecule within the (x, z) -plane. As long as an external electric field is oriented within this plane, there is no force driving the molecule out of plane. Hence its dipole moment $\boldsymbol{\mu} = (\mu^{(x')}, \mu^{(z')})$ is also oriented in-plane with the two components oriented along the x' - and z' -axis of the body-fixed reference frame and $\mu^{(y')} = 0$.

The analytic expression for the dipole moment according to Ref. [2] can be split into three parts

$$\boldsymbol{\mu}(R, \vartheta) = \boldsymbol{\mu}_{\text{lr}}(R, \vartheta) + \boldsymbol{\mu}_{\text{ind}}(R, \vartheta) + \boldsymbol{\mu}_{\text{sr}}(R, \vartheta). \quad (5.26)$$

Here, the term $\boldsymbol{\mu}_{\text{lr}}$ is the first order long-range contribution to the dipole moment due to the separation of charge of Li^+ and CN^- . For large R , this separation of charged

ions becomes the main contribution to the dipole moment $\boldsymbol{\mu}$ together with a smaller contribution due to the permanent dipole moment of the CN^- ion $|\boldsymbol{\mu}_{\text{CN}}| = \mu_{\text{CN}} = 0.2151e a_0$ [102], with $e = 1.602\,176\,621 \times 10^{-19}$ C being the elementary charge [61]. Both effects accumulate to the first order long-range contribution $\boldsymbol{\mu}_{\text{lr}}(R, \vartheta)$ of Eq. (5.26) [2]

$$\mu_{\text{lr}}^{(x')}(R, \vartheta) = \mu_{\text{CN}} \sin(\vartheta) , \quad (5.27a)$$

$$\mu_{\text{lr}}^{(z')}(R, \vartheta) = e R + \mu_{\text{CN}} \cos(\vartheta) . \quad (5.27b)$$

The leading second order long-range contribution $\boldsymbol{\mu}_{\text{ind}}$ to the total dipole moment $\boldsymbol{\mu}$ in Eq. (5.26) is caused by induction [1, 2, 102]. However, since the resulting fits in Ref. [2] could not be improved including charge induced dipole contributions, these terms are being omitted in the final results of this reference. Hence, $\boldsymbol{\mu}_{\text{ind}} = \mathbf{0}$ in Eq. (5.26).

The third term $\boldsymbol{\mu}_{\text{sr}}$ is the short-range contribution to the dipole moment. It is defined by $\boldsymbol{\mu}_{\text{sr}} = \boldsymbol{\mu} - \boldsymbol{\mu}_{\text{lr}}$, i. e., the difference between the dipole moments calculated via SCF methods and the analytically known long-range contributions. In doing so, possible truncation errors in $\boldsymbol{\mu}_{\text{lr}}$ are taken into account.

As already explained in Sec. 5.1.2, charge penetration and exchange effects are dominant in the short-range regime due to the overlap of the Li^+ and CN^- charge distributions. Here, a theoretical description with two individual closed-shell ions fails, as these shells cease to be identifiable. However, this fact motivates an exponential dependence on R in the fit-function for the short-range part $\boldsymbol{\mu}_{\text{sr}}$ of the total dipole moment $\boldsymbol{\mu}$ in Eq. (5.26) [2]

$$\mu_{\text{sr}}^{(x')}(R, \vartheta) = \sum_{\lambda=1}^2 a_{\lambda,1} \exp\left(\sum_{n=1}^2 b_{n,\lambda,1} R^n\right) P_{\lambda}^1(\cos(\vartheta)) , \quad (5.28a)$$

$$\mu_{\text{sr}}^{(z')}(R, \vartheta) = \sum_{\lambda=0}^3 a_{\lambda,0} \exp\left(\sum_{n=1}^2 b_{n,\lambda,0} R^n\right) P_{\lambda}(\cos(\vartheta)) . \quad (5.28b)$$

Here, $P_{\lambda}(\cos(\vartheta))$ are the Legendre polynomials and $P_{\lambda}^1(\cos(\vartheta))$ their first derivatives, respectively. The coefficients $a_{\lambda,\nu}$ and $b_{n,\lambda,\nu}$ with $\nu = 1, 2$ were fitted such, that the average deviation of the total dipole $\mu^{(x')}$ in (x') -direction compared to the corresponding SCF data is 35 % and the average deviation of the total dipole $\mu^{(z')}$ in (z') -direction compared to the corresponding SCF data is 0.32 % for $R \in [3.3a_0, 5a_0]$. Here, $\mu^{(z')}$ dominates the total dipole moment being at least 15 times larger than $\mu^{(x')}$, so the large relative error in the fit of $\mu^{(x')}$ has little meaning. All coefficients can be found in Ref. [2], but according to Ref. [113] there is a typo as the coefficients $a_{1,0}$ and $a_{3,0}$ given in Table II of Ref. [2] should be negatively signed. The corrected coefficients are also listed in Table A.4 in Appendix A. A contour plot according to Eq. (5.26) of the dipole surface of $\mu^{(x')}(R, \vartheta)$ is given in Fig. 5.4 and for the dipole surface of $\mu^{(z')}(R, \vartheta)$ in Fig. 5.5.

The $\text{LiCN} \rightleftharpoons \text{LiNC}$ isomerization reaction becomes a time-dependent problem, if the reaction is subject to a time-dependent electric field. In general, such an external field

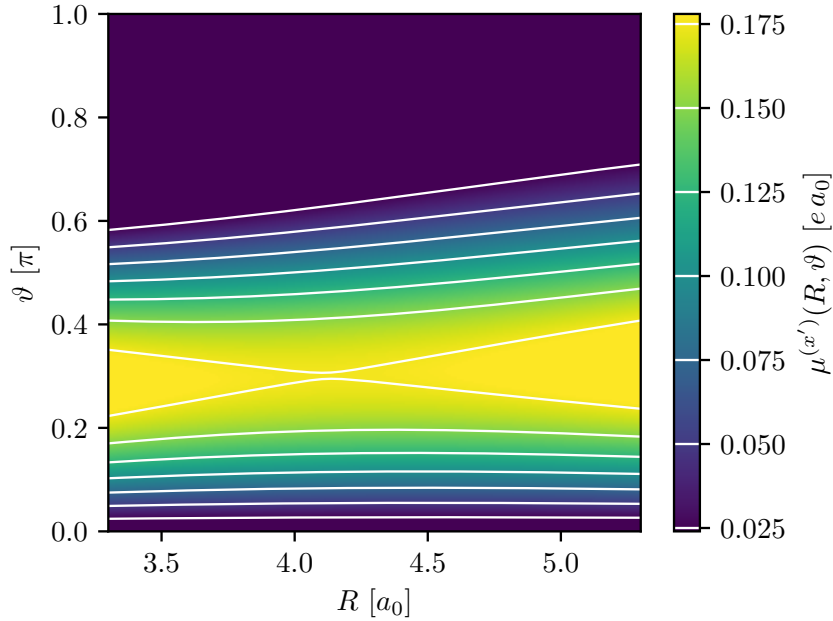


Figure 5.4.: Dipole surface $\mu^{(x')}(R, \vartheta)$ for LiCN according to Eq. (5.26). Note the difference to Fig. 2 in Ref. [2] wherein the LiNC dipole surface is given, not the LiCN surface. This accounts for a reflection and a minus compared to the present figure.

with a given direction in a space-fixed coordinate system breaks the rotational symmetry of Eq. (5.22) as the potential energy of a dipole depends on its angle relative to an electric field, see Eq. (5.25). Consequently, the overall orientation α of the molecule becomes relevant when describing the time-dependent LiCN isomerization reaction. Whereas the undisturbed reaction according to Sec. 5.1.2 can be described adequately in a two-dimensional parameter space (R, ϑ) , the time-dependent problem exposed to a periodically oscillating external field with a fixed direction in the space-fixed coordinate system (Fig. 5.1) has to be treated in the extended parameter space $(R, \vartheta, \alpha, t)$ including the absolute orientation α of the molecule – at least without further assumptions.

The dipole moment in the space-fixed coordinate system, which is needed in Eq. (5.25), is obtained by rotating its body-fixed contribution by the angle α

$$\boldsymbol{\mu}(R, \vartheta, \alpha) = \begin{pmatrix} \cos(\alpha) & \sin(\alpha) \\ -\sin(\alpha) & \cos(\alpha) \end{pmatrix} \begin{pmatrix} \mu^{(x')}(R, \vartheta) \\ \mu^{(z')}(R, \vartheta) \end{pmatrix}. \quad (5.29)$$

As discussed, the dipole $\mu^{(z')}$ in z' -direction of the body-fixed coordinate system is at least 15 times larger than the dipole moment $\mu^{(x')}$ in x' -direction. Thus, $\mu^{(z')}$ is by far the largest contribution to the molecule's dipole moment. When ignoring the much smaller component $\mu^{(x')}(R, \vartheta)$, the dipole potential of Eq. (5.25) simplifies to

$$U_{\text{dip}}(R, \vartheta, \alpha, t) \approx -E_0 \sin(\omega t) \mu^{(z')}(R, \vartheta) \cos(\alpha). \quad (5.30)$$

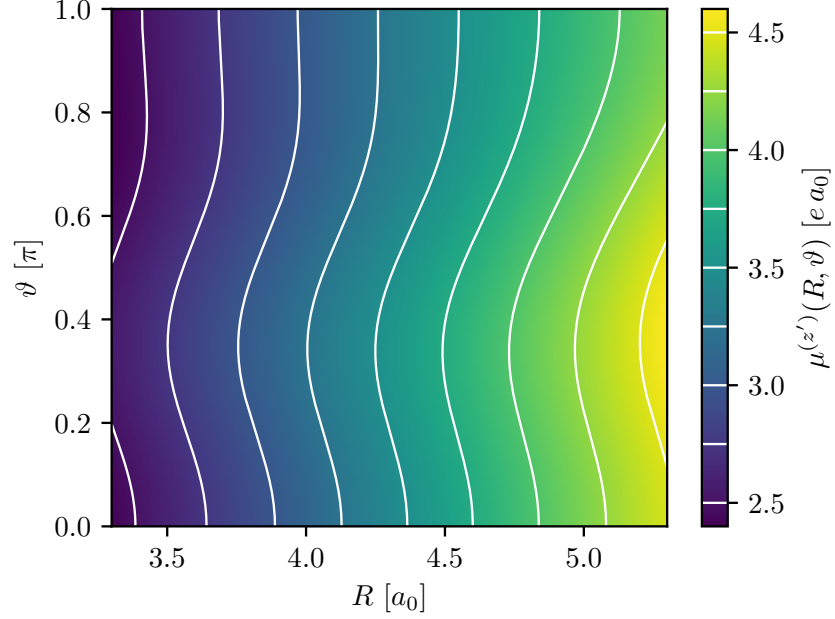


Figure 5.5.: Dipole surface $\mu^{(z')}(R, \vartheta)$ for LiCN according to Eq. (5.26). Note the difference to Fig. 2 in Ref. [2] wherein the LiNC dipole surface is given, not the LiCN surface. This accounts for an inversion of the ϑ -axis in the present figure.

By further neglecting the oscillations in α around the minimum at $\alpha = 0$, hence, for $\cos(\alpha) \approx 1$, the dimensionality of the time-dependent LiCN isomerization reaction can be reduced. Now, the simplified dipole potential

$$U_{\text{dip}}(R, \vartheta, t) = -E_0 \sin(\omega t) \mu^{(z')}(R, \vartheta) \quad (5.31)$$

will only depend on the two internal degrees of freedom, R and ϑ , and on time t .

The simplification according to Eq. (5.31) will be valid if the oscillations in α are much faster than the other motion and, thus, the external field is taken into account as an effective field which considers the various orientations α by renormalizing the prefactor E_0 . To fully examine the validity of this simplification and to consider the LiCN isomerization in a higher-dimensional and α dependent case will remain for future work. Here, we resort to the simplified problem to qualitatively study the influence of a time-periodically driven oscillating field. Thus, we focus on the reduced-dimensional Hamiltonian

$$\mathcal{H}_{\text{driven}}(R, \vartheta, t) = \mathcal{H} + U_{\text{dip}}(R, \vartheta, t) , \quad (5.32)$$

where \mathcal{H} is the non-driven Hamiltonian of Eq. (5.22) and the time-dependent driving is included via the simplified dipole potential according to Eq. (5.31).

Using Hamilton's formalism, the equations of motion can be derived. They have again the form of a first order differential equation for the state $\zeta(t) = (\vartheta, p_\vartheta, R, p_R)^T$, similar

to the field-free equation (5.24) in Sec. 5.1.2. However, now time-dependent derivatives of the dipole potential $U_{\text{dip}}(R, \vartheta, t)$ according to Eq. (5.31) are included

$$\dot{\zeta}(t) = \begin{pmatrix} \dot{\vartheta} \\ \dot{p}_{\vartheta} \\ \dot{R} \\ \dot{p}_R \end{pmatrix} = \begin{pmatrix} \left(\frac{1}{\mu_1 R^2} + \frac{1}{\mu_2 r_e^2} \right) p_{\vartheta} \\ -\frac{dU_{\text{pes}}(R, \vartheta)}{d\vartheta} - \frac{dU_{\text{dip}}(R, \vartheta, t)}{d\vartheta} \\ \frac{p_R}{\mu_1} \\ \frac{p_{\vartheta}^2}{\mu_1 R^3} - \frac{dU_{\text{pes}}(R, \vartheta)}{dR} - \frac{dU_{\text{dip}}(R, \vartheta, t)}{dR} \end{pmatrix}. \quad (5.33)$$

In the present work, solutions are found numerically using a fourth order Runge-Kutta algorithm [111]. Therefore, the derivatives of U_{pes} and U_{dip} with respect to R and ϑ have been implemented in C++ using the Legendre polynomials and their derivatives, see Appendix A.

5.2 Non-driven LiCN isomerization reaction

In the absence of external fields, the potential energy surface according to Eq. (5.19) describes the interaction between the individual atoms. According to Fig. 5.6, the metastable structure LiCN close to $\vartheta = 0$ is named *reactant* \mathcal{R} and the stable structure LiNC close to $\vartheta = \pi$ is called *product* \mathcal{P} . Both (meta)-stable states are separated by an energy barrier with a saddle point at position $R = 4.263$ and $\vartheta = 0.280\pi$. In Fig. 5.6, this saddle point is found by numerically searching for the root in the gradient of the potential energy surface $U_{\text{pes}}(R, \vartheta)$ according to Eq. (5.19).

5.2.1 Analysis of reactive trajectories

The relative movement of the individual atoms in the $\text{LiCN} \rightleftharpoons \text{LiNC}$ isomerization reaction is described by the EOM according to Eq. (5.24). In Fig. 5.6, two exemplary trajectories are shown. The reactive trajectory in Fig. 5.6 (a) is initialized in the reactant state \mathcal{R} . Described by the relative coordinates R and ϑ , it enters the barrier region, i. e., the vicinity of the saddle point. Having enough energy to overcome the barrier the molecule reacts to the product state \mathcal{P} . Conversely, the non-reactive trajectory in Fig. 5.6 (b), initialized in the product state, does not cross the barrier, as the energy of the molecule is too small.

When comparing the trajectories in Fig. 5.6, it is remarkable, that both of them are starting to oscillate in the stable direction of the barrier, whereas the movement in the unstable direction slows down as trajectories are approaching the area close to the saddle point. This is a first indicator that a stable (and an unstable) manifold can be found in the barrier region. A more detailed analysis has to be done in the phase space.

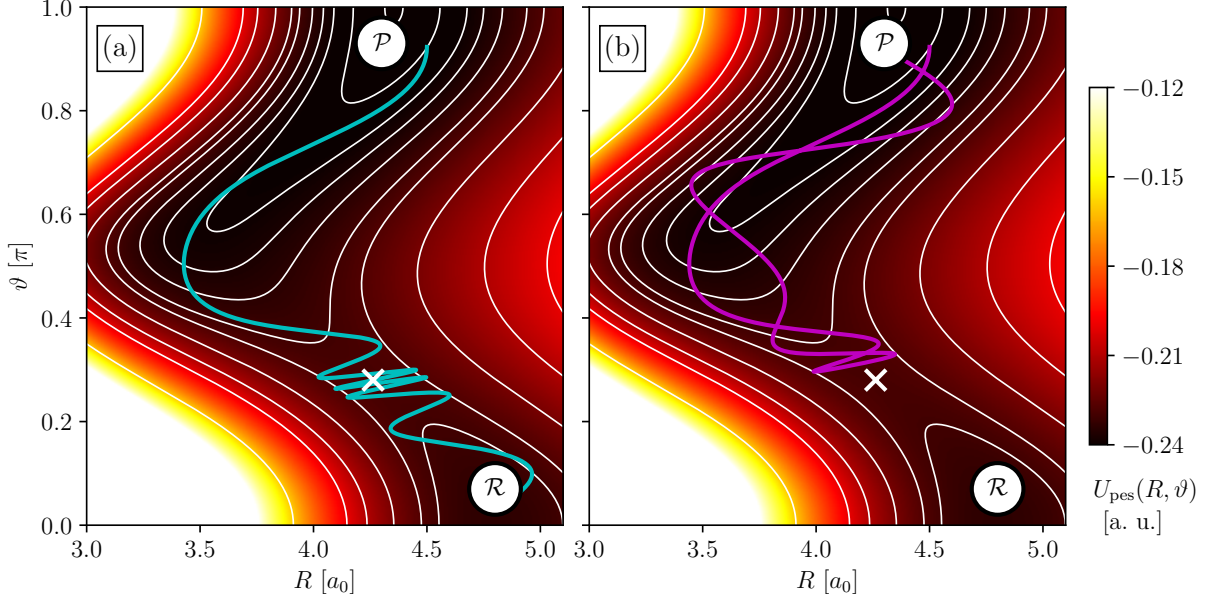


Figure 5.6.: Color encoding: potential energy surface $U_{\text{pes}}(R, \vartheta)$ according to Eq. (5.19) of the static LiCN isomerization reaction, with the two (meta)-stable states LiCN close to $\vartheta = 0$, named *reactant* \mathcal{R} and LiNC close to $\vartheta = \pi$, denoted as *product* \mathcal{P} . The white cross marks the saddle point at position $R = 4.262615$ and $\vartheta = 0.280033\pi$ on the barrier between the two (meta)-stable minima. This point was found numerically by searching for the root in the gradient of the static LiCN potential (5.19). The reactive trajectory in part (a) crosses the rank-1 saddle after staying in the barrier region for several oscillations. The non-reactive trajectory in part (b) starts and ends in the product state.

According to Sec. 3.3, there exist several methods to reveal phase space structures. In Fig. 5.7 (a) the TD is shown in the (ϑ, p_ϑ) -plane for $R = 4.3$ and $p_R = 0$. Here, all trajectories entering the phase space area with $\vartheta < 0.15\pi$ are classified as reactant and all trajectories entering $\vartheta > 0.5\pi$ are denoted as product. Obviously, the TD shows the clear and pronounced cross-like fibers of the stable and the unstable manifold, intersecting on the NHIM of the barrier. As a verification, Fig. 5.7 (b) shows the same cross section of the phase space, but this time with reactive and non-reactive areas as a color encoding. Again, the cross-like structure of the two manifolds is visible, when choosing the same cutoffs as in Fig. 5.7 (a), and the reactive and non-reactive areas are clearly separated.

To demonstrate the influence of choosing proper cutoffs, the same calculations as in Fig. 5.7 are repeated in Fig. 5.8. However, this time, the cutoffs are enlarged to cover the full area in between $\vartheta \in [0, \pi]$. Hence, to be classified as reactant, a trajectory has to leave to $\vartheta < 0$ and to be denoted as product, it has to enter $\vartheta > 0$. By choosing larger cutoffs, more substructure is encoded in the TD of Fig. 5.8 (a). Although the fibers of the stable and the unstable manifold are still visible, they are overlapped by

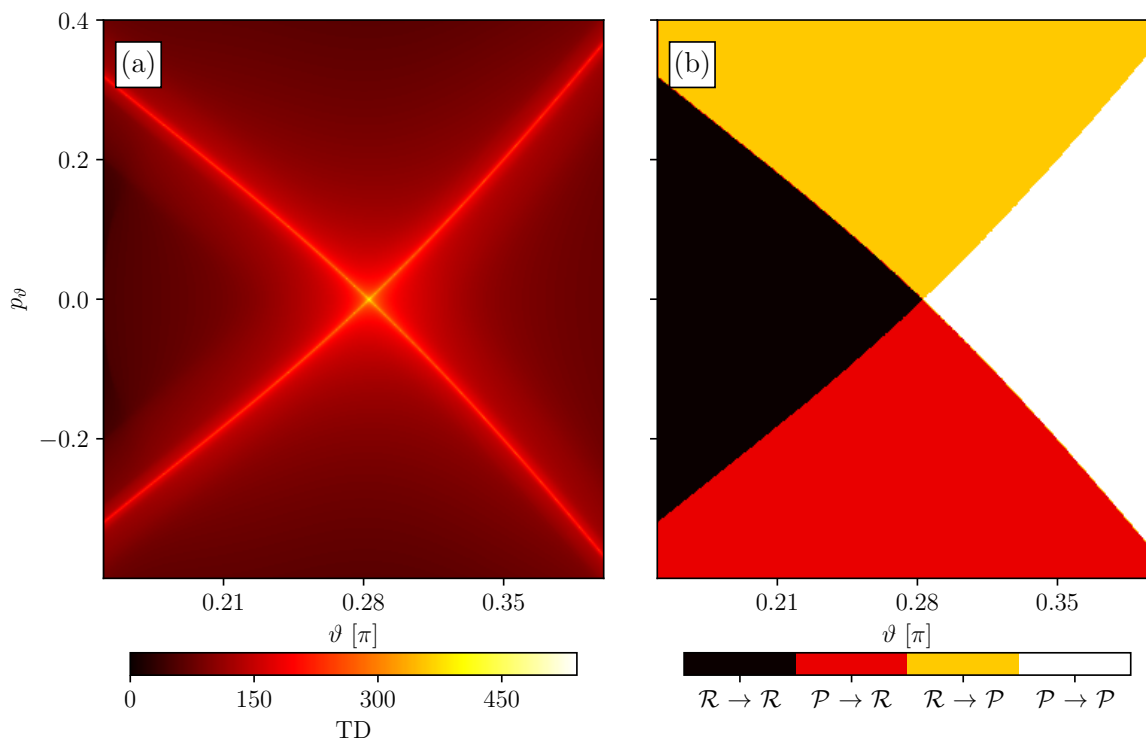


Figure 5.7.: Phase-space sections (ϑ, p_ϑ) of the undisturbed LiCN problem with $R = 4.3$ and $p_R = 0$. (a): Plot of the TD with cutoffs at $\vartheta = 0.15\pi$ and 0.5π . Fibers of the stable and unstable manifold, which intersect in a point on the NHIM, are clearly visible as maximum structures. (b): Corresponding plot of the various reaction states according to Sec. 3.3.

additional structures forming multiple crosses. The related cross section of the reactive and non-reactive areas in Fig. 5.8 (b) is slightly more clear here, as it shows a single, dominant cross. Still, the four areas are not fully separated any more and begin to mix.

An explanation for these emerging substructures when choosing the wrong cutoffs can be found by closely looking at the potential energy surface in, e. g., Fig. 5.6. At values $\vartheta > 0.5$ the path of minimum energy changes its direction significantly. Hence, trajectories “falling down” the barrier to the product side may be reflected at the potential if the upper cutoff in ϑ is chosen much larger. These reflected trajectories can re-enter the barrier region and cross the saddle again. However, such global re-crossings are unwanted in TST as they would lead to an overestimation of the related decay rates. This problem was extensively discussed in Ref. [55] and a solution is to choose the cutoffs small enough that the barrier’s property of being locally recrossing-free is maintained.

The connection between individual reactive and non-reactive trajectories and a cross section with reactive and non-reactive areas is illustrated in Fig. 5.9. Here, the initial point of every trajectory is highlighted with a specific marker. Each full trajectory,

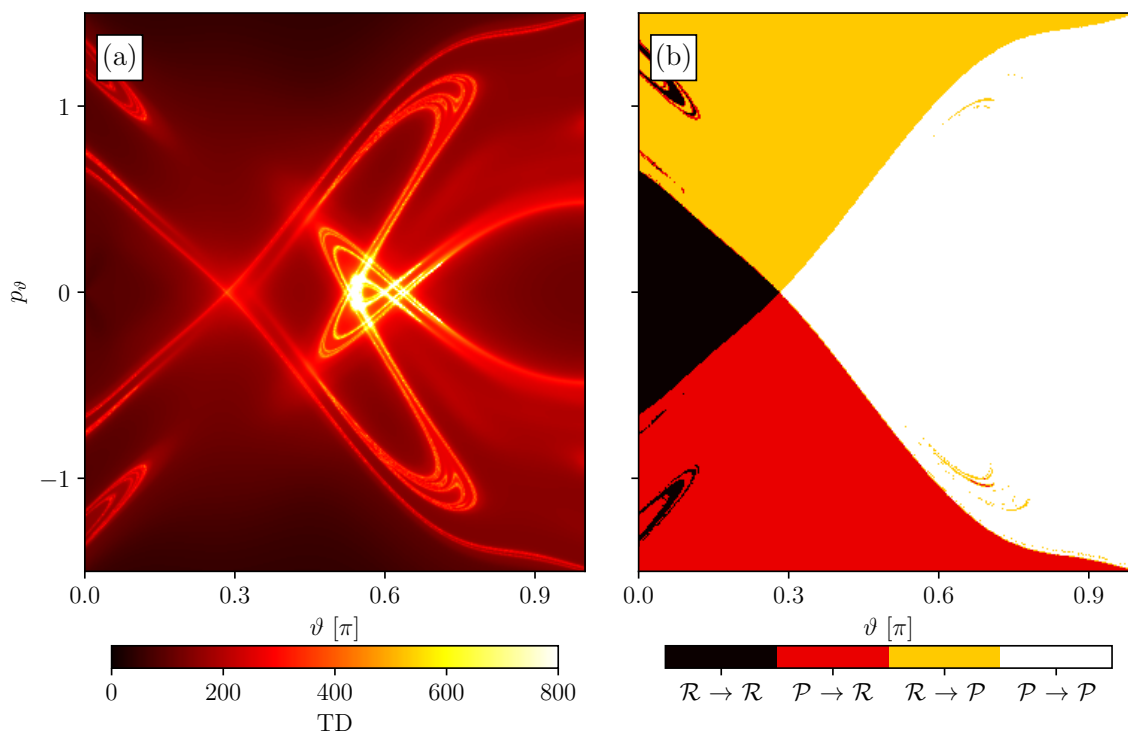


Figure 5.8.: Same as Fig. 5.7 but with the cutoffs chosen such, that a full range of the potential between $\vartheta \in [0, \pi]$ is covered. The cross-like fibers of the manifolds are still the dominant structures in both phase space representations. However, they are superimposed by the beginning fractal-like structures arising from global recrossings at the (bound) LiCN potential.

displayed with a different line style, is obtained by propagating the molecule according to Eq. (5.24) forward and backward in time until the reactant or the product state is reached. Whereas Fig. 5.9 (a) shows the full trajectories in the (R, ϑ) plane of the potential energy surface according to Eq. (5.19), Fig. 5.9 (b) shows a (ϑ, p_ϑ) cross section of the phase space with the reactive and non-reactive areas. Here, only the initial points of each trajectory, highlighted with the respective markers, are displayed. The remaining coordinate p_R of the full phase space is initially set to zero for all four trajectories.

Although the potential of the $\text{LiCN} \rightleftharpoons \text{LiNC}$ isomerization reaction is usually given in the curvilinear coordinate system (R, ϑ) , as in Fig. 5.9, its representation may be converted to the Cartesian body-fixed reference frame (x', z') according to Fig. 5.2. In doing so, the fact that the Li^+ -ion is actually orbiting around the CN^- molecule is more imaginable. A visualization of these reactions, again for the same four trajectories of Fig. 5.9, is given in Fig. 5.10, where all reactive trajectories follow the disk-like channel from reactant \mathcal{R} to product \mathcal{P} or vice versa. All markers, colors and line styles of these trajectories are chosen to be exactly the same as in Fig. 5.9.

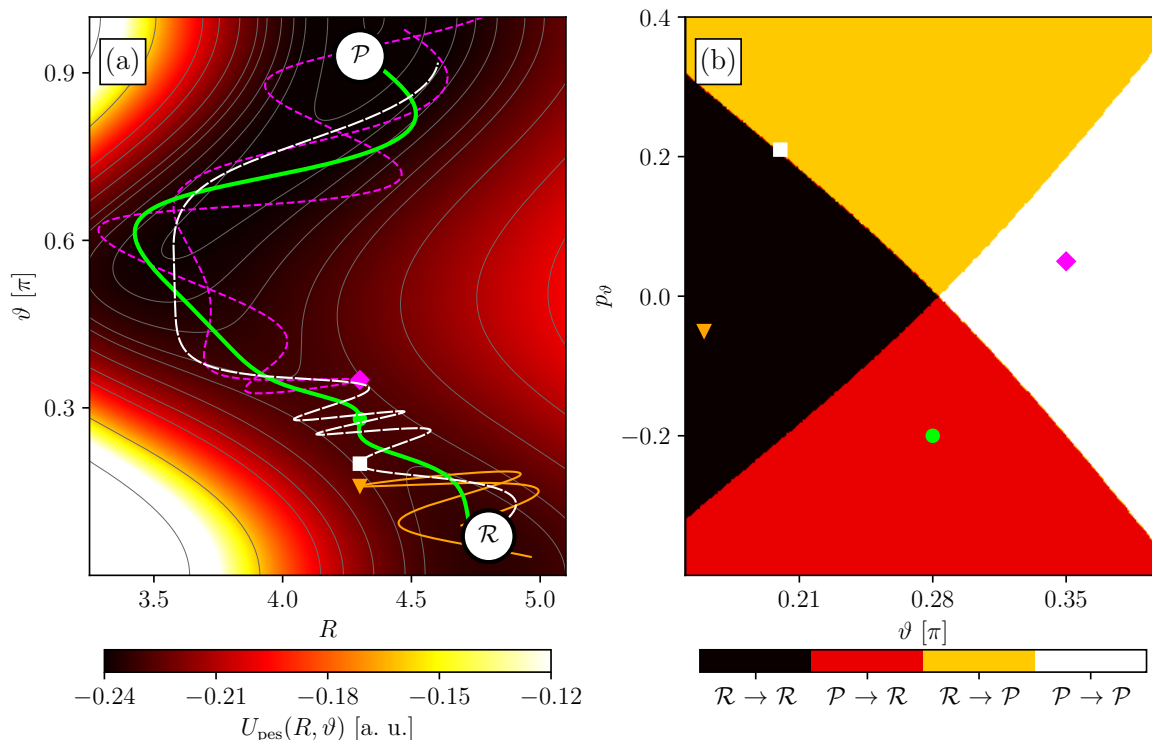


Figure 5.9.: Visualization of the reactive and non-reactive behavior of trajectories, initially launched closely to the barrier region (visualized with individual markers), and propagated according to Eq. (5.24) forward and backward in time until the reactant \mathcal{R} or product \mathcal{P} state is reached. Whereas part (a) shows an (R, ϑ) position space cross section with the potential energy surface $U_{\text{pes}}(R, \vartheta)$ according to Eq. (5.19) as color encoding, in part (b) a (ϑ, p_ϑ) cross section of the phase space with the corresponding reactive and non-reactive areas is displayed. For all trajectories, the remaining coordinate p_R is initially set to zero. For further discussion, see text.

Both Fig. 5.9 and Fig. 5.10 demonstrate two important facts. First of all, the classification of being reactive and non-reactive is correctly assigned. The thin solid yellow trajectory with initial triangle and the thin dashed purple trajectory with initial diamond enter the barrier region, but do not have enough energy to overcome the barrier and ultimately fall back to their initial side. Hence, these two trajectories are non-reactive. The thick solid green trajectory with initial circle, as well as the thick dashed white trajectory with initial rectangle, however, enter the barrier region from one side of the barrier and leave it to the other side. These two trajectories are denoted as reactive trajectories, having enough energy to overcome the barrier. However, there is another important fact illustrated in Figs. 5.9 and 5.10 when comparing the four trajectories directly. Whereas the triangle, diamond and circle trajectory are initialized far away from one of the two

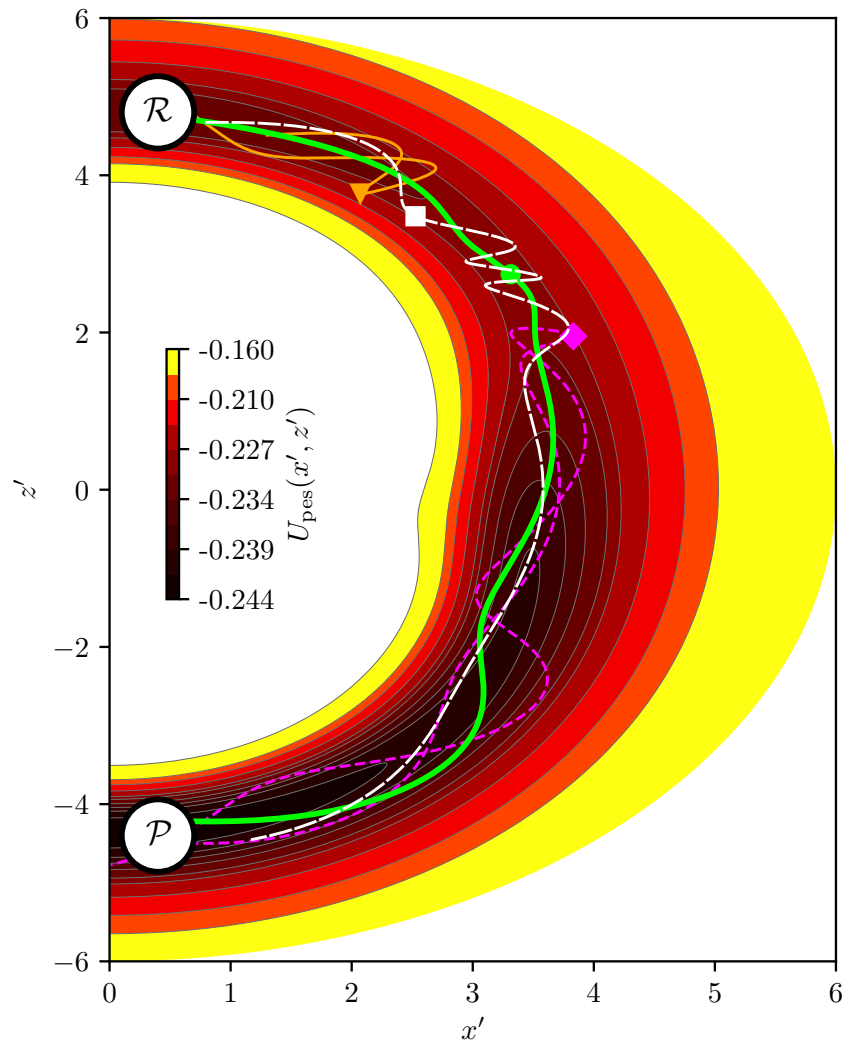


Figure 5.10.: Potential energy surface U_{pes} in the coordinates (x', z') of the body-fixed reference frame according to Fig. 5.2. The four trajectories are the same as in Fig. 5.9, with corresponding line styles, colors and markers.

manifolds (see Fig. 5.9 (b)) the rectangle trajectory is launched very closely to the stable manifold of the barrier, where trajectories approach the corresponding NHIM exponentially slow. Consequently, this trajectory stays in the saddle region much longer, and oscillates nearly three times in the stable direction of the barrier, whereas the circle trajectory, initialized far away from the manifolds, shows only one small oscillation here. When compared to the other three trajectories, the white rectangle trajectory pass the barrier closest to the NHIM, the special subspace of unstable trajectories which are never leaving the barrier region.

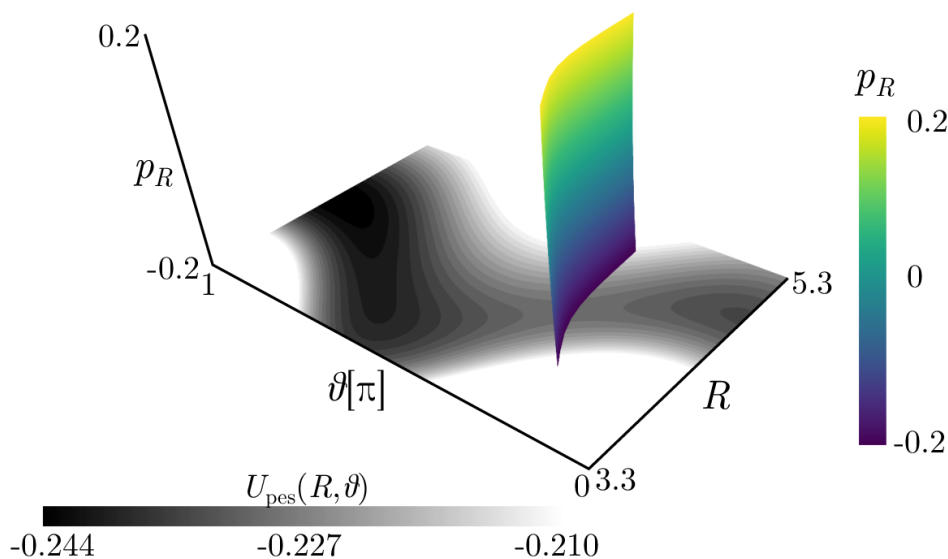


Figure 5.11.: NHIM of the barrier of the non-driven $\text{LiCN} \rightleftharpoons \text{LiNC}$ isomerization reaction. Here, its three-dimensional representation is given in the subspace (R, ϑ, p_R) of the full phase space. Therefore, individual points on the NHIM are obtained in the ranges $R \in [3.8, 5.0]$ and $p_R \in [-0.2, 0.2]$ using the BCM according to Sec. 3.4.1. In the Figure, these points are interpolated to a surface using bi-cubic splines. Its color encoding corresponds to the radial momentum p_R . To clarify the position of the NHIM with respect to the barrier, a two-dimensional representation of the potential energy surface $U_{\text{pes}}(R, \vartheta)$ according to Eq. (5.19) is added in gray scales.

5.2.2 Static NHIM and attached DS

The NHIM is according to Sec. 2.1.3 a co-dimension two manifold embedded in the full phase space. Since the full phase space of the non-driven $\text{LiCN} \rightleftharpoons \text{LiNC}$ isomerization reaction in our model is four-dimensional, the corresponding NHIM of the rank-1 barrier in the potential energy surface (5.19) is two-dimensional. It can be revealed using the BCM according to Sec. 3.4.1. A representation of the NHIM in the three-dimensional subspace (R, ϑ, p_R) is given in Fig. 5.11.

Reactive trajectories, moving closely along the stable manifold of the barrier forward in time (or closely along the unstable manifold backward in time) approach (or depart from) the NHIM asymptotically and when they react, they pierce the attached DS very closely to the NHIM. An example of such a reactive trajectory approaching the NHIM is given in Fig. 5.12. Given in the same three-dimensional representation as in Fig. 5.11, the NHIM and the trajectory are displayed from two different viewing angles. As the reactive trajectory approaches the NHIM, its movement towards the NHIM slows down and it starts to oscillate solely in the stable degree of freedom, along the NHIM. After

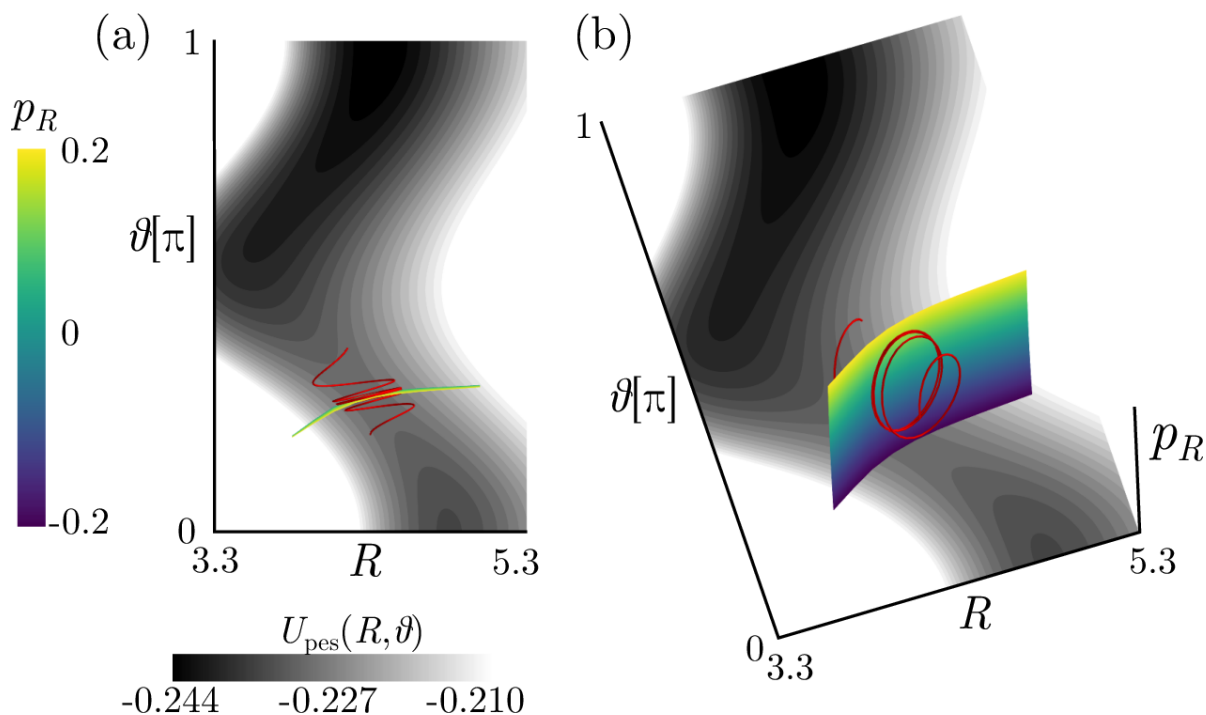


Figure 5.12.: Three-dimensional representation (R, ϑ, p_R) of a reactive trajectory approaching the NHIM of the barrier in the non-driven $\text{LiCN} \rightleftharpoons \text{LiNC}$ isomerization reaction according to Eq. (5.24). Both sub-figures show the same NHIM as a colored surface with p_R as color encoding and the corresponding potential energy surface as a plane in gray scales from two different viewing angles. While the reactive trajectory approaches the NHIM it starts to move solely in the stable direction, along the NHIM.

it has reacted, it is departing with slowly increasing velocity towards the other side of the barrier.

Note, that Fig. 5.12 shows a representation of the two-dimensional NHIM in a three-dimensional subspace (R, ϑ, p_R) of the full phase space. Although it seems like the reactive trajectory pierces the NHIM here, it never fully approaches the NHIM, as it passes the NHIM in the fourth dimension along the p_ϑ axis which cannot be seen here. No trajectory can fully approach the NHIM and afterwards depart from it again, as any trajectory located on the NHIM never leaves this unstable subspace, at least in a mathematical sense. Even if launched exactly on the stable manifold of the barrier, the trajectory would “hit” the NHIM only after infinite time. Furthermore, the surface in Fig. 5.12 is not a DS. As discussed in Sec. 2.1.3, the DS separating reactants from products in the phase space is a hypersurface with one dimension less than the full phase space and it is attached to the NHIM. Since the full phase space of the non-driven $\text{LiCN} \rightleftharpoons \text{LiNC}$ isomerization reaction is four-dimensional according to Eq. (5.24), the

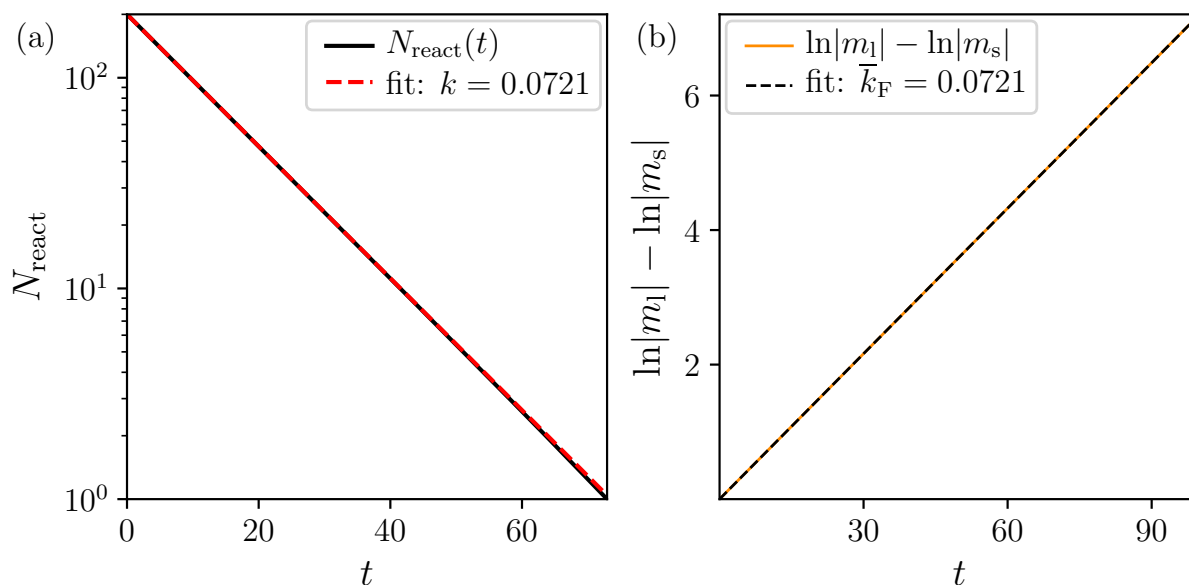


Figure 5.13.: Rate calculations for a trajectory initialized at $R = 4.2636$ and $p_R = 0$ on the NHIM of the non-driven $\text{LiCN} \rightleftharpoons \text{LiNC}$ isomerization reaction according to Eq. (5.24). This position corresponds to the saddle point in Fig. 5.6, marked by a white cross. In both cases, the NHIM was obtained with a tolerance of 10^{-12} using the BCM as explained in Sec. 3.4.1. (a): Ensemble rate (black solid line) obtained by propagating a reactive ensemble of 200 trajectories with a distance of $\Delta\vartheta = 10^{-3}$, as explained in Sec. 4.2. An exponential fit (red dashed line) according to Eq. (5.34) yields a static decay rate of $k = 0.0721$ for this trajectory. (b): Floquet calculation for this trajectory. The orange line shows the difference of the logarithmic eigenvalues $m_{l,s}$ of the stability matrix M , obtained time-dependently according to Sec. 4.4. The slope corresponds to the mean Floquet rate $\bar{k}_F = 0.0721$, obtained via fitting a linear function (black dashed line).

corresponding DS of the barrier would be three-dimensional and cannot be shown as a surface in Fig. 5.12.

5.2.3 Phase-space resolved decay rates close to the static transition state

Having obtained the NHIM and the DS attached for the non-driven $\text{LiCN} \rightleftharpoons \text{LiNC}$ isomerization reaction allows us to propagate reactive ensembles according to Sec. 4.2 to obtain decay rates of reactant population close to the TS. Exemplary, this is done for the unstable state exactly at the saddle point of the barrier with $R = 4.2626$ and $\vartheta = 0.2800\pi$, marked with a white cross in Fig. 5.6. Since the barrier is non-driven, this

special state has no movement in any direction and $p_R = p_\vartheta = 0$. Using the procedure explained in Sec. 4.2, an ensemble of 200 reactive trajectories is initialized close to this state in a (ϑ, p_ϑ) section of the full phase space with a distance of $\Delta\vartheta = 10^{-3}$ according to Fig. 4.1. Trajectories are propagated using a fourth order Runge-Kutta integrator with fixed stepsize of $\Delta t = 0.1$. The precise reaction time of each trajectory is obtained when it pierces the DS separating reactants from products. The DS is attached to the NHIM, that is obtained at the individual positions (R, p_R) of any trajectory using the BCM method with a tolerance of 10^{-12} , see Sec. 3.4.1. The corresponding number of reactants $N_{\text{react}}(t)$ as a function of propagation time is displayed in Fig. 5.13 (a) as a black, solid line. Since the axis in Fig. 5.13 (a) are semi-logarithmic the linear curve progression means an exponential decrease of the number of reactants

$$N_{\text{react}}(t) = N_{\text{react}}(0) \exp(-k t) \quad (5.34)$$

with $N_{\text{react}}(0) = 200$ and a rate constant of $k = 0.0721$. This result corresponds to the expectation of an exponentially decreasing reactant population for a static barrier according to Eq. (2.7).

As a verification, the decay rate of the trajectory resting at the saddle point of the non-driven $\text{LiCN} \rightleftharpoons \text{LiNC}$ isomerization reaction can be calculated directly from its stability using the Floquet method according to Sec. 4.4. As defined in Eq. (4.27), the Floquet rate k_F is the difference of the Floquet exponents which are obtained from the largest and the smallest eigenvalue $m_{l,s}$ of the monodromy matrix. In the special case of the trajectory resting exactly at the saddle point, this monodromy matrix and the corresponding fundamental matrix are the same. A plot of the logarithmic difference of their eigenvalues is given in Fig. 5.13 (b) as an orange solid line. It is increasing linearly with propagation time. A linear fit yields a Floquet rate of $k_F = 0.0721$ for the decay rate associated with this special trajectory. This result perfectly coincides with the obtained ensemble rate according to Fig. 5.13 (a).

Even though the NHIM of the non-driven $\text{LiCN} \rightleftharpoons \text{LiNC}$ isomerization reaction according to Eq. (5.24) is not time-dependent, it is a two-dimensional manifold embedded in the full four-dimensional phase space. It contains not only the unstable and static trajectory resting at the saddle point but also infinitely many other unstable trajectories having significant movement in direction of the orthogonal modes while balancing on the barrier in its unstable degree of freedom. Since the system according to Eq. (5.19) is non-driven, energy is conserved and, consequently, these trajectories are periodic. To resolve this dynamics, 25 different trajectories are propagated for a full period on the NHIM, see white lines in Fig. 5.14. Obviously, trajectories are arranged around a fixed point corresponding to the position of the static trajectory which rests at the saddle point of the barrier at $R = 4.2626$ and $\vartheta = 0.2800\pi$. Whereas the decay rates in Fig. 5.13 are obtained for this static state, in principle, such rates can be obtained for any other trajectory located on the NHIM.

In Fig. 5.14 (a), such a rate calculation is done for an equidistant grid of 100×100 trajectories initialized in between the ranges $R \in [3.8, 5.3]$ and $p_R \in [-0.5, 0.5]$ on the

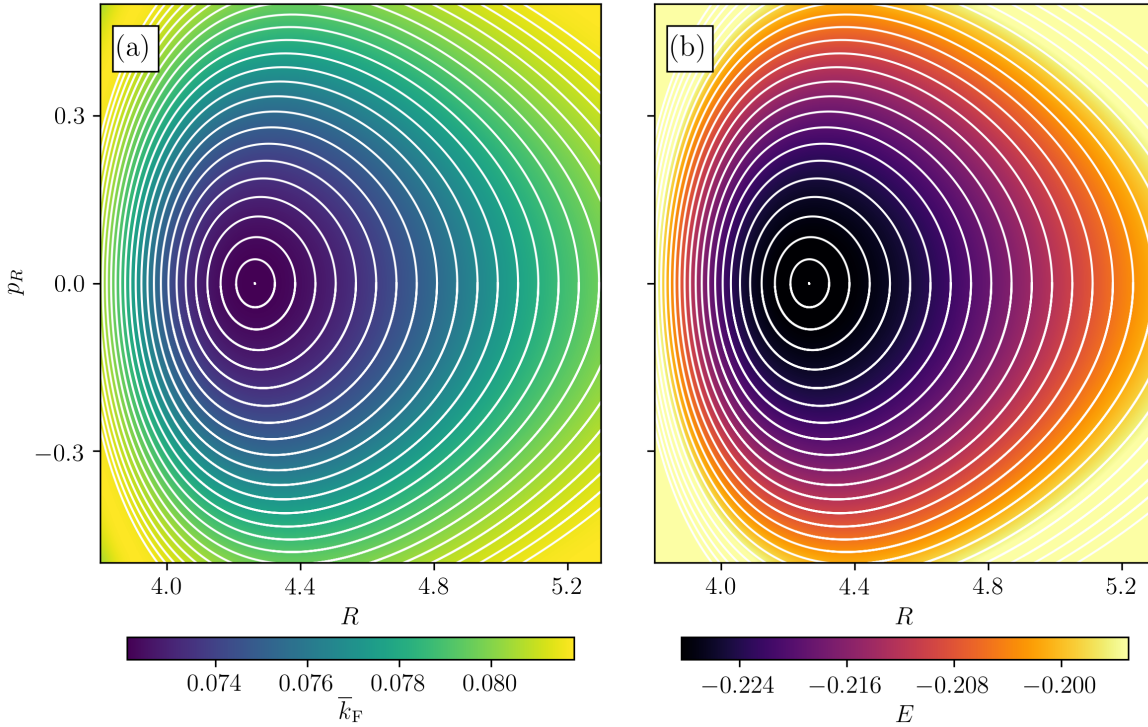


Figure 5.14.: White lines: (R, p_R) of stabilized trajectories on the NHIM of the non-driven $\text{LiCN} \rightleftharpoons \text{LiNC}$ isomerization reaction according to Eq. (5.24). The color encoding in part (a) shows the Floquet rates, obtained for 100×100 stabilized trajectories which are initialized on the NHIM in an equidistant grid with the ranges $R \in [3.8, 5.3]$ and $p_R \in [-0.5, 0.5]$. The color encoding in part (b) shows the respective energy of each trajectory. In order to precisely find the NHIM for a given position (R, p_R) , the BCM according to Sec. 3.4.1 is used with an error tolerance of 10^{-12} and to make the figures more smooth, both color-maps are interpolated using bicubic splines.

NHIM of the non-driven $\text{LiCN} \rightleftharpoons \text{LiNC}$ isomerization reaction. Since all trajectories are periodic, the corresponding decay rates are obtained using the Floquet method according to Sec. 4.4. Therefore, trajectories are stabilized every $\Delta t = 100$ using the BCM with a tolerance of 10^{-12} . At the initial positions (R, p_R) of each trajectory, these Floquet rates are included in Fig. 5.14 (a) as color encoding. Obviously, the Floquet rate of the trajectory resting at the saddle point, here visible as elliptic fixed point of the PSOS, is minimal. Outgoing from this trajectory, the phase-space resolved decay rates grow monotonously in any direction of the NHIM.

To visually examine the correspondence of the obtained Floquet rates in Fig. 5.14 (a) to the energies E of the respective periodic trajectories, these energies are visualized in Fig. 5.14 (b), also as color encoding. Again, the PSOS of the dynamics on the

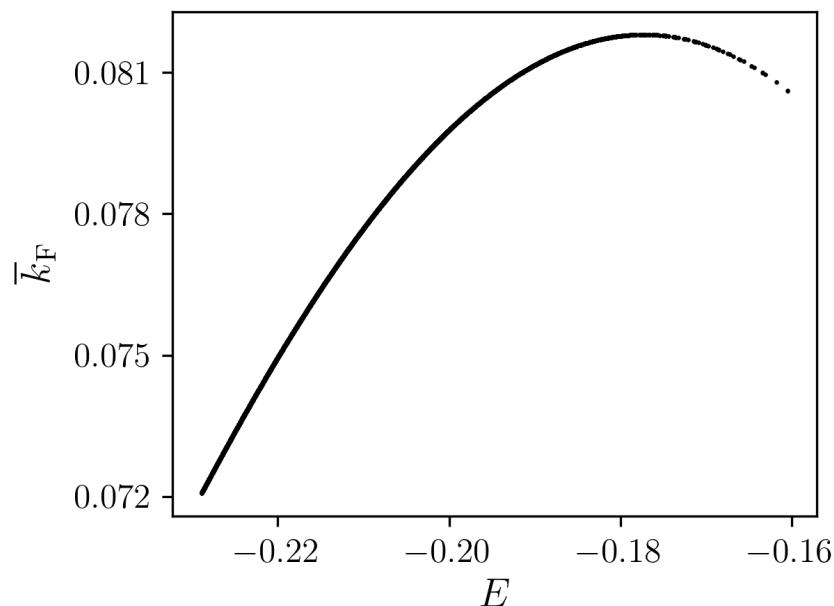


Figure 5.15.: Quantitative relation of the Floquet rates \bar{k}_F of Fig. 5.14 (a) to the energies in Fig. 5.14 (b).

NHIM is included using white dots. When comparing Fig. 5.14 (b) with the energy of trajectories on the NHIM to Fig. 5.14 (a) showing the Floquet rates on the NHIM, the qualitative accordance of both figures is obvious. Clearly, the stability of the TS, and hence of trajectories on the NHIM decreases when having an increasing movement in the orthogonal mode of the barrier. The more movement in this stable degree of freedom, the higher is the decay rate and consequently, the more unstable is a corresponding trajectory.

To further quantify the correspondence of the Floquet rates in Fig. 5.14 (a) to the respective energies in Fig. 5.14 (b), these two quantities can be brought together for all 100×100 trajectories, see Fig. 5.15. Although both the Floquet rate and the energy are specific properties of a periodic trajectory, the relation of these two quantities when switching to another trajectory is, according to Fig. 5.15, non-trivial. The individual points marking the energy and Floquet rate of any trajectory seem to approximate a function $\bar{k}_F(E)$ which shows a maximum at approximately $E = -0.18$. A further increase of the energy of trajectories on the NHIM goes together with a decrease the corresponding decay rate. However, a maximum in the decay rate of a trajectory is associated with a minimum in its stability. According to Fig. 5.15, there seems to be an upper bound for the instability of trajectories on the NHIM in the non-driven LiCN isomerization reaction.

5.3 Periodically driven LiCN isomerization reaction

So far, the results of Sec. 5.2 are obtained for the non-driven $\text{LiCN} \rightleftharpoons \text{LiNC}$ isomerization reaction. Here, the influence of a time-periodic driving caused by an alternating electric field as discussed in Sec. 5.1.3 is described. As an important effect of the external driving according to Eq. (5.33) energy is no longer conserved since the potential $U_{\text{dip}}(R, \vartheta, t)$ is now explicitly time-dependent. Still, a two-dimensional NHIM exists in the barrier region, which contains all trajectories that never leave this region, neither forward, nor backward in time. In contrast to a static system, however, this NHIM starts to oscillate with the same frequency as the barrier, if time-periodically driven.

5.3.1 Dynamics of periodically driven transition states

A useful tool to study the dynamics on the NHIM of a periodically driven system is a PSOS, as introduced in Sec. 3.5. Therefore, the position of each trajectory after integer multiples of the driving period is marked on the NHIM and trajectories have to be integrated for a time much longer than a single period of the external driving.

When propagating trajectories for such a relatively long time, the instability of the dynamics on the NHIM becomes a problem. Here, errors which are produced by any numerical propagator are exponentially increasing in the unstable direction of the barrier. Consequently, trajectories initialized as precisely as possible on the NHIM nevertheless “fall down” from the barrier to either the reactant or to the product side. This problem can be solved by using a stabilized propagator which successively projects unstable trajectories back into the NHIM after an appropriately chosen time Δt using the BCM, as explained in Sec. 3.4.1.

Since the driven NHIM is subject to time-periodic movement, the initial time t_0 at which the PSOS is started becomes relevant. This has important consequences. First of all, a PSOS looks differently for a different initial time $t_1 \neq t_0$ as, in general, the NHIM at t_1 has moved to another position and secondly, periodic trajectories like in Fig. 5.14 for the non-driven barrier usually evolve to full tori with quasi-periodic trajectories in the extended phase space (including time) of a driven system. Another important change is concerning the fixed points visible in such a PSOS. In the case of a non-driven barrier the elliptical fixed point in Fig. 5.14 corresponds to the trajectory resting at the saddle point. However, in a PSOS of a time-periodically driven barrier obtained at time t_0 such a fixed point is the point corresponding to t_0 on a periodic trajectory on the NHIM with respect to the external driving. Since the time-periodically driven NHIM is moving in the phase space, such a trajectory must at least follow its movement to not “fall out” of this unstable subspace. Depending on the amplitude or the frequency of the barrier’s periodic driving, the dynamics of these periodic trajectories, and also the dynamics of

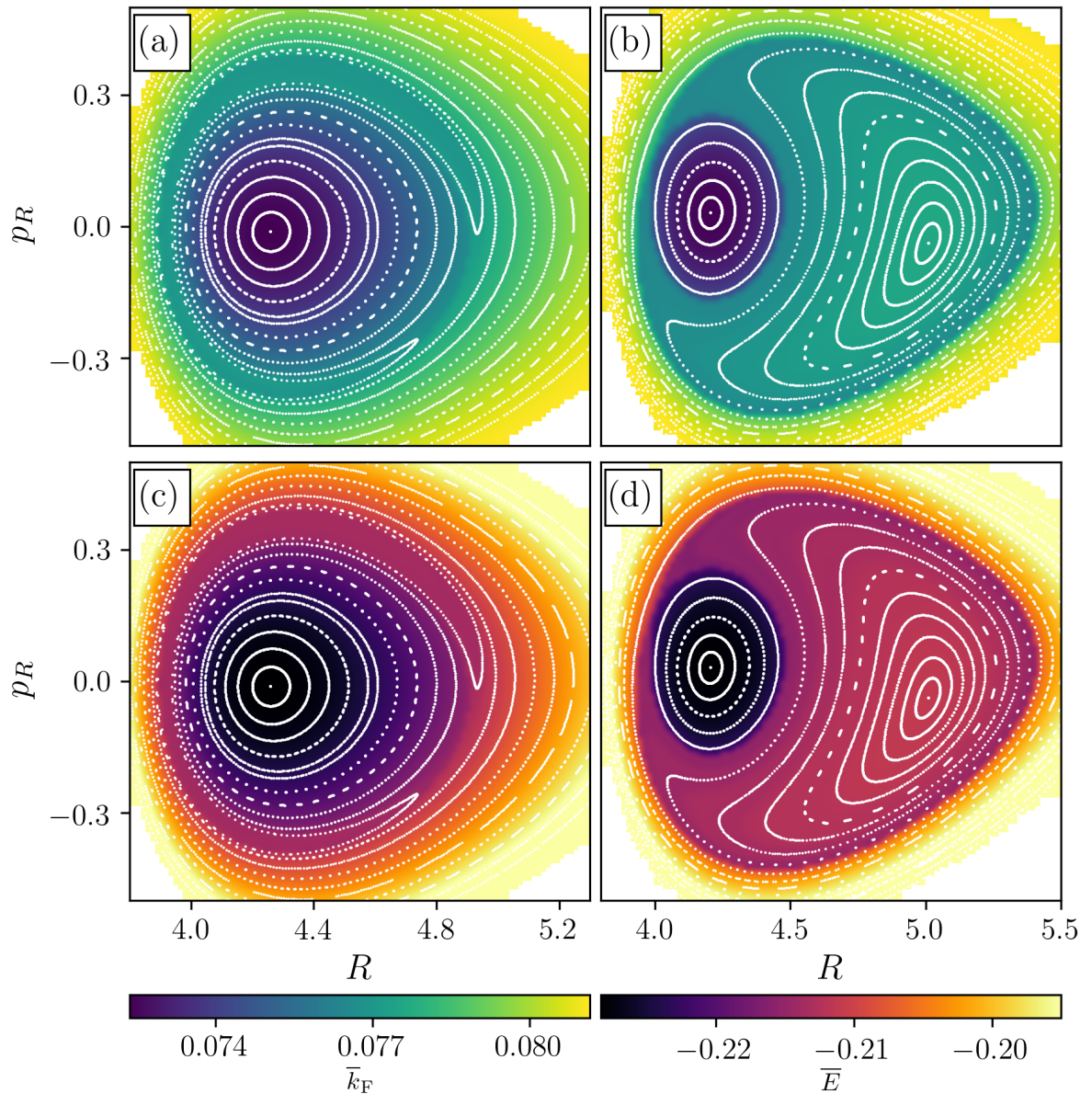


Figure 5.16.: White dots: PSOS visualizing the dynamics of stabilized trajectories on the NHIM of the driven $\text{LiCN} \rightleftharpoons \text{LiNC}$ isomerization reaction according to Eq. (5.33) with amplitude $E_0 = 0.01$. The frequency of the external driving is $\omega = 0.01\pi$ in parts (a) and (c) and $\omega = 0.02\pi$ in parts (b) and (d). The color encoding in parts (a) and (b) show Floquet rates, obtained for 100×100 stabilized trajectories which are initialized on an equidistant grid in the given area of the NHIM. The color encoding in parts (c) and (d) show the respective mean energy of these trajectories, averaged over the full propagation time. For further information, see text.

any other quasi-periodic trajectory on the NHIM, can be rather complex.

Exemplary, a PSOS for stabilized trajectories with various initial conditions on the NHIM, propagated for 400 periods of the external driving according to Eq. (5.33) with amplitude $E_0 = 0.01$ and frequency $\omega = 0.01\pi$ (in atomic units) is displayed in Fig. 5.16 (a) with white dots. Therefore, the initial time was set to $t_0 = 0$. After each period of $T = 200$, the instantaneous position (R, p_R) of each trajectory on the NHIM is marked. The stabilization of trajectories to the NHIM was done using the BCM with an error tolerance of 10^{-12} . In SI units, the external driving corresponds to a laser field with wavelength $\lambda = 1.43 \mu\text{m}$ and amplitude $E_0 = 5.14 \times 10^7 \text{ V/cm}$.

At first glance, the PSOS of the driven barrier in Fig. 5.16 (a) looks very similar to the corresponding Fig. 5.14 of the static case. It has a central fixed point and tori around it. On the right-hand side of Fig. 5.16 (a) at about $R = 4.8$ and $p_R = -0.2$, an unstable fixed point is visible, interruption the regular arrangement of the tori. According to the Poincaré-Birkhoff theorem [114], only an even number of fixed points may occur in a perturbed system, and consequently, the appearance of the unstable fixed point is accompanied by the emergence of a stable fixed point which is located approximately at $R = 3.9$ and $p_R = 0$ and is not directly visible here. In contrast to the non-driven barrier, these structures arise solely due to the external driving.

To clarify this influence of the moving barrier, a second PSOS is obtained in the same way as has been done for Fig. 5.16 (a), but this time, the frequency of the external driving is doubled to $\omega = 0.02\pi$ (this corresponds to laser light with a wavelength of $\lambda = 716 \text{ nm}$). Now, the movement of the NHIM has a strong impact on the bound trajectories and an additional unstable, as well as an additional stable fixed point are clearly visible. Both stable fixed points belong to separate periodic trajectories which are encircled by many quasi-periodic trajectories on various tori.

By the representation of the dynamics on the driven NHIM via a PSOS it is impossible to decide, if there are two separate period-1 trajectories located on the driven NHIM or if both elliptical fixed points correspond to the same period-2 trajectory with respect to the external driving. To answer this question, the trajectories corresponding to the visible elliptical fixed points in Fig. 5.16 (a) and Fig. 5.16 (b) can be plotted in a three-dimensional subspace (R, ϑ, p_R) of the full phase space, see Fig. 5.17 (a). Here, the blue trajectory which corresponds to the visible stable fixed point in Fig. 5.16 (a) at initial position $R = 4.2579$ and $p_R = -0.0117$ shows just very little movement in the stable direction of the barrier. However, the red trajectory, corresponding to the stable fixed point at $R = 4.2040$ and $p_R = 0.0313$, and especially the green trajectory, corresponding to the stable fixed point at $R = 5.0096$ and $p_R = -0.0378$ of Fig. 5.16 (b), are subject to significant movement in the stable direction of the barrier. Interestingly, these two trajectories show two oscillations in direction of the orthogonal mode of the barrier although they are both period-1 trajectories with respect to the external driving. Such a double-oscillatory behavior was up to now not observed in the period-1 trajectories of the model system according to Eq. (3.1). An explanation may be given by the potential according to Eq. (5.19): In the barrier region, the curvature in the unstable direction is

very small when compared to the relatively strong confinement in the orthogonal mode. This confinement defines the velocity of oscillations in the stable degree direction of the barrier. Due to the strong orthogonal confinement of the LiCN potential (5.19), multiple oscillations of a period-1 trajectory are possible, while the trajectory oscillates just a single time in the unstable direction of the barrier. In the model system according to Eq. (3.1), however, the curvature in both directions of the barrier is of the same order of magnitude and for that reason, both oscillations are similarly strong.

5.3.2 Instantaneous decay rates for trajectories on the driven NHIM

Having examined the dynamics on the NHIM of the time-periodically driven $\text{LiCN} \rightleftharpoons \text{LiNC}$ isomerization reaction, the decay rates of reactant population in a close neighborhood of these trajectories is of utmost interest. According to Chapter 4, three methods are available to obtain these decay rates. Here, all of them are going to be applied to the three period-1 trajectories displayed in Fig. 5.17 (a). As a first example, the decay rate of reactant population close to the blue period-1 trajectory with an initial point at $R = 4.2579$ and $p_R = -0.0117$ at time $t = 0$ on the NHIM of the driven barrier with $E_0 = 0.01$ and $\omega = 0.01\pi$ is obtained in Fig. 5.17 (b).

For the ensemble method according to Sec. 4.2, the blue trajectory is divided into 20 segments. For each segment, an ensemble of 200 reactive trajectories is initialized close to the NHIM with a distance of $\Delta\vartheta = 10^{-3}$. Patching together these individual segments yields the thin black line in Fig. 5.17 (b). The corresponding mean ensemble decay rate is obtained by averaging over a full period of the external driving, yielding $\bar{k} = 0.0724$ as vertical thick solid line. This result can be verified using the Floquet method, as explained in Sec. 4.4, which according to Eq. (4.28) yields a mean Floquet rate of $\bar{k}_F = 0.0724$ for this blue trajectory. Given as an orange dotted vertical line in Fig. 5.17 (b) this mean Floquet rate is in perfect agreement with the mean ensemble rate. Using the LMA according to Sec. 4.3, a third verification of these decay rates can be obtained. The thin red dashed line in Fig. 5.17 (b) shows the instantaneous manifold rate $k_M(t)$ and the thick red dashed vertical line the mean manifold rate $\bar{k}_M = 0.0724$, averaged over a full period of the external driving. Both lines fit the results of the other two methods.

The same procedure as in Fig. 5.17 (b) is repeated for the two remaining trajectories of Fig. 5.17 (a) which are obtained for the driven system with $\omega = 0.02\pi$. Figure 5.17 (c) yields the results for the red trajectory and Fig. 5.17 (d) for the green trajectory. In any case, the instantaneous decay rates obtained via the LMA correspond perfectly to the instantaneous decay rates of the ensemble method and their mean rates are also in perfect accordance to the obtained Floquet rates.

By comparing the decay rates of reactant population close to the three different period-1 trajectories in Figs. 5.17 (b)-(d), not only the instantaneous rates and consequently also

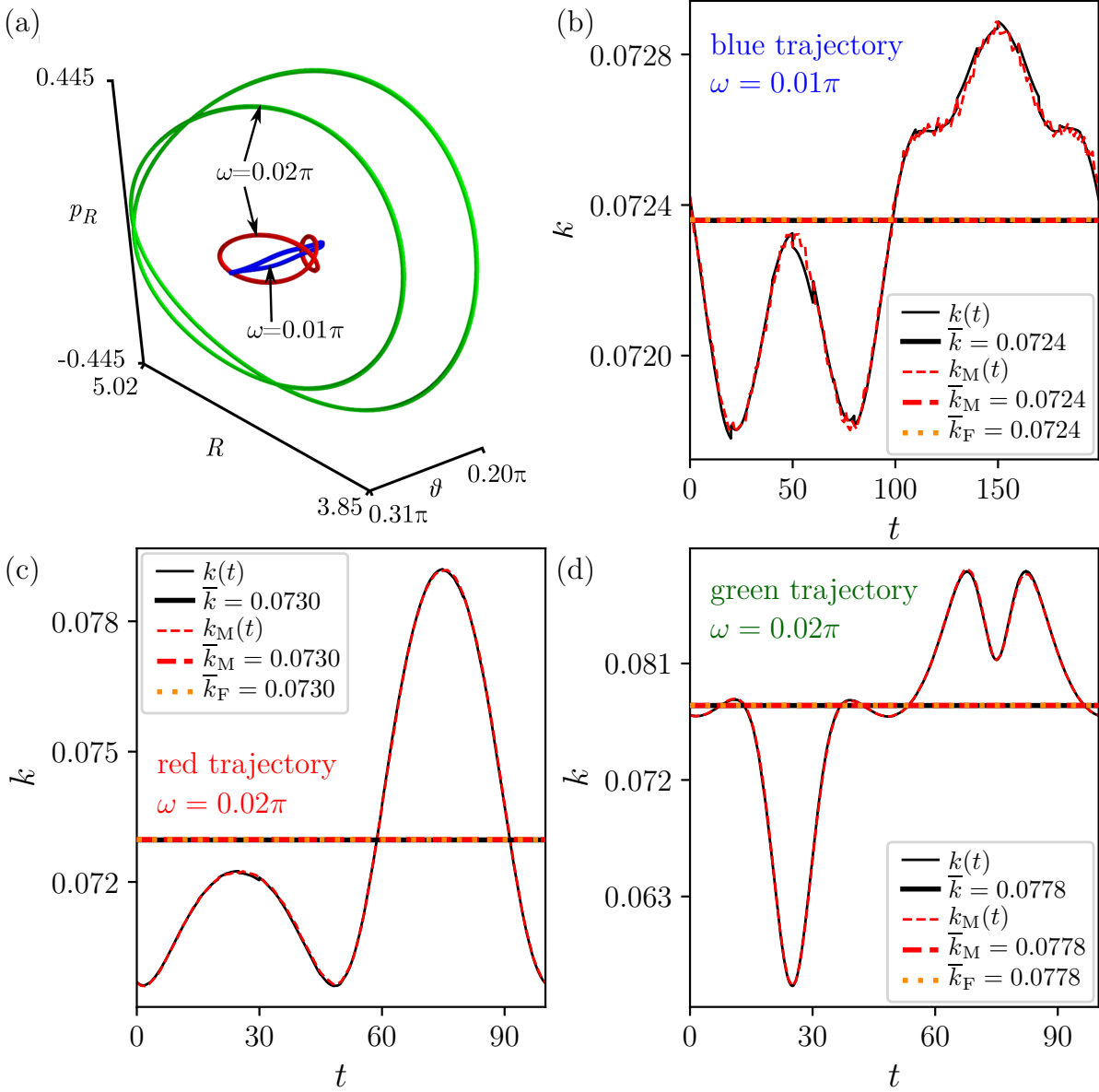


Figure 5.17.: (a): Representation (R, ϑ, p_R) of period-1 trajectories on the NHIM of the driven LiCN isomerization reaction. The blue trajectory corresponds to the central elliptic fixed point in Fig. 5.16 (a), the red and green double-loop trajectories to the elliptic fixed points in Fig. 5.16 (b) at positions $R \approx 4.2$ and $R \approx 5.0$, respectively. Parts (b)-(d) show the instantaneous ensemble rate $k(t)$ (thin black line), obtained according to Sec. 4.2, the time-averaged mean ensemble rate \bar{k} (thick black horizontal line), the mean Floquet rate \bar{k}_F (orange dotted horizontal line) according to Sec. 4.4, the instantaneous manifold rate $k_M(t)$ (thin red dashed line) according to Sec. 4.3 and the time-averaged mean manifold rate \bar{k}_M (thick red horizontal dashed line). For further information, see text.

the mean rates differ significantly, but also the amount of variation of the instantaneous rates is different for each trajectory. For the blue trajectory, that has according to Fig. 5.17 (a) the smallest movement in the orthogonal mode, the relative change of instantaneous rate $\Delta k \approx 10^{-3}$ is very small. This means that the effect of the external driving is barely noticeable here. As a consequence, the plotted k -range in Fig. 5.17 (b) is very narrow and numerical fluctuations in the instantaneous manifold rate $k_M(t)$ are noticeable at this magnification. Also small jumps of $k(t)$ are visible where the 20 individual segments of the instantaneous ensemble rate $\bar{k}(t)$ are patched together. Hence, Fig. 5.17 (b) somehow defines the maximum precision achievable in obtaining decay rates using an integrator with stepsize of $\Delta t = 0.1$. Note, that the calculation time necessary to obtain the instantaneous ensemble rates in Figs. 5.17 (b)-(d) is in the order of a full day¹. To further increase precision, the stepsize of the integrator must be decreased but that would significantly increase calculation time as not only the individual trajectories of the reactive ensemble have to be propagated, but also their precise reaction time has to be determined. Therefore, multiple iterations of the BCM are needed and each BCM iteration again requires the propagation of tens to hundreds of trajectories.

The red trajectory in Fig. 5.17 (a) has significantly more motion in the stable direction of the barrier and the relative change $\Delta k \approx 10^{-2}$ of the instantaneous rate is changing according to Fig. 5.17 (c) considerably larger. Again, the instantaneous ensemble rate and the instantaneous manifold rate coincide perfectly and also the mean rates produced by all three methods are the same. As the magnification of the k -axis is much smaller when compared to Fig. 5.17 (b) effects of the limited stepsize of the integrator are not visible here. For the green trajectory, that has according to Fig. 5.17 (a) by far the largest movement in the stable direction of the barrier, the relative change $\Delta k \approx 0.5 \times 10^{-1}$ in the instantaneous rates in Fig. 5.17 (d) is the largest. Again, the rates obtained by the various methods coincide perfectly.

When comparing the different decay rates of all three trajectories in Fig. 5.17, the influence of the external driving is high if a trajectory has significant motion in direction of the orthogonal modes. To further examine this effect, the rates of the other quasi-periodic trajectories on the NHIM in the vicinity of these periodic orbits are examined. Since the computational effort to obtain decay rates with the ensemble method is very high and the obtained mean ensemble rates coincide perfectly to the Floquet rates, we therefore resort to the much faster Floquet method.

When doing Floquet calculations, the periodicity of trajectories is important. For the non-driven barrier energy is conserved and hence, any trajectory on the NHIM is strictly periodic. Consequently, the time-averaging in the Floquet-method according to Eq. (4.27) has just to be done for a single period of the corresponding trajectory. For a time-periodically driven barrier, however, the conservation of energy is no longer

¹Surely, this information is strongly dependent on, e.g., the hardware used or the amount of optimization included in coding. This statement here is just provided to give the reader a rough hint on how costly the calculations via the ensemble method actually are. In comparison, obtaining the instantaneous manifold rates using the LMA is just a matter of a few minutes.

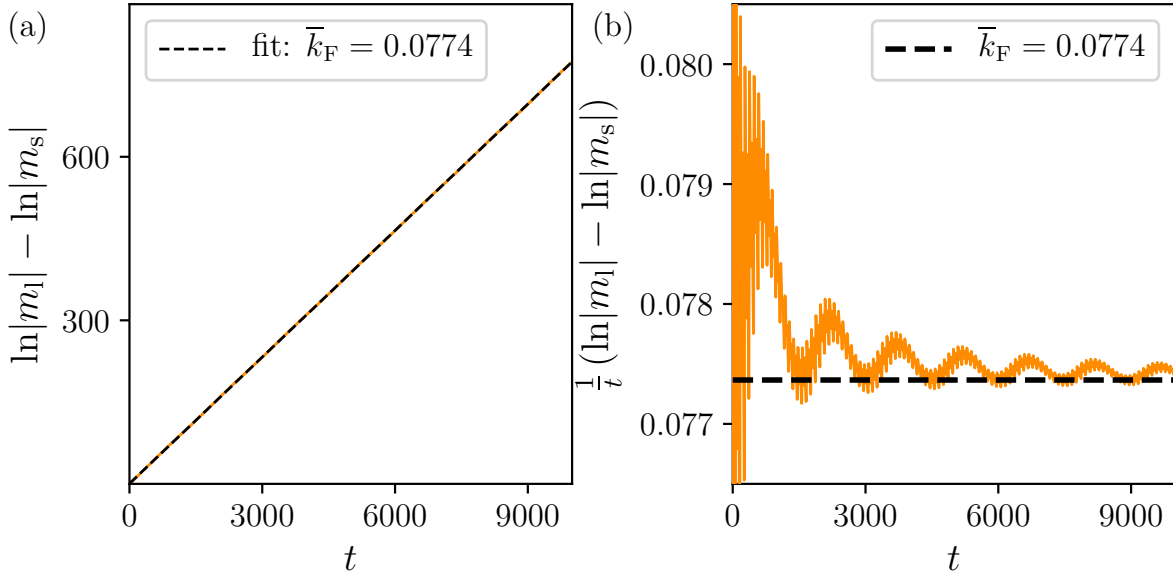


Figure 5.18.: (a): Floquet calculation for a stabilized trajectory, initialized at $R = 4.5$ and $p_R = -0.3$ on the NHIM of system (5.33) at time $t = 0$. Orange line: difference of the logarithmic eigenvalues $m_{1,s}$ of the fundamental matrix according to Sec. 4.4. The slope corresponds to the mean Floquet rate $\bar{k}_F = 0.0743$, obtained via fitting a linear function (black dashed line). (b): Normalized difference (orange solid line) of the corresponding logarithmic eigenvalues $m_{1,s}$ yielding the Floquet rate in the infinite time limit according to Sec. 4.4. The slowly decreasing oscillations converge against the mean Floquet rate $\bar{k}_F = 0.0743$ (orange dotted horizontal line), which is obtained from the linear fit in Fig. 5.18 (a).

satisfied and most of the trajectories on the NHIM are quasi-periodically located on regular tori, as discussed in Figs. 5.16 (a) and (b). For the few periodic trajectories, like the ones displayed in Fig. 5.17 (a), the definition of the Floquet exponents according to Eq. (4.27) still holds. For quasi-periodic trajectories, however, these Floquet exponents need to be obtained according to Eq. (4.29) in an infinite time limit. This can be done by propagating a trajectory for long enough time. Having said that, the question arises how long “long enough” needs to be to represent the infinite time limit in Eq. (4.29) and to yield consistent results for the mean Floquet rate \bar{k}_F . To answer this question, the time-dependent difference of the logarithmic eigenvalues $m_{1,s}$ of the corresponding fundamental matrix is obtained according to Eq. (4.9) in an instantaneous way while propagating such a quasi periodic trajectory on the driven NHIM. This difference is displayed in Fig. 5.18 (a) as a solid orange line which seems to be linearly increasing with propagation time, just like in the static case according to Fig. 5.13 (b). However, when normalizing this difference of the logarithmic eigenvalues $m_{1,s}$ with the propagation

time t , as done in Fig. 5.18 (b) also in a solid orange line, an additional and rather small oscillation of this difference becomes visible. This oscillation arises from the circulation of a quasi-periodic trajectory on one of the stable tori visible in Fig. 5.16. After a full oscillation in Fig. 5.18 (b), the corresponding trajectory has approximately returned to its initial point at $t = 0$. To obtain consistent results for the mean Floquet rate, one has to average out these oscillations in Fig. 5.18 (b) and, hence, the propagation time of the underlying trajectory has to be chosen long enough to cover several of these oscillations. Effectively, this is done by choosing an according fit range of the linear fit in Fig. 5.18 (a). Here, this linear fit yields a Floquet rate of $\bar{k}_F = 0.0774$. According to Fig. 5.18 (b), the normalized instantaneous difference of the logarithmic eigenvalues $m_{l,s}$ of the fundamental matrix converges slowly against exactly this mean Floquet rate.

5.3.3 Phase-space resolved decay rates associated with the periodically driven transition states

Phase-space resolved decay rates of reactant population close to trajectories on the NHIM of the time-dependent $\text{LiCN} \rightleftharpoons \text{LiNC}$ isomerization reaction according to Eq. (5.33) can be efficiently obtained using the numerically fast Floquet method. In Fig. 5.16 (a), the Floquet rates of an equidistant grid of 100×100 stabilized trajectories are displayed as color encoding on the NHIM at time $t = 0$ with $E_0 = 0.01$ and $\omega = 0.01\pi$. All trajectories are propagated for a total time of $t = 10\,000$ and for an improved smoothness of the figure, the individual Floquet rates are interpolated using bicubic splines. To visualize the dynamics on the NHIM, a PSOS is included with white dots. The mean Floquet rate obtained at the clearly visible elliptic fixed point in the center of the tori corresponds to the rates already obtained in Fig. 5.17 (b) with all three methods.

When comparing the obtained mean Floquet rates of the driven system with $E_0 = 0.01$ and $\omega = 0.01\pi$ in Fig. 5.16 (a) to the mean Floquet rates of the static system according to Fig. 5.14 (a), the influence of the external driving is small. In both cases, the mean Floquet rates at the center of the tori are similar ($\bar{k}_F = 0.0721$ for the static and $\bar{k}_F = 0.0724$ for the driven case) and every torus on the NHIM is characterized by a specific mean Floquet rate. The only difference is the slightly indicated emergence of the unstable fixed point on the right-hand side of Fig. 5.16 (a) and the related stable fixed point at about $R = 3.9$ (hardly visible).

These observations change drastically, when increasing the frequency of the external driving to $\omega = 0.02\pi$, see Fig. 5.16 (b). Now, the influence of the external driving on the dynamics on the NHIM is strong and two clearly separated elliptical fixed points are visible in the PSOS of Fig. 5.16 (b), each one encircled by an individual set of tori dividing the NHIM into two areas of very different Floquet rates. This means that two areas of very different stability emerge close to the time-periodically driven NHIM. In the surrounding of the fixed point at $R = 4.2040$ and $p_R = 0.0313$, the decay rates of reactant population are rather small and approximately correspond to the mean Floquet

rate of $\bar{k}_F = 0.0730$ obtained for the central period-1 trajectory according to Fig. 5.17 (c). On the other hand, the mean Floquet rates in an area near the fixed point at $R = 5.0096$ and $p_R = -0.0378$ are rather large and approximately correspond to the mean Floquet rate $\bar{k}_F = 0.0778$ of the associated central period-1 trajectory according to Fig. 5.17 (d).

In the non-driven case, the decay rates of reactant population are, according to Fig. 5.14 (b), strongly correlated to the energy E of the respective periodic trajectories on the NHIM. For a time-periodically driven system, however, the instantaneous energy $E(t)$ of trajectories on the NHIM is not conserved. However, by averaging this instantaneous and non-conserved energy of a specific trajectory over many oscillations on a specific torus, its characteristic mean energy \bar{E} can be obtained. To answer the question of a correlation of this mean energy of bound trajectories to the phase-space resolved decay rates of reactant population close to the TS, in Fig. 5.16 (c) the mean energy \bar{E} has been obtained for the 100×100 stabilized trajectories of Fig. 5.16 (a) on the time-periodically driven NHIM with amplitude $E_0 = 0.01$ and frequency $\omega = 0.01\pi$. It is displayed as color encoding, again using bicubic splines to improve the smoothness of the figure. As expected, the mean energy in Fig. 5.16 (c) is constant for any of the tori, visualizing the dynamics on the NHIM with white dots. When comparing Fig. 5.16 (c) with the mean energies of trajectories to the corresponding mean Floquet rates in Fig. 5.16 (a), the again very strong correlation of both quantities is obvious. As an additional test, the mean energy of stabilized trajectories on the time-periodically driven NHIM with amplitude $E_0 = 0.01$ and $\omega = 0.02\pi$ is displayed in Fig. 5.16 (d). Again, the correlation to Fig. 5.16 (b) is clearly visible.

The correspondence of the Floquet rates in Fig. 5.16 (a) and (b) to the respective mean energies in Fig. 5.16 (c) and (d) can be examined more quantitatively. Therefore, the Floquet rates associated with any trajectory is plotted over its mean energy in Fig. 5.19 (a) for $\omega = 0.01\pi$ and in Fig. 5.19 (b) for $\omega = 0.02\pi$, respectively. Both curves in Fig. 5.19 for the driven barrier appear similar to the static case according to Fig. 5.15. Again, the relation between the Floquet rate of a trajectory on a given torus and the associated mean energy is non-trivial and there seems to exist a maximum decay rate of reactant population associated with trajectories on the NHIM, at least in the examined area. In contrast to the static case, however, for the driven barrier with $\omega = 0.02\pi$ in Fig. 5.19 (b) a significant gap arises at about $\bar{E} = -0.22$.

When looking at Fig. 5.16 (d), this gap corresponds exactly to the boundary between the two different regions of decay rates of the NHIM which are prescribed by the dynamics on tori around distinct fixed points. Whereas this sharp boundary was hard to see in the color encoding in Fig. 5.16 (d), in Fig. 5.19 (b) a gap clearly emerges both in the rate and in the mean energy. At the upper edge of the gap, the points in Fig. 5.19 (b) appear rather wiggly at first before becoming smooth again. The reason for these fluctuations is of numerical nature, since the Floquet method of non-periodic trajectories is according to Eq. 4.29 defined in a limit $t \rightarrow \infty$. However, trajectories in Fig. 5.16 (b) are just propagated for a finite time which causes certain errors of the obtained Floquet rates. In other words, close to the boundary between the two areas of different decay rates on

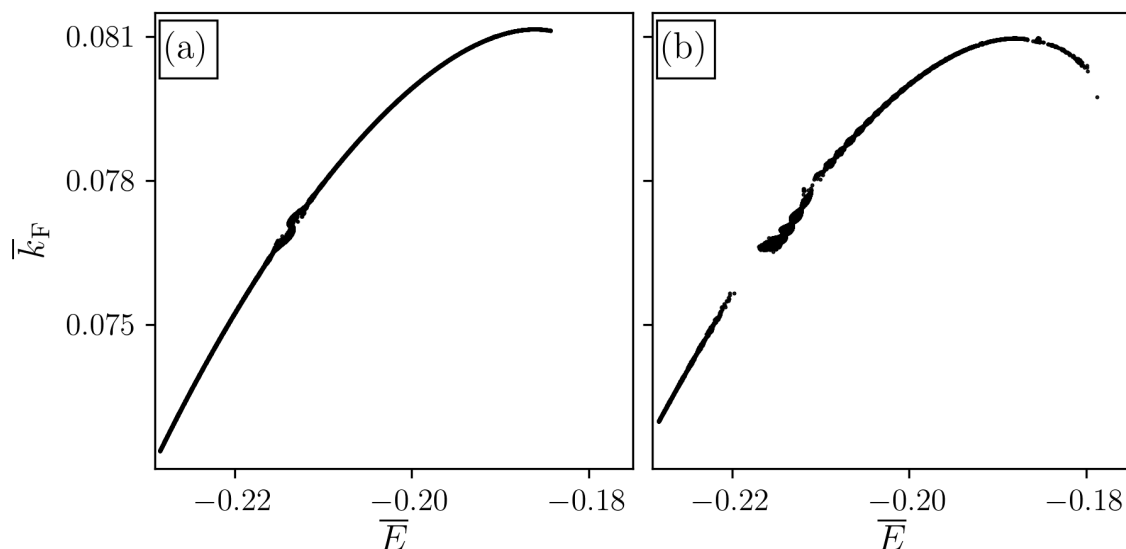


Figure 5.19.: Quantitative relation of the Floquet rates \bar{k}_F to the mean energy of trajectories on the respective tori of Fig. 5.16 (a) and (c) with $\omega = 0.01\pi$ in part (a) and of Fig. 5.16 (b) and (d) with $\omega = 0.02\pi$ in part (b).

the driven NHIM the circulation times of quasi-periodic trajectories on the regular tori increases and longer propagation times are necessary to obtain conclusive results with the Floquet method. This can also be seen in Fig. 5.19 (b) with a driving frequency of $\omega = 0.01\pi$. According to Fig. 5.16 (c), a second stable fixed point is barely visible at this driving frequency, and, consequently, nearly no gap appears in Fig. 5.19 (b). Still, the same wiggly structures are visible at the energy of the indicated fixed point on the left-hand side of Fig. 5.16 (c), and, hence, a gap is just emerging here.

According to these results, both the emergence of different areas of reactant decay close to the NHIM and the existence of gaps in energy and decay rate between these separate areas is an effect solely invoked by the external driving. Furthermore, the different decay rates associated with trajectories in these areas of the NHIM are approximately prescribed by the corresponding central period-1 trajectory.

A more physical interpretation of these areas with different stability on the NHIM as *reactive channels* is tempting since these decay rates are valid also in a close neighborhood of the NHIM. Here, the rates of reactive trajectories which pierce the DS on their way from the reactant side to the product side coincide with these decay rates. For a static barrier only a single reactive channel is open and trajectories, which have just enough energy to overcome the barrier, will pierce the DS close to the central periodic trajectory on the NHIM – according to the corresponding decay rate. However, when time-dependently driving a system, a second reactive channel opens up which is characterized by a different decay rate. If trajectories pierce the DS close to the corresponding central trajectory, they will react, at least locally, with a different rate, approximately

prescribed by the decay rate of the other central trajectory. From this point of view, applying an external field may allow to gain control over an reaction by manipulating reaction rates.

To verify such statements, however, one must go beyond the limits of this thesis since the given results and methods discussed here are – without further justification – only valid in a local neighborhood of the NHIM. Here, the DS certainly is recrossing-free and decay rates are basically prescribed by the linearized dynamics according to the two manifolds. Not discussed, however, is how “large” this local neighborhood is for various systems. In some future Kramers-like approaches (see Sec. 2.2.1) ensembles, which are initialized in a thermal equilibrium state in a reactant basin, are initially clearly located outside this local neighborhood. When a corresponding reactive trajectory passes the barrier region, the question arises where and how long it enters the local neighborhood of the NHIM and, therefore, is influenced by the movement of the barrier. How to extend the local description of the phase space in the neighborhood of the NHIM towards a global description of reaction rates is still an open question and subject to future research.

6

Conclusion and outlook

In this thesis, several advances to TST for time-dependently driven systems are made. After introducing the well-known theoretical basics used to characterize reactions over a static energy barrier in Chapter 2, this theory is generalized to driven systems in Chapter 3. By means of a simple two-dimensional model reaction over a driven rank-1 barrier several methods are introduced and discussed in Sec. 3.3 to reveal the phase space structure of the stable and the unstable manifolds close to the TS. In driven systems the TS, which is also known as the NHIM, is given by the time-dependent intersection of these manifolds. In contrast to the approximative methods known from the literature [11, 30–40], an approach of finding the NHIM via the time-dependent intersection of the stable and the unstable manifold is numerically exact. Individual points on the NHIM can be revealed either by using two nested iterations based on the LD or the TD, or by means of an efficient algorithm based on where reactive or non-reactive trajectories come from in the past and where they go to in the future. This BCM is introduced in Sec. 3.4.

Although being very efficient when compared to the nested iterations approach the BCM requires the time-consuming propagation of several dozens of trajectories according to the EOM. Therefore, using the BCM to obtain rates by propagating a large ensemble of reactive trajectories might be too cumbersome when calculating the position of the NHIM (and the DS attached) relative to each trajectory from scratch. A possible solution to this problem is provided by machine-learning techniques. As briefly discussed in Sec. 3.4.2, using an artificial NN might speed up the process of obtaining individual points on the NHIM considerably if the desired accuracy is not too high.

For the non-thermal systems examined in this thesis, three methods on how to obtain phase-space resolved reactant decay rates close to the TS of a driven system are introduced in Chapter 4. All three methods ultimately yield the same rate. The *ensemble method* according to Sec. 4.2, is based on the actual propagation of reactive ensembles according to the EOM and, hence, only this method would benefit significantly from a machine-learning representation of the NHIM. When dealing with thermal systems (see

also discussion later in this section) this fact can be totally different. In such systems one usually has to average over several realizations of thermal fluctuations in a Langevin-type approach. Here, NNs might become a handy tool to reduce computational time significantly. For a non-thermal but time-dependently driven system, however, the LMA, as an advancement to the ensemble method, requires according to Sec. 4.3 just few but very precise calls of the BCM and, therefore, using machine learning techniques to calculate instantaneous decay rates becomes obsolete.

A third method, the *Floquet method*, is based on analyzing the stability of trajectories on the NHIM as presented in Sec. 4.4. As long as the dynamics on the NHIM is not chaotic, these trajectories are periodic or located on stable tori, as briefly discussed in Sec. 3.5. To each trajectory (or torus), a unique mean decay rate of reactant population close to the TS is associated and can be obtained using the Floquet method.

In Chapter 5 of this thesis, the methods developed for driven systems are applied to the driven $\text{LiCN} \rightleftharpoons \text{LiNC}$ isomerization reaction. Therefore, a mathematical model is introduced in Sec. 5.1.1 by finding a suitable coordinate system and discussing both a potential energy surface as well as a dipole surface known from the literature [1, 2, 102]. The latter surface is used to couple the molecule to a time-periodically oscillating external field. Starting with the non-driven case in Sec. 5.2, the motion of trajectories in the barrier region and the location of both the NHIM and the DS in the phase space close to the energy barrier between LiCN and LiNC are examined and the associated decay of reactant population close to the static TS is obtained. As already expected according to Sec. 3.5, the bound trajectories on the static NHIM are periodic and arranged around the trajectory resting at the saddle point of the barrier. To every trajectory a unique decay rate of reactant population close to the TS is associated. Thereby, the rate of the “saddle point trajectory” is minimal. With increasing energy with respect to the orthogonal modes, the decay rates are also increasing. The specific relation between energy and rate, however, is found to be non-trivial.

When switching to the periodically driven $\text{LiCN} \rightleftharpoons \text{LiNC}$ isomerization reaction in Sec. 5.3 two major effects can be seen. On the one hand, the external driving leads to a time-dependent modulation of the instantaneous decay rates of reactant population close to the TS. As a consequence, also the mean decay rates change accordingly. On the other hand, also the dynamics of trajectories on the NHIM is directly altered by the external driving and additional fixed points arise. Whereas for the static reaction such a fixed point corresponds to the static trajectory resting at the saddle point, the fixed points in the driven system correspond to periodic trajectories on the NHIM having the same period as the external driving. These periodic orbits are approximately defining the decay rates in a close area on the NHIM and, interestingly, the decay rates of different areas around different periodic trajectories are also significantly different. This effect is not seen for the static isomerization reaction and is, therefore, caused solely by the external driving.

As already briefly discussed at the end of Sec. 5.3.3, it is tempting to interpret these areas of different decay of reactant population close to the TS as reactive channels.

Whereas for the static barrier only one reactive channel is open for trajectories that have just enough energy to overcome the barrier, applying an external field opens up a second reactive channel which is characterized by a different decay rate. From this point of view, the external field allows to gain control over the reaction since it directly manipulates the decay rates close to the TS. A verification of such statements is, however, beyond the limits of this thesis and, therefore, subject to future research. Here, the results are only valid in a local neighborhood of the TS where reactive trajectories pierce the DS with a small distance Δp_x to the NHIM and the dynamics is mostly linear and directly prescribed by the stable and the unstable manifolds. In this thesis, it is not examined how “large” this local neighborhood is for various systems or how to extend the given methods to other areas of the phase space. Outside this local regime, a linear DS attached to the NHIM might not be recrossing-free any more. If such unwanted recrossings are detected, what can be easily tested for a given DS using the ensemble method, a more complicated DS needs to be taken into account. Furthermore, the LMA, which is based on a linearization of the dynamics close to the DS will not be directly applicable to reactant population outside this linear regime and modifications to obtain instantaneous decay rates need to be found. The ultimate goal would be to find a direct connection between the decay rates presented in this thesis and the reaction rates in a Kramers-like approach (see Sec. 2.2.1) for driven systems – although even the existence of such a connection is currently unknown. An initial point towards this ambitious goal would be to specify the areas of the phase space where such reactive trajectories on their way from the reactant to the product state pierce the DS relative to the NHIM.

Apart from generalizing the locally found decay rates to a global description over a moving barrier, the advances made in this thesis give a good basis for future research in the context of TST for time-dependently driven systems. As an example, one could further examine the dynamics on the NHIM and the corresponding decay rates of reactant population close to the TS. Interesting questions arise regarding to how exactly the additional “reactive channels” emerge when time-periodically driving a system. Such an investigation could be either done quasi-statically for various external fields with different frequency and amplitude or dynamically for in- and decreasing driving.

Another open question arises when regarding the dynamics on the NHIM. In this thesis the limitation “as long as it is not chaotic” is always made. The reason therefore is, that so far no chaotic dynamics of trajectories on the NHIM has been found for neither of the two examined systems. However, in principle there is no limitation preventing the chaotic dynamics of trajectories on the driven NHIM and a future work could deal with the question of finding the parameters at which chaos arises. Testing the here presented methods in a regime close to the emergence of chaotic trajectories will be both interesting and challenging. Thereby, one needs to pay special attention that the *normal hyperbolicity* of the NHIM is preserved and that the Lyapunov exponents of the chaotic trajectories on the NHIM are always smaller than the Lyapunov exponents of the trajectories leaving this unstable subspace. Violating this assumption would lead to a break-down of the NHIM.

Apart from applying the methods introduced in this thesis to other systems like, e. g., ketene [43], KCN [115], the spin system already examined in Refs. [97, 98] or to more complex and higher-dimensional systems another possible project for future work would be to include a Langevin-based thermal description to the systems already used in this thesis. As discussed in Sec. 1, a first approach in that direction was already done in Refs. [44–46] for the single trajectory the NHIM collapses to in the long-term limit when introducing friction (and noise) to a system. When averaged for long enough, the methods presented in this thesis can be applied to this specific trajectory to obtain its instantaneous rate and thereof the corresponding mean decay rate of reactant population close to the thermal TS. Examining the temperature dependence of these mean decay rates will be very interesting and a next step towards the description of more realistic systems.

A

Constants and equations for the LiCN potential

In this appendix, the equations and expansion coefficients for the representation of the LiCN potential energy surface introduced in Sec. 5.1.2 as well as for its dipole surface according to Sec. 5.1.3 are given. The expectation values $\langle Q_{L,0} \rangle$ of the multipole moment expansion according to Eq. (5.15) of the CN^- ion in LiCN are listed in Table A.1. The induction coefficients $C_{l_1, l_2, L}$ needed to express the classical induction energy between the two closed-shell ions Li^+ and CN^- in a series expansion according to Eq. (5.16) are given in Table A.2. According to Ref. [102], these coefficients are symmetric when exchanging

Table A.1.: Expectation values $\langle Q_{L,0} \rangle$ of the multipole moment expansion of order L according to Eq. (5.15) of the CN^- ion in LiCN, originally published in Refs. [1, 102].

	$L = 0$	$L = 1$	$L = 2$	$L = 3$	$L = 4$	$L = 5$	$L = 6$
$\langle Q_{L,0} \rangle$	-1.00	-0.2151	-3.414	-3.819	-15.84	-14.29	-43.82

Table A.2.: Induction coefficients $C_{l_1, l_2, L}$ for the expansion of the classical induction energy according to Eq. (5.16) between the closed-shell ions Li^+ and the CN^- . These numerical values were originally published in Ref. [1].

	$L = 0$	$L = 1$	$L = 2$	$L = 3$	$L = 4$	$L = 5$	$L = 6$
$C_{1,1,L}$	-10.53		-3.17				
$C_{2,1,L}$		-10.31		2.03			
$C_{2,2,L}$	-57.49		-35.71		5.23		
$C_{3,1,L}$			-35.56		5.95		
$C_{3,2,L}$		-101.45		-37.62		-14.23	
$C_{3,3,L}$	-458.2		-353.7		-112.6		-108.3

A. Constants and equations for the LiCN potential

Table A.3.: Expansion coefficients A_L , B_L and C_L according to Eq. (5.18) for the short range interaction between the two closed-shell ions Li^+ and CN^- due to exchange and penetration effects. These numerical values were originally published in Ref. [1].

L	A_L	B_L	C_L
0	-1.38321	0.14001	0.207892
1	-2.95791	1.47977	-0.011613
2	-4.74203	1.81199	-0.017818
3	-1.88853	1.28750	0.027728
4	-4.41433	2.32297	-0.070693
5	-4.02565	2.77538	-0.137720
6	-5.84259	3.48085	-0.186331
7	-2.61681	2.65559	-0.005882
8	-6.34466	4.34498	-0.152914
9	15.2023	-6.54925	1.302568

Table A.4.: Expansion coefficients according to Eqs. (5.28) for the short range part of the dipole moment of the LiCN molecule. This table shows the original data from Ref. [2] including the corrections of Ref. [113].

	$\lambda = 0$	$\lambda = 1$	$\lambda = 2$	$\lambda = 3$
$a_{\lambda,0}$	-0.4465	-1.481×10^{-3}	-0.4720	-1.845×10^{-3}
$b_{1,\lambda,0}$	0.3017	2.847	-1.2678	2.024
$b_{2,\lambda,0}$	-0.03481	-0.4505	0.2009	-0.2757
$a_{\lambda,1}$		0.09428	-0.5551	
$b_{1,\lambda,1}$		0.2914	-0.8401	
$b_{2,\lambda,1}$		-0.06052	0.07694	

l_1 and l_2 . Following Eq. (5.18), also the short range interaction between these ions can be expressed in a series expansion to take into account exchange and penetration effects. The coefficients A_L , B_L and C_L of this expansion are listed in Table A.3. To couple the molecule to a time-periodically oscillating field as introduced in Sec. 5.1.3, its dipole surface is needed. According to Eq. (5.28) this surface can be represented again via a series expansion with the coefficients listed in Table A.4. Originally, these coefficients were published in Ref. [2], where a small mistake was made. According to Ref. [113], the coefficients $a_{1,0}$ and $a_{3,0}$ have to be negatively signed. In Table A.4, this mistake is corrected.

The Legendre polynomials $P_L(\cos(\vartheta))$ of order L according to Ref. [106] and their derivatives which are used in the present work are listed in Eqs. (A.1) and Eqs. (A.2).

$$P_0(\cos(\vartheta)) = 1 \quad (\text{A.1a})$$

$$P_1(\cos(\vartheta)) = \cos(\vartheta) \quad (\text{A.1b})$$

$$P_2(\cos(\vartheta)) = \frac{3 \cos^2(\vartheta) - 1}{2} \quad (\text{A.1c})$$

$$P_3(\cos(\vartheta)) = (5 \cos^2(\vartheta) - 3) \frac{\cos(\vartheta)}{2} \quad (\text{A.1d})$$

$$P_4(\cos(\vartheta)) = \frac{1}{8} (35 \cos^4(\vartheta) - 30 \cos^2(\vartheta) + 3) \quad (\text{A.1e})$$

$$P_5(\cos(\vartheta)) = \frac{1}{8} \cos(\vartheta) (63 \cos^4(\vartheta) - 70 \cos^2(\vartheta) + 15) \quad (\text{A.1f})$$

$$P_6(\cos(\vartheta)) = \frac{1}{16} (231 \cos^6(\vartheta) - 315 \cos^4(\vartheta) + 105 \cos^2(\vartheta) - 5) \quad (\text{A.1g})$$

$$\frac{d}{d\vartheta} P_0(\cos(\vartheta)) = 0 \quad (\text{A.2a})$$

$$\frac{d}{d\vartheta} P_1(\cos(\vartheta)) = -\sin(\vartheta) \quad (\text{A.2b})$$

$$\frac{d}{d\vartheta} P_2(\cos(\vartheta)) = -3 \sin(\vartheta) \cos(\vartheta) \quad (\text{A.2c})$$

$$\frac{d}{d\vartheta} P_3(\cos(\vartheta)) = -\frac{3}{2} \sin(\vartheta) (5 \cos^2(\vartheta) - 1) \quad (\text{A.2d})$$

$$\frac{d}{d\vartheta} P_4(\cos(\vartheta)) = -\frac{5}{2} \sin(\vartheta) \cos(\vartheta) (7 \cos^2(\vartheta) - 3) \quad (\text{A.2e})$$

$$\frac{d}{d\vartheta} P_5(\cos(\vartheta)) = -\frac{15}{8} \sin(\vartheta) (21 \cos^4(\vartheta) - 14 \cos^2(\vartheta) + 1) \quad (\text{A.2f})$$

$$\frac{d}{d\vartheta} P_6(\cos(\vartheta)) = -\frac{21}{8} \sin(\vartheta) \cos(\vartheta) (33 \cos^4(\vartheta) - 30 \cos^2(\vartheta) + 5) \quad (\text{A.2g})$$

$$\frac{d}{d\vartheta} P_7(\cos(\vartheta)) = -\frac{7}{16} \sin(\vartheta) (429 \cos^6(\vartheta) - 495 \cos^4(\vartheta) + 135 \cos^2(\vartheta) - 5) \quad (\text{A.2h})$$

$$\begin{aligned} \frac{d}{d\vartheta} P_8(\cos(\vartheta)) &= -\frac{9}{16} \sin(\vartheta) \cos(\vartheta) \\ &\quad \times (715 \cos^6(\vartheta) - 1001 \cos^4(\vartheta) + 385 \cos^2(\vartheta) - 35) \end{aligned} \quad (\text{A.2i})$$

$$\begin{aligned} \frac{d}{d\vartheta} P_9(\cos(\vartheta)) &= -\frac{45}{128} \sin(\vartheta) (2431 \cos^8(\vartheta) - 4004 \cos^6(\vartheta) \\ &\quad + 2002 \cos^4(\vartheta) - 308 \cos^2(\vartheta) + 7) \end{aligned} \quad (\text{A.2j})$$



Bibliography

- [1] R. Essers, J. Tennyson, and P. E. S. Wormer. An SCF potential energy surface for Lithium Cyanide. *Chem. Phys. Lett.* 89, 223–227 (1982).
- [2] G. Brocks, J. Tennyson, and A. van der Avoird. Ab initio dipole surfaces, vibrationally averaged dipole moments, and infrared transition intensities for KCN and LiCN. *J. Chem. Phys.* 80, 3223–3233 (1984).
- [3] A. D. McNaught and A. D. McNaught. *Compendium of chemical terminology*, volume 1669. Blackwell Science Oxford (1997).
- [4] C. Jaffé, D. Farrelly, and T. Uzer. Transition State Theory without Time-Reversal Symmetry: Chaotic Ionization of the Hydrogen Atom. *Phys. Rev. Lett.* 84, 610–613 (2000).
- [5] G. Jacucci, M. Toller, G. DeLorenzi, and C. P. Flynn. Rate Theory, Return Jump Catastrophes, and the Center Manifold. *Phys. Rev. Lett.* 52, 295 (1984).
- [6] T. Komatsuzaki and R. S. Berry. Regularity in chaotic reaction paths. I. Ar₆. *J. Chem. Phys.* 110, 9160–9173 (1999).
- [7] T. Komatsuzaki and R. S. Berry. Chemical Reaction Dynamics: Many-Body Chaos and Regularity. *Adv. Chem. Phys.* 123, 79–152 (2002).
- [8] M. Toller, G. Jacucci, G. DeLorenzi, and C. P. Flynn. Theory of classical diffusion jumps in solids. *Phys. Rev. B* 32, 2082 (1985).
- [9] A. F. Voter, F. Montalenti, and T. C. Germann. Extending the time scale in atomistic simulations of materials. *Annu. Rev. Mater. Res.* 32, 321–346 (2002).

- [10] H. P. de Oliveira, A. M. Ozorio de Almeida, I. Damiaõ Soares, and E. V. Tonini. Homoclinic chaos in the dynamics of a general Bianchi type-IX model. *Phys. Rev. D* 65, 083511/1–9 (2002).
- [11] C. Jaffé, S. D. Ross, M. W. Lo, J. Marsden, D. Farrelly, and T. Uzer. Statistical Theory of Asteroid Escape Rates. *Phys. Rev. Lett.* 89, 011101 (2002).
- [12] H. Waalkens, A. Burbanks, and S. Wiggins. Escape from planetary neighborhoods. *Mon. Not. R. Astron. Soc.* 361, 763 (2005).
- [13] C. Huepe, S. Métens, G. Dewel, P. Borckmans, and M. E. Brachet. Decay rates in attractive Bose-Einstein condensates. *Phys. Rev. Lett.* 82, 1616 (1999).
- [14] C. Huepe, L. S. Tuckerman, S. Métens, and M. E. Brachet. Stability and decay rates of nonisotropic attractive Bose-Einstein condensates. *Phys. Rev. A* 68, 023609 (2003).
- [15] A. Junginger, J. Main, G. Wunner, and M. Dorwarth. Transition state theory for wave packet dynamics. I. Thermal decay in metastable Schrödinger systems. *J. Phys. A: Math. Theor.* 45, 155201 (2012).
- [16] A. Junginger, M. Dorwarth, J. Main, and G. Wunner. Transition state theory for wave packet dynamics. II. Thermal decay of Bose-Einstein condensates with long-range interaction. *J. Phys. A: Math. Theor.* 45, 155202 (2012).
- [17] A. Junginger, M. Kreibich, J. Main, and G. Wunner. Transition states and thermal collapse of dipolar Bose-Einstein condensates. *Phys. Rev. A* 88, 043617 (2013).
- [18] J. C. Lorquet. Crossing the dividing surface of transition state theory. IV. Dynamical regularity and dimensionality reduction as key features of reactive trajectories. *J. Chem. Phys.* 146, 134310 (2017).
- [19] S. Patra and S. Keshavamurthy. Detecting reactive islands using Lagrangian descriptors and the relevance to transition path sampling. *Phys. Chem. Chem. Phys.* 20, 4970–4981 (2018).
- [20] V. Krajňák and H. Waalkens. The phase space geometry underlying roaming reaction dynamics. *J. Math. Chem.* 56, 2341–2378 (2018).
- [21] Y. Tamiya, R. Watanabe, H. Noji, C. Li, and T. Komatsuzaki. Effects of non-equilibrium angle fluctuation on F1-ATPase kinetics induced by temperature increase. *Phys. Chem. Chem. Phys.* 20, 1872–1880 (2018).
- [22] H. Eyring. The Activated Complex in Chemical Reactions. *J. Chem. Phys.* 3, 107–115 (1935).

-
- [23] E. P. Wigner. Calculation of the Rate of Elementary Association Reactions. *J. Chem. Phys.* 5, 720–725 (1937).
- [24] P. Pechukas. Transition State Theory. *Annu. Rev. Phys. Chem.* 32, 159 (1981).
- [25] D. G. Truhlar, B. C. Garrett, and S. J. Klippenstein. Current Status of Transition-State Theory. *Journal of Physical Chemistry* 100, 12771–12800 (1996).
- [26] R. G. Mullen, J.-E. Shea, and B. Peters. Communication: An existence test for dividing surfaces without recrossing. *J. Chem. Phys.* 140, 041104 (2014).
- [27] S. Wiggins. The role of normally hyperbolic invariant manifolds (NHIMS) in the context of the phase space setting for chemical reaction dynamics. *Regul. Chaotic Dyn.* 21, 621–638 (2016).
- [28] S. Wiggins. *Normally Hyperbolic Invariant Manifolds in Dynamical Systems*. Springer, New York (1994).
- [29] M. Feldmaier, P. Schraft, R. Bardakcioglu, J. Reiff, M. Lober, M. Tschöpe, A. Junginger, J. Main, T. Bartsch, and R. Hernandez. Invariant manifolds and rate constants in driven chemical reactions. *J. Phys. Chem. B* 123, 2070–2086 (2019).
- [30] D. G. Truhlar and B. C. Garrett. Variational Transition State Theory. *Annu. Rev. Phys. Chem.* 35, 159–189 (1984).
- [31] E. Vanden-Eijnden and F. A. Tal. Transition state theory: Variational formulation, dynamical corrections, and error estimates. *J. Chem. Phys.* 123, 184103 (2005).
- [32] E. Pollak and P. Pechukas. Transition States, Trapped Trajectories, and Classical Bound States Embedded in the Continuum. *J. Chem. Phys.* 69, 1218–1226 (1978).
- [33] P. Pechukas and E. Pollak. Classical Transition State Theory is Exact if the Transition State is Unique. *J. Chem. Phys.* 71, 2062–2068 (1979).
- [34] R. Hernandez and W. H. Miller. Semiclassical Transition State Theory. A New Perspective. *Chem. Phys. Lett.* 214, 129–136 (1993).
- [35] R. Hernandez. A Combined Use of Perturbation Theory and Diagonalization: Application to Bound Energy Levels and Semiclassical Rate Theory. *J. Chem. Phys.* 101, 9534–9547 (1994).
- [36] T. Uzer, C. Jaffé, J. Palacián, P. Yanguas, and S. Wiggins. The geometry of reaction dynamics. *Nonlinearity* 15, 957–992 (2002).

- [37] H. Teramoto, M. Toda, and T. Komatsuzaki. Dynamical Switching of a Reaction Coordinate to Carry the System Through to a Different Product State at High Energies. *Phys. Rev. Lett.* 106, 054101 (2011).
- [38] C. Li, A. Shoujiguchi, M. Toda, and T. Komatsuzaki. Definability of No-Return Transition States in the High-Energy Regime above the Reaction Threshold. *Phys. Rev. Lett.* 97, 028302 (2006).
- [39] H. Waalkens and S. Wiggins. Direct construction of a dividing surface of minimal flux for multi-degree-of-freedom systems that cannot be recrossed. *J. Phys. A* 37, L435–L445 (2004).
- [40] Ü. Çiftçi and H. Waalkens. Reaction Dynamics Through Kinetic Transition States. *Phys. Rev. Lett.* 110, 233201 (2013).
- [41] A. Allahem and T. Bartsch. Chaotic dynamics in multidimensional transition states. *J. Chem. Phys.* 137, 214310 (2012).
- [42] A. Junginger, P. L. Garcia-Muller, F. Borondo, R. M. Benito, and R. Hernandez. Solvated molecular dynamics of LiCN isomerization: All-atom argon solvent versus a generalized Langevin bath. *J. Chem. Phys.* 144, 024104 (2016).
- [43] G. T. Craven and R. Hernandez. Deconstructing field-induced ketene isomerization through Lagrangian descriptors. *Phys. Chem. Chem. Phys.* 18, 4008–4018 (2016).
- [44] T. Bartsch, R. Hernandez, and T. Uzer. Transition state in a noisy environment. *Phys. Rev. Lett.* 95, 058301 (2005).
- [45] T. Bartsch, T. Uzer, and R. Hernandez. Stochastic transition states: Reaction geometry amidst noise. *J. Chem. Phys.* 123, 204102 (2005).
- [46] T. Bartsch, J. M. Moix, R. Hernandez, S. Kawai, and T. Uzer. Time-dependent transition state theory. *Adv. Chem. Phys.* 140, 191–238 (2008).
- [47] H. A. Kramers. Brownian motion in a field of force and the diffusion model of chemical reactions. *Physica* 7, 284–304 (1940).
- [48] P. Hänggi, P. Talkner, and M. Borkovec. Reaction-rate theory: fifty years after Kramers. *Rev. Mod. Phys.* 62, 251 (1990).
- [49] S. Wiggins. *Introduction to Applied Nonlinear Dynamical Systems and Chaos*. Springer, New York (1990).
- [50] T. Komatsuzaki and R. S. Berry. Regularity in chaotic reaction paths. II. Ar₆. Energy dependence and visualization of the reaction bottleneck. *Phys. Chem. Chem. Phys.* 1, 1387–1397 (1999).

-
- [51] C.-B. Li, A. Shoujiguchi, M. Toda, and T. Komatsuzaki. Dynamical Hierarchy in Transition States in Reactions. *Few-Body Systems* 38, 173–179 (2006).
- [52] C.-B. Li, M. Toda, and T. Komatsuzaki. Bifurcation of no-return transition states in many-body chemical reactions. *J. Chem. Phys.* 130, 124116 (2009).
- [53] M. Feldmaier, A. Junginger, J. Main, G. Wunner, and R. Hernandez. Obtaining time-dependent multi-dimensional dividing surfaces using Lagrangian descriptors. *Chem. Phys. Lett.* 687, 194 (2017).
- [54] P. Schraft, A. Junginger, M. Feldmaier, R. Bardakcioglu, J. Main, G. Wunner, and R. Hernandez. Neural network approach to time-dependent dividing surfaces in classical reaction dynamics. *Phys. Rev. E* 97, 042309 (2018).
- [55] A. Junginger, L. Duvenbeck, M. Feldmaier, J. Main, G. Wunner, and R. Hernandez. Chemical dynamics between wells across a time-dependent barrier: Self-similarity in the Lagrangian descriptor and reactive basins. *J. Chem. Phys.* 147, 06401 (2017).
- [56] S. Wiggins. *Normally hyperbolic invariant manifolds in dynamical systems*, volume 105. Springer Science & Business Media (2013).
- [57] N. Fenichel and J. K. Moser. Persistence and smoothness of invariant manifolds for flows. *Indiana University Mathematics Journal* 21, 193–226 (1971).
- [58] N. Fenichel. Asymptotic stability with rate conditions. *Indiana University Mathematics Journal* 23, 1109–1137 (1974).
- [59] N. Fenichel. Asymptotic stability with rate conditions, II. *Indiana University Mathematics Journal* 26, 81–93 (1977).
- [60] M. A. Junginger. *Transition state theory for wave packet dynamics and its application to thermal decay of metastable nonlinear Schrödinger systems*. Dissertation, Universität Stuttgart (2014).
- [61] P. J. Mohr, D. B. Newell, and B. N. Taylor. CODATA recommended values of the fundamental physical constants: 2014. *Journal of Physical and Chemical Reference Data* 45, 043102 (2016).
- [62] S. K. Upadhyay. *Chemical Kinetics and Reaction Dynamics*. Springer Netherlands (2006).
- [63] K. A. Connors. *Chemical Kinetics: The Study of Reaction Rates in Solution*. Wiley-VCH (1990).

- [64] A. M. Mancho, S. Wiggins, J. Curbelo, and C. Mendoza. Lagrangian Descriptors: A Method for Revealing Phase Space Structures of General Time Dependent Dynamical Systems. *Commun. Nonlinear Sci. Numer. Simul.* 18, 3530 – 3557 (2013).
- [65] G. T. Craven and R. Hernandez. Lagrangian descriptors of thermalized transition states on time-varying energy surfaces. *Phys. Rev. Lett.* 115, 148301 (2015).
- [66] A. Junginger and R. Hernandez. Uncovering the geometry of barrierless reactions using Lagrangian descriptors. *J. Phys. Chem. B* 120, 1720 (2016).
- [67] A. Junginger and R. Hernandez. Lagrangian descriptors in dissipative systems. *Phys. Chem. Chem. Phys.* 18, 30282 (2016).
- [68] R. Bardakcioglu, A. Junginger, M. Feldmaier, J. Main, and R. Hernandez. Binary contraction method for the construction of time-dependent dividing surfaces in driven chemical reactions. *Phys. Rev. E* 98, 032204 (2018).
- [69] T. B. Blank, S. D. Brown, A. W. Calhoun, and D .J. Doren. Neural network models of potential energy surfaces. *J. Chem. Phys.* 103, 4129–4137 (1995).
- [70] J. Behler and M. Parrinello. Generalized neural-network representation of high-dimensional potential-energy surfaces. *Phys. Rev. Lett.* 98, 146401 (2007).
- [71] J. Behler. Atom-centered symmetry functions for constructing high-dimensional neural network potentials. *J. Chem. Phys.* 134, 074106 (2011).
- [72] J. Cui and R. V. Krems. Efficient non-parametric fitting of potential energy surfaces for polyatomic molecules with Gaussian processes. *J. Phys. B* 49, 224001 (2016).
- [73] R. A. Vargas-Hernández, Y. Guan, D. H. Zhang, and R. V. Krems. Bayesian optimization for the inverse scattering problem in quantum reaction dynamics. *New J. Phys.* 21, 022011 (2019).
- [74] M. Rupp, A. Tkatchenko, K.-R. Müller, and O. A. von Lilienfeld. Fast and accurate modeling of molecular atomization energies with machine learning. *Phys. Rev. Lett.* 108, 058301 (2012).
- [75] J. Cui and R. V. Krems. Gaussian Process model for collision dynamics of complex molecules. *Phys. Rev. Lett.* 115, 073202 (2015).
- [76] J. Cui, Z. Li, and R. V. Krems. Gaussian process model for extrapolation of scattering observables for complex molecules: From benzene to benzonitrile. *J. Chem. Phys.* 143, 154101 (2015).

-
- [77] F. A. Faber, A. Lindmaa, O. A. von Lilienfeld, and R. Armiento. Machine Learning Energies of 2 Million Elpasolite (A B C 2 D 6) Crystals. *Phys. Rev. Lett.* 117, 135502 (2016).
- [78] B. Huang and O. A. von Lilienfeld. The “DNA” of chemistry: Scalable quantum machine learning with “amons”. *arXiv preprint arXiv:1707.04146* (2017).
- [79] S. Manzhos and T. Carrington Jr. A random-sampling high dimensional model representation neural network for building potential energy surfaces. *J. Chem. Phys.* 125, 084109 (2006).
- [80] K.-I. Funahashi. On the approximate realization of continuous mappings by neural networks. *Neural Networks* 2, 183 – 192 (1989).
- [81] D. E. Rumelhart, G. E. Hinton, and R. J. Williams. Learning representations by back-propagating errors. *Nature* 323, 533–538 (1986).
- [82] M. Feldmaier, R. Bardakcioglu, J. Reiff, J. Main, and R. Hernandez. Phase-space resolved rates in driven multidimensional chemical reactions. *J. Chem. Phys.* 151, 244108 (2019).
- [83] M. Tschöpe. *Application of neural networks to determine the transition state trajectory in periodically driven systems with two or more degrees of freedom*. Master’s thesis, 1. Institut für Theoretische Physik, Universität Stuttgart (2018).
- [84] M. Tschöpe, M. Feldmaier, J. Main, and Rigoberto Hernandez. Neural network approach for the dynamics on the normally hyperbolic invariant manifold of periodically driven systems. *Phys. Rev. E* 101, 022219 (2020).
- [85] M. Kuchelmeister. *Untersuchung der Dynamik auf der normal hyperbolisch invarianten Mannigfaltigkeit eines periodisch getriebenen Systems mit Rang-1-Sattel*. Bachelor’s thesis, 1. Institut für Theoretische Physik, Universität Stuttgart (2019).
- [86] F. Revuelta, G. T. Craven, T. Bartsch, F. Borondo, R. M. Benito, and R. Hernandez. Transition state theory for activated systems with driven anharmonic barriers. *J. Chem. Phys.* 147, 074104 (2017).
- [87] T. Mielich. *Machine Learning Methods for the Computation of Rate Constants in Driven Chemical Reactions*. Master’s thesis, 1. Institut für Theoretische Physik, Universität Stuttgart (2019).
- [88] G. T. Craven, T. Bartsch, and R. Hernandez. Communication: Transition State Trajectory Stability Determines Barrier Crossing Rates in Chemical Reactions Induced by Time-Dependent Oscillating Fields. *J. Chem. Phys.* 141, 041106 (2014).

- [89] J. Reiff, R. Bardakcioglu, M. Feldmaier, J. Main, and R. Hernandez. Controlling decay rates in model chemical reactions through external driving (In preparation, 2020).
- [90] H. Goldstein. *Classical mechanics*. Addison-Wesley series in physics. Addison-Wesley (1980).
- [91] M. J. Lober. *Parameter Dependent Rates in Transition State Theory for Periodically Driven Systems*. Bachelor's thesis, 1. Institut für Theoretische Physik, Universität Stuttgart (2018).
- [92] J. P. Schraft. *Neural networks for the approximation of time-dependent dividing surfaces in Transition State Theory*. Master's thesis, 1. Institut für Theoretische Physik, Universität Stuttgart (2017).
- [93] J. Reiff. *Dynamik und Trennflächen für getriebene Systeme mit zwei zeitabhängigen Sattelpunkten*. Master's thesis, 1. Institut für Theoretische Physik, Universität Stuttgart (2018).
- [94] J. Reiff, M. Feldmaier, J. Main, and R. Hernandez. Dynamics and decay rates of a time-dependent two-saddle system (Submitted to Phys. Rev. E, 2020).
- [95] R. Bardakcioglu, J. Reiff, M. Feldmaier, J. Main, and R. Hernandez. Thermal decay rates of an activated complex in a driven model chemical reaction (In preparation, 2020).
- [96] J. C. J. Zatsch. *Berücksichtigung der Mondrotation beim Asteroideneinfang an Lagrangepunkten*. Bachelor's thesis, 1. Institut für Theoretische Physik, Universität Stuttgart (2019).
- [97] R. Schuldt. *Zeitabhängige Theorie des Übergangszustands und Methode der Lagrangedeskriptoren für ein getriebenes Spin-System*. Master's thesis, 1. Institut für Theoretische Physik, Universität Stuttgart (2017).
- [98] J. Mögerle. *Ratenkonstanten für den Spinflip in einem getriebenen Zweischichtenmodell*. Bachelor's thesis, 1. Institut für Theoretische Physik, Universität Stuttgart (2019).
- [99] M. Feldmaier, J. Reiff, R. M. Benito, F. Borondo, J. Main, and R. Hernandez. Influence of external driving on decays in the geometry of the LiCN isomerization. *J. Chem. Phys.* 153, 084115 (2020).
- [100] J. Meija, T. B. Coplen, M. Berglund, W. A. Brand, P. De Bièvre, M. Gröning, N. E. Holden, J. Irrgeher, R. D. Loss, T. Walczyk, et al. Atomic weights of the elements 2013 (IUPAC Technical Report). *Pure and Applied Chemistry* 88, 265–291 (2016).

-
- [101] G. Brocks and J. Tennyson. Ab initio rovibrational spectrum of LiNC and LiCN. *J. Mol. Spectrosc.* 99, 263–278 (1983).
- [102] P. E. S. Wormer and J. Tennyson. Ab initio SCF calculations on the potential energy surface of potassium cyanide (KCN). *J. Chem. Phys.* 75, 1245–1252 (1981).
- [103] E. Clementi, H. Kistenmacher, and H. Popkie. Study of the electronic structure of molecules. XVIII. Interaction between a lithium atom and a cyano group as an example of a polytopic bond. *J. Chem. Phys.* 58, 2460–2466 (1973).
- [104] V. A. Istomin, N. F. Stepanov, and B. I. Zhilinskii. Vibration-rotation problem for triatomic molecules with two large-amplitude coordinates: Spherical model. *J. Mol. Spectrosc.* 67, 265–282 (1977).
- [105] J. Berkowitz, W. A. Chupka, and T. A. Walter. Photoionization of HCN: the electron affinity and heat of formation of CN. *J. Chem. Phys.* 50, 1497–1500 (1969).
- [106] A. R. Edmonds. *Angular momentum in quantum mechanics*. Princeton university press (1960).
- [107] R. Courant and D. Hilbert. *Methods of Mathematical Physics* (New York: Interscience) 1 (1953).
- [108] R. M. Berns and A. van der Avoird. N₂-N₂ interaction potential from abinitio calculations, with application to the structure of (N₂)₂. *J. Chem. Phys.* 72, 6107–6116 (1980).
- [109] R. M. Benito, F. Borondo, J.-H. Kim, B. G. Sumpter, and G. S. Ezra. Comparison of classical and quantum phase space structure of nonrigid molecules, LiCN. *Chem. Phys. Lett.* 161, 60–66 (1989).
- [110] A. Vergel, R. M. Benito, J. C. Losada, and F. Borondo. Geometrical analysis of the LiCN vibrational dynamics: A stability geometrical indicator. *Phys. Rev. E* 89, 022901 (2014).
- [111] W. H. Press, S. A. Teukolsky, W. T. Vetterling, and B. P. Flannery. *Numerical recipes 3rd edition: The art of scientific computing*. Cambridge university press (2007).
- [112] J. D. Jackson. *Classical electrodynamics*. John Wiley & Sons (2012).
- [113] G. E. Murgida, F. J. Arranz, and F. Borondo. Quantum control of isomerization by robust navigation in the energy spectrum. *J. Chem. Phys.* 143, 214305 (2015).

- [114] S. Wimberger. Nonlinear dynamics and quantum chaos. *Cham, Switzerland: Springer International. Crossref* (2014).
- [115] H. Párraga, F. J. Arranz, R. M. Benito, and F. Borondo. Ab initio potential energy surface for the highly nonlinear dynamics of the KCN molecule. *J. Chem. Phys.* 139, 194304 (2013).



Zusammenfassung in deutscher Sprache

Der Begriff *Reaktion* tritt meistens im Kontext der Chemie auf. Hier beschreibt er die Umwandlung einer chemischen Verbindung in eine andere [3]. Tatsächlich sind solche Umwandlungen nicht nur auf die Chemie beschränkt. In den richtigen Koordinaten beschrieben kann eine Reaktion von einem Zustand in einen anderen in einer Vielzahl von Systemen gefunden werden, z. B. in der Atomphysik [4], der Festkörperphysik [5], der Bildung von Clustern [6, 7], der Diffusionsdynamik [8, 9], der Kosmologie [10], der Himmelsmechanik [11, 12], der Bose-Einstein Kondensation [13–17] oder der Dynamik chemischer Reaktionen [18–21].

In vielen Fällen lässt sich die Dynamik eines solchen Systems durch klassische Mechanik beschreiben, z. B. die Bewegung einzelner Atome oder Moleküle bei chemischen Reaktionen auf einer Born-Oppenheimer Potentialfläche. Im Rahmen der Theorie der Übergangszustände (engl. transition state theory, TST) [22–27] können solche Reaktionen zwischen einem Ausgangszustand, dem *Reaktant*, und einem Endzustand, dem *Produkt*, sowohl qualitativ, als auch quantitativ beschrieben werden. Normalerweise treten diese Zustände als lokale Minima in der zugehörigen Potentialfläche auf. Hierbei sind sie durch eine Energiebarriere, den *Sattel*, getrennt. Typischerweise besitzt solch ein Sattel eine instabile Richtung, die *Reaktionskoordinate*, und eine gewisse Anzahl an stabilen Richtungen, die *orthogonalen Moden*. Erfüllt er diese Eigenschaften, wird er als *Rang-1 Sattel* bezeichnet.

Eine reaktive Trajektorie muss in einem klassischen und zeitunabhängigen Hamiltonschen System mindestens so viel Energie besitzen, dass sie eine Barriere in der Nähe des Sattelpunktes überquert. Andererseits stellt die lokale Nachbarschaft des Sattelpunktes im Phasenraum einen Flaschenhals für den Großteil der reaktiven Trajektorien dar. Zwar können solche Trajektorien den Sattel auch weit entfernt vom Sattelpunkt und somit mit einer wesentlich höheren Energie überqueren. In der Nähe des Sattelpunktes ist die Energie reaktiver Trajektorien jedoch minimal und deshalb ihre Dichte am größten. Eine wesentliche Grundannahme der TST ist, dass Reaktionsraten hauptsächlich durch die Vorgänge in diesem Flaschenhals bestimmt werden, da hier der Fluss reaktiver

Trajektorien über die Barriere am langsamsten ist. Aus diesem Grund ist es sehr wichtig, fundierte Kenntnisse über die Dynamik reaktiver und nichtreaktiver Trajektorien in diesem Flaschenhals zu erlangen. Diese Dynamik wird im Wesentlichen durch eine spezielle Mannigfaltigkeit bestimmt, die normal hyperbolische invariante Mannigfaltigkeit (NHIM) [28, 29].

Die NHIM ist ein spezieller Unterraum des vollen Phasenraums nahe des Sattelpunktes. Sie beherbergt Trajektorien, welche sich weder zum Reaktanten- noch zum Produktgebiet zuordnen lassen – weder bei einer Propagation vorwärts noch bei einer Propagation rückwärts in der Zeit. Aus diesem Grund ist sie oft auch unter dem Namen *Übergangszustand* (engl. transition state, TS) bekannt. Die Dynamik auf der NHIM ist instabil. Das bedeutet, dass schon die kleinste Abweichung einer Trajektorie von der NHIM dazu führt, dass diese Trajektorie das Sattelgebiet entweder zur Reaktanten- oder zur Produktseite verlässt.

Um Reaktionsraten aus dem Fluss reaktiver Trajektorien über eine Barriere bestimmen zu können, muss für jede Trajektorie sowohl bekannt sein, *wo* sie reagiert, als auch *wann* diese Reaktion stattfindet. Im Rahmen der TST bedeutet das Wort *Reaktion*, dass eine Trajektorie das Gebiet der Reaktanten verlässt und durch eine sogenannte *Trennfläche* (engl. dividing surface, DS) in das Gebiet der Produkte eindringt. Ein einfaches und intuitives Beispiel einer solchen Trennfläche wäre eine planare Ebene, welche sich an den Sattelpunkt angeheftet in die Richtung der orthogonalen Moden erstreckt.

In den allermeisten Fällen ist eine solche planare Trennfläche jedoch eine starke Vereinfachung, da sie von vielen reagierenden Trajektorien auf dem Weg von Reaktant zu Produkt mehrfach durchstoßen wird [22–25]. Charakterisiert man das Durchstoßen einer Trajektorie durch diese Trennfläche als Reaktion, so würde in solch einem Fall die Reaktionsrate durch die mehrfachen Durchstoßpunkte überschätzt werden. Folglich ist eine solche Reaktionsrate, wenn sie denn berechnet wird, immer eine obere Grenze für die tatsächliche Reaktionsrate.

Um sicherzustellen, dass tatsächlich die wirkliche Reaktionsrate bestimmt wird, muss eine Trennfläche gefunden werden, welche von jeder reagierenden Trajektorie nur einmal durchstoßen wird. Eine solche Trennfläche ist im Normalfall hochdimensional und nicht trivial gekrümmt. Aus diesem Grund ist ihre Bestimmung meist ein schwieriges Unterfangen. Ansätze zu ihrer Bestimmung sind z. B. variativ, indem eine Fläche so optimiert wird, dass sich die Anzahl an Durchstoßpunkten für ein Ensemble reaktiver Trajektorien verringert [30, 31]. Alternativ gibt es auch störungstheoretische Methoden mit Hilfe von Normalformentwicklungen [11, 32–40]. Durch die Weiterentwicklung und Anwendung solcher Näherungsmethoden konnten erste chemische Reaktionen mit wenigen Freiheitsgraden untersucht werden. Beispiele hierfür sind die $\text{H} + \text{H}_2$ [35, 41] Reaktion oder die Isomerisationsreaktionen von LiCN [42] und Keten [43]. Im Normalfall müssen solche Reaktionen jedoch weit höherdimensional beschrieben werden, was zu Problemen hinsichtlich der Konvergenz und des numerischen Aufwands solcher Methoden führt.

Aus diesem Grund ist ein erster Ansatzpunkt dieser Promotion die Entwicklung einer schnellen und numerisch exakten Methode zur Bestimmung der Trennflächen, welche von

reaktiven Trajektorien nur einmal durchstoßen werden. Weiterhin sollen diese Methoden nicht nur bei statischen, sondern auch bei getriebenen mehrdimensionalen Systemen funktionieren. Diese Erweiterung auf getriebene Systeme ist dabei alles andere als trivial. Während bei einem statischen System die Konstruktion einer solchen Trennfläche im Konfigurationsraum genügt, muss die Trennfläche bei einem getriebenen System zwingend zeitabhängig und im vollen Phasenraum konstruiert werden.

Die Verallgemeinerung auf zeitabhängige Systeme soll nicht nur zum besseren Verständnis von getriebenen chemischen Reaktionen beitragen, sondern auch einen wichtigen ersten Schritt zur Kontrolle von Reaktionsraten mit Hilfe äußerer Felder darstellen. Aus diesem Grund liegt der Schwerpunkt dieser Arbeit auf dem Verständnis des Einflusses äußerer Felder auf die Reaktionsdynamik und die zugehörigen Zerfallsraten der Reaktantenpopulation in der Nähe des Übergangszustandes. Hierzu werden verschiedene Methoden anhand eines zweidimensionalen Modellsystems eingeführt, entwickelt und später auf die getriebene Isomerisationsreaktion von LiCN angewendet.

Erste Schritte hin zu zeitabhängig getriebenen Systemen wurden in thermischen Systemen vollbracht [44–46]. Durch die Reibung lässt sich in einem solchen System die Vereinfachung einführen, dass zumindest für lange Zeiten die Dynamik auf der NHIM hin zu einer einzigen Trajektorie kollabiert. Diese sogenannte *TS-Trajektorie* kann dann als Aufhängepunkt einer planaren Trennfläche verwendet werden, welche sich entsprechend der Fluktuationen im System bewegt. Ohne diese Reduktion auf eine einzelne Trajektorie liegen jedoch im allgemeinen Fall unendlich viele Trajektorien in der NHIM eines zeitabhängig getriebenen und mehrdimensionalen Systems. Hier kommt es dann darauf an, nahe welcher dieser gebundenen Trajektorien eine reagierende Trajektorie auf ihrem Weg von der Reaktanten- zur Produktseite die Trennfläche durchstößt. Würde man einfach eine planare Trennfläche an eine einzelne Trajektorie in der NHIM anheften, würde man diesen Effekt komplett vernachlässigen.

Ein zentrales Resultat dieser Arbeit ist, dass die Position auf der NHIM, an welcher eine reagierende Trajektorie die Trennfläche durchstößt, einen starken Einfluss auf die Zerfallsrate der Reaktantenpopulation nahe des Übergangszustandes hat – zumindest in einer lokalen Umgebung der NHIM. Um diese Effekte isoliert untersuchen zu können, werden in dieser Arbeit nur getriebene Systeme ohne Fluktuationen und Reibung betrachtet.

Im Folgenden werden die Inhalte der einzelnen Kapitel dieser Arbeit kurz zusammengefasst. In Kapitel 1 beginnt die vorliegende Arbeit mit einer Einführung in das Thema und seiner Einordnung in einen größeren wissenschaftlichen Kontext.

In Kapitel 2 folgt dann die Einleitung in die theoretischen Hintergründe einer Reaktion über eine statische Energiebarriere im Rahmen der Theorie der Übergangszustände. Hierzu wird das Konzept einer Trennfläche im Phasenraum eingeführt, welche Reaktanten und Produkte als stabile Zustände eines reaktiven Systems voneinander trennt. Eine solche Trennfläche ist an der NHIM verankert. Wie in Kapitel 2 ausführlich diskutiert, entspricht die NHIM in einem eindimensionalen statischen System der ruhenden Trajektorie am Maximum der Barriere und ist deshalb lediglich ein Punkt im Phasenraum.

Bei mehrdimensionalen Systemen erweitert sie sich jedoch zur Hyperfläche welche eine unendliche Anzahl an Trajektorien enthält.

Konzeptionell auf wenige Grundannahmen an ein System zurückgreifend werden in Kapitel 2 verschiedene Konzepte und Beschreibungen des Phasenraumes in der Sattelregion entwickelt. Nach einer Diskussion eines eindimensionalen Systems folgt die Verallgemeinerung auf mehrdimensionale Systeme. Ein wichtiger Fokus liegt dabei auf der Unterscheidung zwischen offenen und geschlossenen Systemen. Bei letzteren liegt ein grundsätzliches Problem vor: Da im statischen Fall Energieerhaltung gilt, wird eine reaktive Trajektorie den Sattel zwischen Reaktant und Produkt unendlich oft überqueren. Eine global gültige Trennfläche mit der geforderten Eigenschaft von einer reaktiven Trajektorie nur einmal durchstoßen zu werden, kann in einem solchen System demnach prinzipiell nicht gefunden werden. Eine Lösung dieses Problems wird durch das Einführen einer geeigneten Sattelregion präsentiert, wodurch die zugehörige Trennfläche zumindest lokal nie mehr als einmal durchstoßen wird.

Der zweite Teil von Kapitel 2 befasst sich mit der Definition des Begriffs *Zerfallsrate der Reaktantenpopulation in der Nachbarschaft des Übergangszustandes* und wie sich eine solche Rate von einer Reaktionsrate über eine Energiebarriere nach Kramers unterscheidet. Eine Rate nach Kramers bezieht sich auf ein Ensemble thermischer Teilchen in einem Reaktantenbasin. Hier befindet sich eine Teilchenquelle, welche mit einem konstanten Teilchenstrom reaktive Teilchen einleitet. Aufgrund der thermischen Anregung im Rahmen einer Langevin-Dynamik können manche dieser Teilchen in seltenen Fällen die Barriere erklimmen und zur Produktseite entkommen. Hier werden sie dem System entnommen. Im thermischen Gleichgewicht stellt sich ein konstanter Teilchenstrom über die Barriere ein. Diesem Teilchenstrom ist eine Rate zugeordnet, die Reaktionsrate nach Kramers. Wichtig ist hier, dass sich die Populationen in Reaktantenbasin und in der Sattelregion stets im thermischen Gleichgewicht befinden.

Dies ist auch der grundlegende Unterschied zu den im Rahmen dieser Arbeit berechneten Zerfallsraten der Reaktantenpopulation in der Nachbarschaft des Übergangszustandes. Bei diesen Raten steht die Frage im Vordergrund, wie schnell eine Population von Reaktanten die Barriere überquert, nachdem sie die Barriere erklimmen und in die lokale Umgebung des Übergangszustandes eingetreten ist. Diese Zerfallsraten hängen allein von der spezifischen Form des Sattels und im Falle zeitabhängiger Systeme vom Einfluss des äußeren Feldes ab. Der Fokus der vorliegenden Arbeit liegt auf der Quantifizierung dieser Zerfallsraten und ihrer Beeinflussung durch Art und Bewegung des Sattels. Eine thermische Beschreibung wird hierbei bewusst ausgeklammert. Die Frage, ob und wie diese Zerfallsraten mit einer effektiven Beschreibung von Reaktionsraten nach Kramers für diese getriebenen Systeme zusammenhängen, ist Gegenstand künftiger Forschungen und das Fernziel auf diesem Forschungsgebiet. Zuvor müssten die in der vorliegenden Arbeit berechneten Zerfallsraten jedoch erst einmal um eine thermische Beschreibung ergänzt werden.

In Kapitel 3 dieser Arbeit werden die Einflüsse einer extern getriebenen Barriere auf die Dynamik in der Sattelregion diskutiert. Anhand eines zweidimensionalen Modell-

systems, d. h. eine Barriere mit einer instabilen reaktiven Koordinate und einer stabilen orthogonalen Mode, werden verschiedene Methoden zur Beschreibung dieser Dynamik und der zugehörigen Objekte im Phasenraum vorgestellt. Eines dieser Objekte ist die NHIM, welche für ein getriebenes System selbst zeitabhängig wird. Genau wie im statischen Fall enthält sie immer noch alle Trajektorien, welche für alle Zeiten in der Sattelregion gefangen sind und sich demnach im Übergangszustand zwischen Reaktanten und Produkten befinden.

An dieser NHIM lässt sich auch im getriebenen Fall weiterhin eine Trennfläche aufhängen, welche von reaktiven Trajektorien innerhalb einer gewissen Umgebung des Sattels nur einmal durchstoßen wird. Aus diesem Grund ist es für die spätere Berechnung von Zerfallsraten essentiell, die NHIM (und somit die Position dieser Trennfläche) an einer gegebenen Position im Phasenraum numerisch möglichst effektiv berechnen zu können. Hierzu werden zuerst verschiedene Methoden zur Charakterisierung der Dynamik reaktiver und nichtreaktiver Trajektorien in der lokalen Umgebung der NHIM vorgestellt. Mit Hilfe dieser Methoden lassen sich die stabile und die instabile Mannigfaltigkeit der NHIM auflösen, wobei sich die NHIM selbst stets an ihrem Schnittpunkt befindet. Eine Trajektorie direkt auf der stabilen Mannigfaltigkeit wird sich der NHIM asymptotisch nähern. Das bedeutet, sie erreicht die NHIM erst nach unendlich langer Zeit. Anders herum beschreibt die instabile Mannigfaltigkeit Trajektorien, welche sich von der NHIM wegbewegen.

Die beiden Mannigfaltigkeiten teilen den Phasenraum in der lokalen Umgebung der NHIM in vier Gebiete, zwei reaktive und zwei nichtreaktive. Die NHIM lässt sich im getriebenen System durch die Suche nach ihrem zeitabhängigen Schnittpunkt bestimmen, was jedoch mit einem relativ großen numerischen Aufwand verbunden ist. Aus diesem Grund wird in Kapitel 3.4.1 ein Algorithmus vorgestellt, mit welchem sich die NHIM an einzelnen Punkten numerisch deutlich effektiver finden lässt. Dieser Algorithmus basiert allein auf der Klassifizierung reaktiver und nichtreaktiver Trajektorien, d. h. auf der Frage, wo eine Trajektorie herkommt und wohin sie verläuft bezogen auf ihren Ein- und Austrittspunkt in der Sattelregion.

Falls die NHIM zur Bestimmung der Zerfallsraten für ein größeres Ensemble reaktiver Trajektorien individuell berechnet werden soll, erfordert auch diese schnelle Methode immer noch einen größeren numerischen Aufwand. Aus diesem Grund werden in Kapitel 3 auch ihre Interpolation mit Hilfe neuronaler Netze diskutiert und die Vor- und Nachteile einer solchen erläutert.

Im letzten Abschnitt von Kapitel 3 wird kurz auf die instabile Dynamik von Trajektorien in der NHIM eingegangen. Da diese Dynamik instabil ist, führt schon die kleinste numerische Abweichung dazu, dass Trajektorien aus der NHIM in Richtung Reaktant oder Produkt herausfallen. Mit Hilfe geeigneter Methoden lässt sich die Dynamik in der NHIM jedoch numerisch stabilisieren.

Kapitel 4 der vorliegenden Arbeit erläutert das Konzept der phasenraum aufgelösten Zerfallsraten der Reaktantenpopulation in der Nähe des Übergangszustandes für getriebene Systeme. Zu Beginn wird kurz auf die Unterschiede dieser getriebenen Zerfalls-

raten im Vergleich zu einem statischen System eingegangen. Anschließend werden drei Methoden vorgestellt, mit welchen sich diese Zerfallsraten numerisch berechnen lassen.

Die erste Methode, die *Ensemble-Methode*, ist sehr intuitiv: Zuerst wird ein lineares und homogenes Ensemble reaktiver Trajektorien in der lokalen Umgebung der NHIM auf der Reaktantenseite initialisiert. Anschließend wird dieses Ensemble entsprechend den Bewegungsgleichungen numerisch propagiert. Für jede Trajektorie und jeden Integrationszeitschritt wird dabei mit Hilfe des effizienten Algorithmus aus Kapitel 3 die zugehörige und individuelle Position der Trennfläche bestimmt. Sobald eine einzelne Trajektorie die Trennfläche durchstößt, wird die Anzahl der Reaktanten um eins verringert und die numerische Propagation dieser Trajektorie beendet. Aus der so erhaltenen Anzahl der Reaktanten über der Propagationszeit lässt sich dann die sogenannte *Ensemble-Rate* bestimmen. Diese zeitaufgelöste Rate gibt den instantanen Zerfall der Reaktantenpopulation in der Nähe eines Punktes auf der NHIM an. Für unterschiedliche zugehörige Positionen auf der NHIM wird dieser Zerfall im Allgemeinen unterschiedlich stark sein. Die jeweilige instantane Zerfallsrate hängt demnach von der spezifischen Position auf der NHIM im Phasenraum ab – eine phasenraumaufgelöste Zerfallsrate.

Konzeptionell ist die Ensemble-Methode relativ einfach, sofern die korrekte Initialisierung des reaktiven Ensembles beachtet wird. Aus numerischen Gesichtspunkten ist der Aufwand jedoch erheblich, da eine größere Anzahl an reaktiven Trajektorien propagiert werden muss und, was noch schlimmer ist, die Position der zugehörigen Trennfläche für jeden Zeitschritt individuell neu berechnet wird. Aus der Überlegung, diesen numerischen Aufwand zu reduzieren, ist eine zweite Methode entstanden, die *lokale Analyse der Mannigfaltigkeiten* (engl. local manifold analysis, LMA).

Die LMA basiert auf der Tatsache, dass die Dynamik in einer lokalen Umgebung der NHIM linearisiert werden kann. Das zeigt sich z. B. dadurch, dass sich die stabile und die instabile Mannigfaltigkeit in der Nähe ihres Schnittpunkts jeweils einer Geraden annähern. Durch geometrische Überlegungen und mit Hilfe dieser linearisierten Dynamik lässt sich so die instantane Zerfallsrate über eine geometrische Analyse des Phasenraums in der Nähe der NHIM berechnen – auf die zeitintensive Propagation von Trajektorien und das Errechnen der zugehörigen Trennfläche wird hierbei verzichtet. Dadurch ist die LMA im Vergleich zur Ensemble-Methode wesentlich schneller, liefert jedoch die gleichen Ergebnisse für die instantane Rate, zumindest in der lokalen Umgebung des Übergangszustandes.

Für periodische Trajektorien in der NHIM ist auch die zugehörige instantane Zerfallsrate eine periodische Funktion. Gemittelt über die volle Periode kann jeder dieser Trajektorien eine mittlere Zerfallsrate zugeordnet werden. Diese mittlere Zerfallsrate ergibt sich auch über eine dritte Methode, der *Floquet-Methode*, welche hierfür die Stabilitätseigenwerte der zugehörigen Monodromiematrix verwendet. Da zur Berechnung der Monodromiematrix über eine gesamte Periode einer solchen Bahn integriert werden muss, ist die Floquet-Rate immer als eine mittlere Rate anzusehen. Im Rahmen der vorliegenden Arbeit konnte die Floquet-Methode auch auf den viel häufigeren Fall einer quasi-periodischen Bahn in der getriebenen NHIM eines mehrdimensionalen Systems er-

weitert werden. Hierzu wird die Floquet-Rate für mehrere Umläufe einer Trajektorie auf dem zugehörigen stabilen Torus ermittelt.

Im letzten Abschnitt von Kapitel 4 folgt eine kurze Auflistung verschiedener Anwendungen der hier vorgestellten Methoden. Viele davon wurden im Rahmen einer Bachelor- oder Masterarbeit während meiner Forschungen am Institut durchgeführt und auch in Teilen von mir betreut [83, 85, 87, 91–93, 96–98].

In Kapitel 5 dieser Arbeit folgt die Anwendung dieser, üblicherweise an einem Modellsystem entwickelten, Methoden auf ein realistischeres physikalisches System, der $\text{LiCN} \rightleftharpoons \text{LiNC}$ Isomerisationsreaktion. Diese Reaktion wird hierzu erst einmal als mathematisches Modell eingeführt und sowohl die zugehörige Potentialfläche als auch die Dipolfläche zur Kopplung an ein externes Feld diskutiert. Für beide Flächen sind analytische Funktionen aus der Literatur bekannt [1, 2, 102]. Durch die Kopplung an ein äußeres Feld wird die LiCN Isomerisationsreaktion eigentlich zu einem dreidimensionalen Problem. Mit gewissen Vereinfachungen reduziert sich ihre Beschreibung im Rahmen dieser Arbeit jedoch auf zwei Dimensionen.

Im weiteren Fortgang von Kapitel 5 werden dann die Phasenraumstrukturen in der Sattelregion untersucht und die entsprechende Dynamik mit den bestehenden Methoden überprüft. Durch eine geeignete Wahl einer Reaktionskoordinate kann demnach auch für die LiCN Isomerisationsreaktion eine entsprechende Trennfläche an die NHIM angeheftet werden. Die zugehörigen Zerfallsraten werden sowohl im statischen als auch im getriebenen Fall berechnet. Hierbei zeigt sich, dass das externe Feld bei Wahl einer geeigneten Frequenz einen starken Einfluss auf die Dynamik in der NHIM hat. Dieser Einfluss ist auch direkt in den dazu berechneten Zerfallsraten zu sehen. Abschließend wird ein möglicher Interpretationsansatz dieser Änderungen im Sinne auftretender zusätzlicher Reaktionskanäle diskutiert, welche durch das externe Treiben hervorgerufen werden.

In der vorliegenden Arbeit werden wesentliche Fortschritte auf dem Gebiet der Theorie der Übergangszustände für zeitabhängige Systeme erzielt. Diese Fortschritte sind zweigeteilt: Einerseits werden numerisch effiziente Methoden zur Untersuchung und Charakterisierung solcher zeitabhängiger System vorgestellt, andererseits werden mit Hilfe dieser Methoden neue Erkenntnisse bezüglich der Struktur der Zerfallsraten der Reaktantenpopulation in der Nähe des Übergangszustandes gewonnen.

Diese Arbeit legt somit einen Grundstein für weitere Forschungen auf diesem Gebiet. So können nun z. B. die Dynamik auf der NHIM und die zugehörigen Zerfallsraten weiter untersucht werden. In der vorliegenden Arbeit wurde beispielsweise mehrfach die Annahme getroffen, dass Trajektorien auf der NHIM nicht chaotisch sein dürfen. Solche chaotischen Regimes der Dynamik auf der NHIM wurden zwar bisher noch nicht gefunden, sollten aber prinzipiell existieren. Hier wäre es interessant zu wissen, in wieweit die bisher entwickelten Methoden bei Annäherung an ein solches chaotisches Gebiet auf der NHIM noch gültig sind oder ob sie ggf. verändert werden müssen. Eine wichtige Fragestellung in Richtung Dynamik auf der NHIM könnte auch der Einfluss des äußeren Treibens auf die Reaktionskanäle der NHIM sein und ob sich damit Reaktionsraten beeinflussen oder sogar gezielt steuern lassen.

Die im Rahmen dieser Arbeit errechneten Zerfallsraten gelten nur in einer lokalen Umgebung des Übergangszustandes. Eine wichtige Aufgabe für zukünftige Forschungen wird deshalb die Suche nach einer möglichen Verbindung zwischen diesen Zerfallsraten und den Reaktionsraten nach Kramers über eine Barriere, ausgehend von einem thermischen Zustand im Reaktantenbasin, sein. Noch ergeben sich hier allerdings Probleme. So muss z. B. für diese globalen Reaktionspfade trotzdem erst überprüft werden, ob die gefundenen Trennflächen auch wirklich nur einmal durchstoßen werden. Falls nein, muss eventuell eine kompliziertere Definition des Sattelgebiets oder eine kompliziertere Form der Trennfläche entwickelt werden. Auch muss dann natürlich erst einmal die bestehende Theorie, welche für Hamiltonsche Systeme ohne Fluktuation und Dissipation entwickelt wurde, um eine Beschreibung für thermische Systeme erweitert werden. Die Entwicklung einer temperaturabhängigen Beschreibung von Zerfallsraten nahe des Übergangszustandes stellt somit einen nächsten logischen Schritt hin zu realistischeren Systemen dar.

Unter Annahme des Kollaps der NHIM auf eine einzelne Trajektorie aufgrund der Reibung in einem thermischen System wurden solche Rechnungen im Langzeitlimit bereits durchgeführt [44–46]. Die Verallgemeinerung unter Berücksichtigung der vollen Dynamik auf der NHIM ist jedoch anspruchsvoll. Während sich die Interpolation der NHIM durch neuronale Netze für die bisher untersuchten Systeme als nicht vorteilhaft erwiesen hat, könnte sich diese Tatsache für die Untersuchung thermischer Systeme ändern. Hier müssen typischerweise Mittelwerte für eine große Zahl reaktiver Trajektorien ermittelt werden, was mit den bestehenden, numerisch exakten, Methoden einen relativ großen numerischen Aufwand erfordert.

Auch ohne methodische Fortschritte können die im Rahmen dieser Arbeit entwickelten Techniken und Verfahren auch schon jetzt auf eine Vielzahl von Problemen und Fragestellungen angewendet werden. Z. B. wurde in Kapitel 5 die LiCN Isomerisationsreaktion durch eine Vereinfachung auf ein zweidimensionales Problem reduziert. Unter Beachtung der vollen Dynamik des Systems handelt es sich bei der Kopplung dieser Reaktion an ein äußeres Feld jedoch eigentlich um ein dreidimensionales Problem. Eine Anwendung der bestehenden Methoden auf dieses Problem sollte direkt möglich sein. Aber auch Anwendungen auf andere Reaktionen sind denkbar, z. B. auf Keten [43], KCN [115] oder, wie schon in den Referenzen [97, 98] begonnen, auf die Spintronik.

Matthias Feldmaier

Persönliche Daten

Geburtsdatum 06.01.1990
Geburtsort Nürtingen

Schulbildung

1996 – 2000 **Friedrich-Glück-Schule**, Nürtingen-Oberensingen.
2000 – 2009 **Max-Planck-Gymnasium**, Nürtingen.
Allgemeinbildendes Abitur am 23.06.09

Studium und Promotion

2010-10 – 2013-10 **Bachelorstudiengang Physik**, Universität Stuttgart.
Abschluss Bachelor of Science am 19.09.13

2013-05 – 2013-08 **Bachelorarbeit**, *Stabilisierung eines schmalbandigen Lasersystems zur Spektroskopie an Dysprosium*, Betreuung: Prof. Dr. Tilman Pfau.
5. Physikalisches Institut, Universität Stuttgart

2013-10 – 2015-10 **Masterstudiengang Physik**, Universität Stuttgart.
Abschluss Master of Science am 09.10.15

2014-10 – 2015-10 **Masterarbeit**, *Untersuchung exzeptioneller Punkte bei Exzitonen in parallelen elektrischen und magnetischen Feldern*, Betreuung: Apl. Prof. Dr. Jörg Main.
1. Institut für Theoretische Physik, Universität Stuttgart

2015-10 – 2020-09 **Promotion**, *Phase-space resolved decay rates of driven systems near the transition state*, Betreuung: Apl. Prof. Dr. Jörg Main.
1. Institut für Theoretische Physik, Universität Stuttgart

Berufliche und wissenschaftliche Tätigkeiten

Seit Okt. 2015 **Wissenschaftlicher Mitarbeiter**, ITP1, Universität Stuttgart.
Forschung, Betreuung von Bachelor- & Masterarbeiten, Übungsgruppenleitung

Seit 01.10.2017 **Stipendiat nach dem Landesgraduiertenförderungsgesetz (LGFG)**, Land Baden-Württemberg.
Förderung des hochqualifizierten wissenschaftlichen Nachwuchses

Seit 2017 **Mitarbeit im Horizon 2020 Research and Innovation Program der Europäischen Union**, Marie Skłodowska-Curie Grant Agreement No. 734557.
Internationales Mobilitätsprogramm zur Förderung von Nachwuchskräften

Auslandsaufenthalte

- 23.07.17 – 07.08.17 **Georgia Tech, Atlanta und Johns Hopkins University, Baltimore**, bei Prof. Dr. Rafael de la Llave und Prof. Dr. Hernandez.
Wissenschaftlicher Austausch und Projektplanung zur internationalen Zusammenarbeit
- 09.03.18 – 31.03.18 **Johns Hopkins University, Baltimore**, bei Prof. Dr. Hernandez.
Wissenschaftlicher Austausch und Projektplanung zur internationalen Zusammenarbeit
- 04.04.19 – 30.04.19 **Johns Hopkins University, Baltimore**, bei Prof. Dr. Hernandez.
TraX Meeting 2019 und wissenschaftlicher Austausch

Wissenschaftliche Fachvorträge

29. Feb. 2016 **An improved method for finding exceptional points and application to Rydberg systems in external fields**, Frühjahrstagung der Deutschen Physikalischen Gesellschaft, Leibniz Universität Hannover.
12. März 2018 **Transition State Theory for Driven Chemical Reactions: Current State of Research**, Kolloquium Arbeitsgruppe Prof. Dr. Rigoberto Hernandez, Johns Hopkins University, Baltimore.
26. April 2019 **Transition State Theory for Driven Chemical Reactions: Current State of Research**, TraX Meeting 2019, Johns Hopkins University, Baltimore.

Wissenschaftliche Veröffentlichungen

- 2016 **Rydberg systems in parallel electric and magnetic fields: an improved method for finding exceptional points**, *M. Feldmaier, J. Main, F. Schweiner, H. Cartarius, G. Wunner*, *J. Phys. B: At. Mol. Opt. Phys.* **49**, 144002.
- 2016 **Impact of the valence band structure of Cu₂O on excitonic spectra**, *F. Schweiner, J. Main, M. Feldmaier, G. Wunner, C. Uihlein*, *Phys. Rev. B* **93**, 195203.
- 2017 **Chemical dynamics between wells across a time-dependent barrier: Self-similarity in the Lagrangian descriptor and reactive basins**, *A. Junginger, L. Duvenbeck, M. Feldmaier, J. Main, G. Wunner, R. Hernandez*, *J. Chem. Phys.* **147**, 064101.
- 2017 **Obtaining time-dependent multi-dimensional dividing surfaces using Lagrangian descriptors**, *M. Feldmaier, A. Junginger, J. Main, G. Wunner, R. Hernandez*, *Chem. Phys. Lett.* **687**, 194-199.
- 2018 **Binary contraction method for the construction of time-dependent dividing surfaces in driven chemical reactions**, *R. Bardakcioglu, A. Junginger, M. Feldmaier, J. Main, R. Hernandez*, *Phys. Rev. E* **98**, 032204.

- 2018 **Neural network approach to time-dependent dividing surfaces in classical reaction dynamics**, *P. Schraft, A. Junginger, M. Feldmaier, R. Bardakcioglu, J. Main, G. Wunner, R. Hernandez*, Phys. Rev. E **97**, 042309.
- 2019 **Invariant Manifolds and Rate Constants in Driven Chemical Reactions**, *M. Feldmaier, P. Schraft, R. Bardakcioglu, J. Reiff, M. Lober, M. Tschöpe, A. Junginger, J. Main, T. Bartsch, R. Hernandez*, J. Phys. Chem. B **123**, 2070–2086.
- 2019 **Phase-space resolved rates in driven multidimensional chemical reactions**, *M. Feldmaier, R. Bardakcioglu, J. Reiff, J. Main, R. Hernandez*, J. Chem. Phys. **151**, 244108.
- 2020 **Neural network approach for the dynamics on the normally hyperbolic invariant manifold of periodically driven systems**, *M. Tschöpe, M. Feldmaier, J. Main, R. Hernandez*, Phys. Rev. E **101**, 022219.
- 2020 **Influence of external driving on decays in the geometry of the LiCN isomerization**, *M. Feldmaier, J. Reiff, R. M. Benito, F. Borondo, J. Main, R. Hernandez*, J. Chem. Phys. **153**, 084115.
- 2020 **Dynamics and decay rates of a time-dependent two-saddle system**, *J. Reiff, M. Feldmaier, J. Main, R. Hernandez*, Submitted to Phys. Rev. E.
- 2020 **Controlling decay rates in model chemical reactions through external driving**, *J. Reiff, R. Bardakcioglu, M. Feldmaier, J. Main, R. Hernandez*, Submitted to Phys. Rev. E.
- 2020 **Thermal decay rates of an activated complex in a driven model chemical reaction**, *R. Bardakcioglu, J. Reiff, M. Feldmaier, J. Main, R. Hernandez*, In preparation.



Danksagung

An dieser Stelle möchte ich mich bei allen bedanken, die zum Gelingen der vorliegenden Dissertation beigetragen haben. Mein besonderer Dank gilt:

- Meinem Betreuer Prof. Dr. Jörg Main. Lieber Jörg, vielen Dank für die Zusammenarbeit in den letzten Jahren. Wenn ich irgendwo mal nicht weiter kam, konnte ich immer zu dir kommen und du hast dir jedes Mal so lange Zeit für mich genommen, bis wir eine Lösung gefunden haben. Nicht nur als Betreuer und Promotionsstudent, sondern als Kollegen haben wir oft gemeinsam an einer Lösung getüftelt. Meine Meinung war dir immer wichtig und du hast mir Freiraum für eigene Ideen gelassen. Nicht nur bei den Auslandsreisen, auch am Institut haben wir immer wieder schöne Ausflüge zusammen unternommen. Gerade zum Ende meiner Promotion hast du auch sehr viel Verständnis für meine neue familiäre Situation aufgebracht und mich auch darin sehr unterstützt. Ich weiß, dass das alles nicht selbstverständlich ist und bin dir deshalb sehr dankbar dafür!
- Prof. Dr. Udo Seifert für die Übernahme des Mitberichts.
- Prof. Dr. Günter Wunner. Lieber Herr Wunner, danke dass Sie sich so für mich eingesetzt haben. Ohne Ihre Hilfe wäre diese Promotion so sicher nicht zustande gekommen.
- Prof. Dr. Rigoberto Hernandez from the Johns Hopkins University in Baltimore. Dear Rigoberto, I had the pleasure to visit you several times. And each time I was amazed once more: hospitality is really your thing. Although you are always so busy, you took us out on a trip, invited us to dinner, served us delicious drinks, made me have the weirdest visit to the movies I ever had, gave us advice for some sightseeing or just somehow smuggled us into your schedule in between all the other important meetings. I learned so much during these trips, not just science, but also for life!

- Amy and Goby Hernandez. Dear Amy, thanks for all the invitations to dinner, the food you prepared was always so delicious. You always tried your best making us feel at home in Baltimore by sharing your limited family time with us – I really appreciate that. Especially the trips out of town to the lake and horseland were wonderful! Dear Goby, you always had to hang out with us “old guys” and when you called me “weird” and “somehow cool” I was really happy to hear that I might have stayed young somehow ;-). If you ever come back to Germany, feel free to let me know, we still need to do some caving!
- Dr. Thomas Bartsch von der Loughborough University. Lieber Thomas, mir haben die Ausflüge mit dir sehr Spaß gemacht und auch die (nicht immer nur) fachlichen Diskussionen mit dir habe ich immer sehr geschätzt. Von dir habe ich wirklich viel gelernt und oft habe ich mir nach dem Schreiben eines Kapitels gedacht: Was würde Thomas jetzt dazu sagen?
- Dr. Yutaka Nagahata who was a postdoc in Rigoberto’s group when I visited Baltimore and has now returned to Hokkaido University to join the group of Prof. Dr. Komatsuzaki. Dear Yutaka, it was so much fun talking to you. You showed me some nice aspects of Japanese food either by cooking yourself or by taking us to the Ramen place in Baltimore. Oh, and the trip you organized to Washington DC for Sakura was awesome!
- Prof. Dr. Florentino Borondo from the Universidad Autónoma de Madrid. Dear Tino, having you join us during our stays in Atlanta and Baltimore made our trips far more relaxing. And you told me so many interesting things, not only about science and LiCN, but also about boats and sailing. Thanks also to Tino’s wife, Prof. Dr. Rosa M. Benito, whom I met during the last days of my recent trip to Baltimore. Having a conversation with you was so much fun!
- Meinen Kollegen, die mit mir in der TST Gruppe am ITP1 gearbeitet haben oder noch arbeiten: Andrej Junginger, Lennard Duvenbeck, Philippe Schraft, Robin Schuldt, Robin Bardakcioglu, Johannes Reiff, Martin Tschöpe, Melissa Lober, Tobias Mielich, Jonas Zatsch, Johannes Mögerle, Manuel Kuchelmeister, Pooja Mishra und Michael Maihöfer. Ich habe gerne mit euch und im Team gearbeitet.
- Allen weiteren Kollegen am ITP1, besonders jedoch allen ehemaligen und aktuellen Mitgliedern der Kaffeerrunde. Ein tägliches Highlight zur Mittagszeit, auch wenn ich nie Kaffee getrunken habe.
- Frau Bund, der Sekretärin des ITP1. Vielen Dank, dass Sie mit langem Atem all die sinnlosen und oft logikbefreiten Diskussionen mit unserer „Verwaltung“ über alle möglichen Arten und Unarten meiner Anstellung durchgestanden haben!
- Dem Land Baden-Württemberg und der Universität Stuttgart für die Gewährung des Promotionsstipendiums nach dem Landesgraduiertenförderungsgesetz.

-
- Meinen Eltern und meiner Familie, die mich bei dieser langen Ausbildung stets unterstützt und an mich geglaubt haben.
 - Meiner Frau Teresa, die einfach wundervoll ist. Danke, für alles!
 - Meinem Sohn Theo. Danke, dass du immer so brav geschlafen hast, während Papa sich die Nächte mit der Fertigstellung dieser Dissertation um die Ohren gehauen hat.

Ehrenwörtliche Erklärung

Ich erkläre, dass ich diese Dissertation, abgesehen von den ausdrücklich bezeichneten Hilfsmitteln, selbständig verfasst habe.

Stuttgart, den 30. April 2020

Matthias Feldmaier